A Study of the decay $\tau \longrightarrow \mu\nu\bar{\nu}$ using the DELPHI Detector at LEP

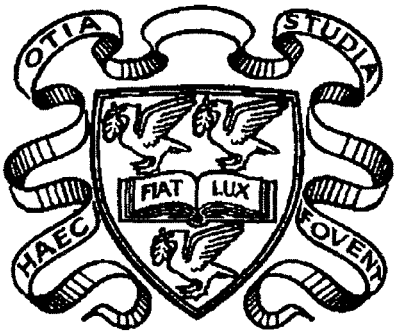

Thesis submitted in accordance with the requirements
of the University of Liverpool
for the degree of Doctor in Philosophy
by

Baljeet Nijjhar

Oliver Lodge Laboratory
University of Liverpool

August 1993

A Study of the decay $\tau \rightarrow \mu\nu\bar{\nu}$ using the DELPHI Detector at LEP

Baljeet Nijjhar

Abstract

An initial sample of 6129 $e^+e^- \rightarrow \tau^+\tau^-$ events, corresponding to an integrated luminosity of 9.9 pb^{-1}, has been collected during the 1991 year of data-taking at energies around the Z^o peak of 91 GeV using the DELPHI detector at LEP.

From this sample, 1613 $\tau \rightarrow \mu\nu\bar{\nu}$ decays have been isolated and a measurement of the branching ratio $Br(\tau \rightarrow \mu\nu\bar{\nu})$ performed. The value obtained is $Br(\tau \rightarrow \mu\nu\bar{\nu}) = 17.58 \pm 0.41$ (stat) $\pm$ 0.27 (syst). This measurement implies $(g_\mu/g_e)^2 = 1.018 \pm 0.028$ and $(g_\tau/g_e)^2 = 0.998 \pm 0.030$, where g_l is the effective weak coupling constant at the l–W–$\bar{\nu}_l$ vertex. Thus, these ratios are consistent with the Standard Model assumption of equal couplings for the three lepton generations.

With a slightly looser selection giving 1644 $\tau \rightarrow \mu\nu\bar{\nu}$ decays, their momentum spectrum has been used to measure the average tau polarisation around the Z^o peak. The value obtained is $A_{pol}(\tau) = -0.114 \pm 0.129$ (stat) $\pm$ 0.091 (syst), which gives the ratio of the vector (c_V^τ) and axial-vector (c_A^τ) coupling constants of the tau to the Z^o as $(c_V^\tau)/(c_A^\tau) = 0.058 \pm 0.079$. This results in a value for the effective electroweak mixing angle at the Z^o mass scale of $\sin^2\theta^l_{W_{eff}}(M_Z^2) = 0.2354 \pm 0.0198$.

Acknowledgements

First and foremost, my biggest thanks go to Dr. Duncan Reid who has been a completely fabulous guide to me during my PhD. I am lucky and glad he was there on the countless occasions when I needed sound judgment, infallible advice, a healthy attitude injection, or just fine brains to pick. He has been invaluable in helping me get this together, and I appreciate it very deeply.

I feel privileged to have worked with an excellent group of people in the DELPHI tau analysis team, who made work and meetings fun. Several of them have helped me in many ways, and encouraged me in my work. In particular, I would like to thank Mogens Dam very much for being the other half of a great office, for giving me the benefit of his advice and wisdom concerning my own and mutual problems, and for sharing with me some very useful software. Thanks also to Walter Bonivento for discussions on the niceties of polarisation measurements.

Thank you to Professors Paul Booth and Erwin Gabathuler for accepting me to do this PhD, and the staff of Liverpool University for their help. I am also grateful to my patient and efficient proofreaders for their comments: Dr. Duncan Reid, Dr. Barry King, my supervisor Dr. Mike Houlden and Dr. Neil Jackson.

The first three years of this PhD were funded by the Science and Engineering Research Council. I am very much indebted to Gonz, Helenka (especially...) and Paul Booth for their kind practical help during the tricky non-funded fourth year.

Thanks to Julia for sending me vital papers and keeping me up-to-date (not just on muons) and generally being a blessing. Thanks to my Liverpool friends for such ace times that I always hated having to pack to go back out to Geneva. And thanks to my Geneva friends for the motorcycle rides, helping to try and save the New Morning from bankruptcy and for convincing a non-swimmer she had any business at Meyrin Pool.

Finally, thanks to Mum, Dad and Raj for their ♡ and support.

Contents

List of Figures

List of Tables

Introduction

The science of particle physics has been evolving rapidly over the past few decades. The proliferation of hadron states that had been observed experimentally can now be explained in terms of their composition of the more fundamental *quarks* – the up, down, charm, strange and bottom. On the other hand, the electron and electron neutrino, fundamental *leptons* as far as we can observe with the accelerators of today, have acquired seeming 'clones' in the muon and muon neutrino, and the tau and tau neutrino. The interactions between the particles are postulated to be mediated by bosons, differing in mass and coupling strength such that the interactions appear to be distinct.

At present, our best understanding concerning the electromagnetic and weak interactions is the Standard Electroweak Model [1]. One of the predictions of the Standard Model was the existence of weak interactions mediated by a neutral particle (the Z^o) which were duly observed in 1973 [2]. This provided the motivation behind the construction of the LEP collider [3] as a testing ground for the Standard Model. The collider will also allow the study of quantum chromodynamics, the theory of strong interactions, and the opportunity for new discoveries in its energy range. Currently, it is in its first phase of operation, LEP100, running at centre-of-mass energies around the Z^o resonance of 91 GeV. In the second phase, LEP200, W^+W^- pairs will be produced at centre-of-mass energies of up to 200 GeV.

In this thesis, the production of $\tau^+\tau^-$ pairs at the Z^o resonance during the 1991 year of data collection is studied using the DELPHI detector [4]. The tau is a massive particle decaying weakly via a variety of modes. In particular, the decay mode $\tau^- \rightarrow \mu^-\bar{\nu}_\mu\nu_\tau$[1] is isolated and a measurement of the branching ratio is performed. This measurement

[1]The analysis includes $\tau^+ \rightarrow \mu^+\nu_\mu\bar{\nu}_\tau$, and both will be understood to be referred to by the usage of $\tau^- \rightarrow \mu^-\bar{\nu}_\mu\nu_\tau$, unless otherwise specified.

is used to test the Standard Model assumption of equal couplings of the $W^{\pm}$ to leptons irrespective of flavour. The average tau polarisation is also measured with the muon decay mode. From this measurement, the ratio of the vector and axial-vector couplings of the tau to the Z^o is estimated, and the value of the parameter θ_W which governs the mixing of photon and Z^o fields in the Standard Model is obtained.

A brief outline of the Standard Model is presented in Chapter 1, with a derivation of some observables sensitive to θ_W. Within this context, the tau particle is discussed in Chapter 2, with emphasis on the physics contained in the muon decay mode. Chapter 3 describes the LEP collider and the DELPHI detector, the experimental apparatus of the analysis. The selection procedure for $e^+e^- \rightarrow \tau^+\tau^-$ events is described in detail in Chapter 4, and is primarily the analysis of [5]. The selection of the $\tau^- \rightarrow \mu^- \bar{\nu}_\mu \nu_\tau$ decays from this sample is given in Chapter 5. The determination of efficiencies and backgrounds from data is stressed for both selections. The branching ratio measurement is performed in Chapter 6, while Chapter 7 is devoted to the polarisation measurement. Finally, there is a short conclusion giving the main results of this analysis.

Chapter 1

The Standard Electroweak Model

The Standard Electroweak Model [1] is an attempt to describe the electromagnetic and weak interactions of particles on the same level. To date, excellent agreement between the predictions of the model and experiment has been observed. A brief description of some of the main ingredients is given below, and observables which can give information on some of the parameters of the model are derived.

1.1 Construction of a symmetric Lagrangian

As far as has been observed, only left-handed neutrinos (and right-handed antineutrinos) exist in nature. Furthermore, the limits on neutrino masses indicate that they could be massless. Based on these facts, the electron e^- and its neutrino ν_e can be put into a left-handed *weak isospin* doublet

$$\psi_L = \begin{pmatrix} \nu_e \\ e^- \end{pmatrix}_L, \quad t_L^3 = \pm\frac{1}{2} \tag{1.1}$$

where t^3 is the third component of weak isospin, and the electron is additionally allowed a right-handed weak isospin singlet state

$$\psi_R = e_R^-, \quad t_R^3 = 0 \tag{1.2}$$

with similar doublets and singlets for (ν_μ, μ^-) and (ν_τ, τ^-), the other two lepton generations. In this notation, ψ_L and ψ_R are the left-handed and right-handed components of the particle spinor ψ and can be expressed as

$$\psi_L = \frac{1}{2}(1-\gamma_5)\psi, \quad \psi_R = \frac{1}{2}(1+\gamma_5)\psi \tag{1.3}$$

For quarks we have the doublet

$$\psi_L = \begin{pmatrix} u \\ d' \end{pmatrix}_L \tag{1.4}$$

with similar doublets for (c, s') and (t, b') (in anticipation that the top quark will be discovered). For the lower members of the doublets, the left-handed states are orthogonal combinations of the flavour states i.e.

$$\begin{pmatrix} d' \\ s' \\ b' \end{pmatrix} = U \begin{pmatrix} d \\ s \\ b \end{pmatrix} \tag{1.5}$$

where U is the Cabbibo–Kobayashi–Maskawa matrix [6]. There are also two singlet states per generation since in the case of quarks, both members of the generation are massive:

$$\psi_R = u_R,\ d'_R \tag{1.6}$$

and similarly for (c, s') and (t, b'). This structure for the quarks is to ensure agreement with experimental observation that although charged weak currents can mix flavours and generations, there are no flavour-changing weak neutral currents. The classification of the quarks and leptons into these generations accounts for all the (so far) fundamental fermions.

To include electromagnetism in the description of weak interactions, the *weak hypercharge* Y is defined through the Gell-Mann–Nishijima formula [7]

$$Q = t^3 + \frac{Y}{2} \tag{1.7}$$

where Q is the electric charge in units of e. Thus, $Y_L = -1$ and $Y_R = -2$ for the lepton generations.

Requiring that the electroweak Lagrangian be invariant under local phase transformations generated by t and $\frac{Y}{2}$ leads to its form as

$$\begin{aligned} \mathcal{L}_{symm} &= \overline{\psi}_R i\gamma^\mu(\partial_\mu + ig'\frac{Y_R}{2}B_\mu)\psi_R + \overline{\psi}_L i\gamma^\mu \mathcal{D}_\mu \psi_L \\ &\quad (\ + \text{gauge boson kinetic energy terms}) \end{aligned} \tag{1.8}$$

with the gauge-covariant derivative $\mathcal{D}_\mu$ given by

$$\mathcal{D}_\mu = \partial_\mu + ig'\frac{Y_L}{2}B_\mu + ig\boldsymbol{t}.\boldsymbol{W}_\mu \tag{1.9}$$

where $[t_i, t_j] = i\varepsilon_{ijk}t_k$ and are usually represented in terms of the Pauli spin matrices

$$t_1 = \frac{1}{2}\begin{pmatrix} 0 & 1 \\ 1 & 0 \end{pmatrix}, \quad t_2 = \frac{1}{2}\begin{pmatrix} 0 & -i \\ i & 0 \end{pmatrix}, \quad t_3 = \frac{1}{2}\begin{pmatrix} 1 & 0 \\ 0 & -1 \end{pmatrix} \tag{1.10}$$

Thus the interaction terms of the Lagrangian are due to the $SU(2)_L$ weak isospin currents $\boldsymbol{J^\mu}$ mediated by three gauge bosons $\boldsymbol{W_\mu}$ with coupling constant g:

$$-ig\boldsymbol{J^\mu}.\boldsymbol{W_\mu} = -ig\overline{\psi}_L\gamma^\mu \boldsymbol{t}.\boldsymbol{W_\mu}\psi_L \tag{1.11}$$

and the $U(1)_Y$ weak hypercharge current j^μ mediated by the gauge boson B_μ with coupling constant g':

$$-ig'j^\mu B_\mu = -ig'\overline{\psi}\gamma^\mu\frac{Y}{2}B_\mu\psi \tag{1.12}$$

1.2 Generation of mass terms

The physical interactions observed involve massive fermions as well as three massive gauge bosons, of which two are charged ($\pm$ 1) and one is neutral. The only massless gauge boson observed is the photon. Adding terms of the form $-m\overline{\psi}\psi$ for the fermion mass for instance does not preserve the invariance of the Lagrangian under $SU(2)_L \otimes$ $U(1)_Y$ transformations since $-m\overline{\psi}\psi$ can be written as

$$-m\overline{\psi}[\frac{1}{2}(1-\gamma_5)+\frac{1}{2}(1+\gamma_5)]\psi \;\; = \;\; -m(\overline{\psi}_R\psi_L + \overline{\psi}_L\psi_R) \tag{1.13}$$

where the right-hand side is obtained using Equation 1.3 and the properties of the Dirac matrices. Therefore, left- and right-handed components which transform differently are mixed. To ensure a renormalisable[1] theory, the symmetry of the Lagrangian must be broken in a gauge invariant way. This is achieved via the Higgs mechanism [8]. In the Minimal Standard Model, the Higgs complex scalar fields are introduced in the form of a single $SU(2)_L$ doublet

$$\phi = \begin{pmatrix} \phi^+ \\ \phi^0 \end{pmatrix} = \frac{1}{\sqrt{2}}\begin{pmatrix} \phi_1 + i\phi_2 \\ \phi_3 + i\phi_4 \end{pmatrix}, \quad Y_L = 1 \tag{1.14}$$

The Lagrangian term for this doublet is

$$\mathcal{L}_{Higgs} = (\mathcal{D}_\mu\phi)^\dagger(\mathcal{D}_\mu\phi) - \mu^2(\phi^\dagger\phi) + |\lambda|\,(\phi^\dagger\phi)^2 \tag{1.15}$$

where the last two terms describe the Higgs potential. The symmetry is broken for

[1] In which divergent terms can be systematically cancelled order by order.

$\mu^2 < 0$ by choosing a non-zero vacuum expectation value (VEV) for ϕ such that

$$\langle\phi\rangle_0 = \begin{pmatrix} 0 \\ v/\sqrt{2} \end{pmatrix} \tag{1.16}$$

where $v = \sqrt{-\mu^2/|\lambda|}$. (This choice ensures that the vacuum state is electrically neutral as required by charge conservation, and thus the boson corresponding to the charge operator Q, the photon, will remain massless.) The masses of the gauge bosons can be identified by substitution of the VEV $\langle\phi\rangle_0$ into the Lagrangian (1.15). The relevant term is given by

$$\begin{aligned}\left[\left(ig\boldsymbol{t}.\boldsymbol{W}_\mu + i\frac{g'}{2}B_\mu\right)\langle\phi\rangle_0\right]^\dagger &\left[\left(ig\boldsymbol{t}.\boldsymbol{W}_\mu + i\frac{g'}{2}B_\mu\right)\langle\phi\rangle_0\right] \\ &= \frac{1}{8}v^2g^2(W^{1\mu} - iW^{2\mu})(W^1_\mu + iW^2_\mu) \\ &+ \frac{1}{8}v^2(gW^{3\mu} - g'B^\mu)(gW^3_\mu - g'B_\mu) \\ &+ 0(g'W^{3\mu} + gB^\mu)(g'W^3_\mu + gB_\mu)\end{aligned} \tag{1.17}$$

where the right-hand side is the explicit expression of the left-hand side. These terms can be identified with the mass terms of the physical boson fields. For the charged fields, we observe that the interaction term $-ig\overline{\psi}_L\gamma^\mu(t^1W^1_\mu + t^2W^2_\mu)\psi_L$ can be written in the form

$$-ig\overline{\psi}_L\gamma^\mu(t^1W^1_\mu + t^2W^2_\mu)\psi_L = \frac{-ig}{\sqrt{2}}\overline{\psi}_L\gamma^\mu(t^+W^+_\mu + t^-W^2_\mu)\psi_L \tag{1.18}$$

where $t^\pm = t^1 \pm it^2$ are charge changing operators, and $W^\pm_\mu = \frac{1}{\sqrt{2}}(W^1_\mu \mp iW^2_\mu)$ are normalised orthogonal combinations of W^1_μ and W^2_μ. Thus, $W^\pm_\mu$ must represent the physical charged bosons, and the first term on the right-hand side of Equation 1.17 can be identified as the appropriate mass term $\frac{1}{2}M^2_W W^{+\mu}W^-_\mu$ giving

$$M_W = \frac{1}{2}gv \tag{1.19}$$

Similarly, if we define two normalised and orthogonal neutral fields by the combinations

$$A_\mu = \frac{g'W^3_\mu + gB_\mu}{\sqrt{g^2 + g'^2}}, \qquad Z_\mu = \frac{gW^3_\mu - g'B_\mu}{\sqrt{g^2 + g'^2}} \tag{1.20}$$

it is seen that $M_A = 0$ and thus represents the photon, and

$$M_Z = \frac{v\sqrt{g^2 + g'^2}}{2} \tag{1.21}$$

representing a massive neutral boson, the Z^o. With the mixing angle between the W^3_μ

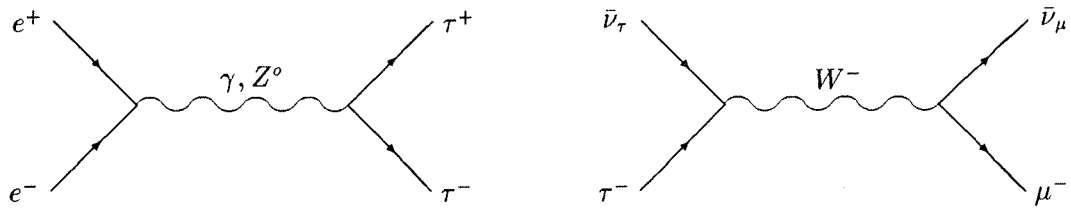

Figure 1.1: *Feynman diagrams for neutral and charged current interactions describing $\tau^+\tau^-$ production and decay (the muonic decay mode is shown as an example) at LEP.*

and B_μ fields given by

$$\tan\theta_W = \frac{g'}{g} \tag{1.22}$$

then (for the Standard Model with one Higgs doublet) we have the relation

$$\frac{M_W}{M_Z} = \cos\theta_W \tag{1.23}$$

The masses of the leptons m_l can be introduced with the same Higgs doublet by adding invariant terms of the form

$$-G_l(\overline{\psi}_R\phi^\dagger\psi_L + \overline{\psi}_L\phi\psi_R) \tag{1.24}$$

Substitution of the VEV $\langle\phi\rangle_0$ leads to expressions of the form

$$m_l = \frac{G_l v}{\sqrt{2}} \tag{1.25}$$

with G_l to be determined experimentally. The masses of the quarks are introduced in a similar way. One neutral Higgs particle is anticipated in the Standard Model, but has not yet been found.

1.3 Charged current interaction

At LEP, in the decay chain (see Figure 1.1)

$$e^+e^- \to Z^o, \gamma \to \tau^+\tau^-, \quad \tau^\pm \to W^\pm \to \bar{\nu}_\tau, \nu_\tau + \ldots$$

both charge-changing and neutral currents are studied. The charged current interaction term of Equation 1.18 is given in terms of the left-handed component of the spinor ψ. In terms of ψ itself, we can use Equation 1.3 to express the interaction as

$$\frac{-ig}{\sqrt{2}}\overline{\psi}\frac{1}{2}\gamma^\mu(1-\gamma^5)(t^+W_\mu^+ + t^-W_\mu^-)\psi$$

Thus for the charged curent interactions, the vector component (proportional to γ^μ) and the (minus) axial-vector component (proportional to $\gamma^\mu\gamma^5$) are equal. This pure $V-A$ structure is consistent with experiment [9] and will be assumed in the subsequent weak decays of the tau. The components for the weak neutral current are not equal, as discussed below.

1.4 Neutral currrent interaction

This refers to both the weak neutral current mediated by the Z^o and the electromagnetic current mediated by the photon. The neutral components of the $\mathrm{SU}(2)_L$ and $\mathrm{U}(1)_Y$ interactions are given by

$$-i\overline{\psi}_L\gamma^\mu(gt_L^3W_\mu^3 + g'\frac{Y_L}{2}B_\mu)\psi_L - ig'\overline{\psi}_R\gamma^\mu\frac{Y_R}{2}B_\mu\psi_R$$

and can be expressed in terms of the physical fields Z_μ and A_μ and the mixing angle θ_W as follows:

$$-i\overline{\psi}_L\gamma^\mu(gt_L^3\cos\theta_W - g'\frac{Y_L}{2}\sin\theta_W)Z_\mu\psi_L + ig'\overline{\psi}_R\gamma^\mu\frac{Y_R}{2}\sin\theta_W Z_\mu\psi_R$$

which represents the Z^o interaction, and

$$-i\overline{\psi}_L\gamma^\mu(gt_L^3\sin\theta_W + g'\frac{Y_L}{2}\cos\theta_W)A_\mu\psi_L - ig'\overline{\psi}_R\gamma^\mu\frac{Y_R}{2}\cos\theta_W A_\mu\psi_R$$

which represents the photon interaction. The extremely well-verified theory of quantum electrodynamics describes the electromagnetic interaction to be of the form [10]

$$-ie\overline{\psi}\gamma^\mu Q A_\mu\psi = -ie(\overline{\psi}_L\gamma^\mu Q A_\mu\psi_L + \overline{\psi}_R\gamma^\mu Q A_\mu\psi_R) \tag{1.26}$$

where the right-hand side is obtained using Equation 1.3 and the properties of the Dirac matrices. Recalling Equation 1.7, and equating Equation 1.26 with the photon term as given above gives the relation

$$e = g'\cos\theta_W = g\sin\theta_W \tag{1.27}$$

Therefore, we can write the Z^o terms as

$$\frac{-ig}{\cos\theta_W}(c_L\overline{\psi}_L\gamma^\mu Z_\mu\psi_L + c_R\overline{\psi}_R\gamma^\mu Z_\mu\psi_R)$$

with the values of the coupling constants c_L and c_R given by

$$c_L = t_L^3 - Q\sin^2\theta_W, \quad c_R = -Q\sin^2\theta_W \tag{1.28}$$

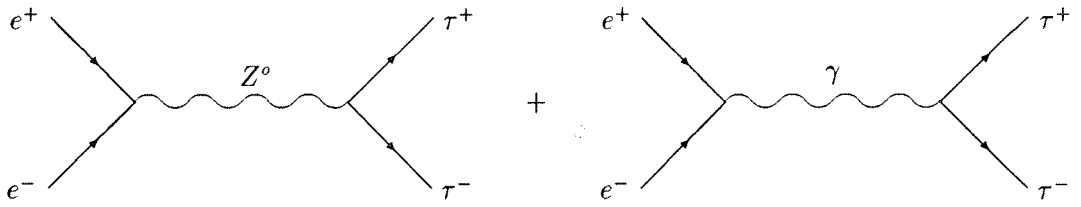

Figure 1.2: *Feynman diagrams for the process* $e^+e^- \rightarrow \tau^+\tau^-$ *at LEP.*

In terms of the particle spinor ψ, the Z^o term can be expressed as

$$\frac{-ig}{\cos\theta_W}\bar{\psi}\frac{1}{2}\gamma^\mu[(c_L + c_R) - (c_L - c_R)\gamma^5]Z_\mu\psi = \frac{-ig}{\cos\theta_W}\bar{\psi}\frac{1}{2}\gamma_\mu(c_V - c_A\gamma_5)Z_\mu\psi \qquad (1.29)$$

Thus, the vector component of the Z^o interaction with fermions is proportional to the vector coupling constant c_V, and the (minus) axial-vector component to the axial-vector coupling constant c_A. The assumption in the Standard Model is that, since each generation is treated equivalently, the same couplings should be found for the same kind of fermions. This is the assumption of *universality* and is to be tested precisely, since deviations from universality would indicate some new physics. For e^-, μ^- and τ^-, we have

$$c_V = -\frac{1}{2} + 2\sin^2\theta_W, \quad c_A = -\frac{1}{2} \qquad (1.30)$$

1.5 Observables sensitive to Z^o-fermion couplings

To actually measure c_V and c_A (and hence θ_W) one can construct several observables. In this section, the derivation of the final state fermion forward-backward charge asymmetry and the average polarisation will be given. The emphasis is on $\tau^+\tau^-$ production, which proceeds via the Feynman diagrams of Figure 1.2.

In general there is interference between these two diagrams, and at energies around the Z^o peak, a resonant enhancement from the Z^o diagram. The differential cross section is given by [10]

$$\frac{d\sigma}{d(\cos\theta)} \propto |\,\mathfrak{M}_\gamma + \mathfrak{M}_Z\,|^2 \qquad (1.31)$$

where θ is the angle between the e^- direction anticlockwise to the τ^- direction. The matrix element for the γ exchange is given by

$$\mathfrak{M}_\gamma = -\frac{e^2}{s}(\bar{\tau}_L\gamma^\mu\tau_L + \bar{\tau}_R\gamma^\mu\tau_R)(\bar{e}_L\gamma^\mu e_L + \bar{e}_R\gamma^\mu e_R) \qquad (1.32)$$

with $1/s$ as the photon propagator factor. The matrix element for Z^o exchange is given by

$$\mathfrak{M}_Z = -\frac{g^2}{\cos^2\theta_W}\frac{1}{(s - M_Z^2 + iM_Z\Gamma_Z)}(c_L^\tau \bar{\tau}_L\gamma^\mu\tau_L + c_R^\tau\bar{\tau}_R\gamma^\mu\tau_R)(c_L^e\bar{e}_L\gamma^\mu e_L + c_R^e\bar{e}_R\gamma^\mu e_R) \tag{1.33}$$

including the propagator factor for the Z^o. Here, $c_{L,R}$ are distinguished for the tau and electron to avoid the assumption of universality.

A simple way of finding $\mid \mathfrak{M}_\gamma + \mathfrak{M}_Z \mid$ is to note that for energies $\gg m_f$, the fermion mass, (as at LEP energies), the left- and right-handed components of the particle spinors are helicity eigenstates. So a term of the form $\bar{e}_L\gamma^\mu e_L$ couples a helicity -1 electron to a helicity -1 electron (or a helicity $+1$ positron) and helicity is conserved. Thus we can have initial states $e_R^- e_L^+$ or $e_L^- e_R^+$ and final states $\tau_R^-\tau_L^+$ or $\tau_L^-\tau_R^+$ (where these are now labels for helicity eigenstates) forming a total of four combinations. The θ dependence of the matrix element can be derived using quantum mechanics for each of the possible combinations (see Figure 1.3).

Simplifying the expressions by defining the quantity

$$r = \frac{g^2 s}{e^2\cos^2\theta_W(s - M_Z^2 + iM_Z\Gamma_Z)} \tag{1.34}$$

the differential cross sections are obtained to be:

$$\frac{d\sigma}{d(\cos\theta)}(e_R^- e_L^+ \to \tau_R^-\tau_L^+) \propto [1 + 2Re(r)c_R^e c_R^\tau + |r|^2 (c_R^e c_R^\tau)^2](1 + \cos\theta)^2 \tag{1.35}$$

$$\frac{d\sigma}{d(\cos\theta)}(e_R^- e_L^+ \to \tau_L^-\tau_R^+) \propto [1 + 2Re(r)c_R^e c_L^\tau + |r|^2 (c_R^e c_L^\tau)^2](1 - \cos\theta)^2 \tag{1.36}$$

$$\frac{d\sigma}{d(\cos\theta)}(e_L^- e_R^+ \to \tau_R^-\tau_L^+) \propto [1 + 2Re(r)c_L^e c_R^\tau + |r|^2 (c_L^e c_R^\tau)^2](1 - \cos\theta)^2 \tag{1.37}$$

$$\frac{d\sigma}{d(\cos\theta)}(e_L^- e_R^+ \to \tau_L^-\tau_R^+) \propto [1 + 2Re(r)c_L^e c_L^\tau + |r|^2 (c_L^e c_L^\tau)^2](1 + \cos\theta)^2 \tag{1.38}$$

With initially unpolarised electron and positron beams, each of these combinations will give an equivalent contribution to the total differential cross section.

1.5.1 Forward-backward charge asymmetry

The forward-backward asymmetry is defined as

$$A_{FB} = \frac{\sigma(\cos\theta > 0) - \sigma(\cos\theta < 0)}{\sigma_{total}} \tag{1.39}$$

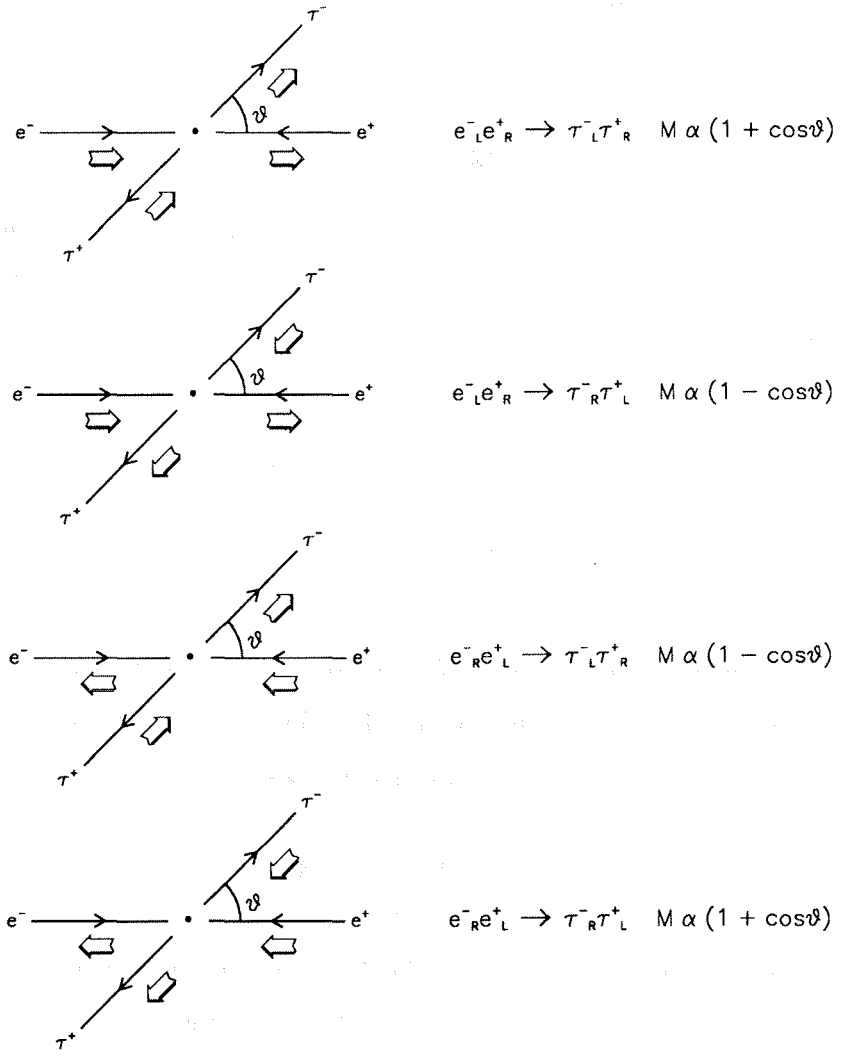

Figure 1.3: *Helicity combinations in the process* $e^+e^- \to \tau^+\tau^-$ *and the* θ *dependence of the matrix element.*

On the Z^o peak, with $Re(r) = 0$ (and neglecting the 1), we have

$$\begin{aligned} A_{FB} &= \frac{3\,(c_R^e c_R^\tau)^2 + (c_L^e c_L^\tau)^2 - (c_R^e c_L^\tau)^2 - (c_L^e c_R^\tau)^2}{4\,(c_R^e c_R^\tau)^2 + (c_R^e c_L^\tau)^2 + (c_L^e c_R^\tau)^2 + (c_L^e c_L^\tau)^2} \\ &= 3\frac{c_V^e c_A^e}{c_V^{e2} + c_A^{e2}}\frac{c_V^\tau c_A^\tau}{c_V^{\tau 2} + c_A^{\tau 2}} = \frac{3}{4}\mathcal{A}_e\mathcal{A}_\tau \end{aligned} \tag{1.40}$$

where the coupling constants c_L and c_R have been expressed in terms of c_V and c_A and the following abbreviations have been used:

$$\mathcal{A}_e = -2\frac{c_V^e c_A^e}{c_V^{e2} + c_A^{e2}}, \quad \mathcal{A}_\tau = -2\frac{c_V^\tau c_A^\tau}{c_V^{\tau 2} + c_A^{\tau 2}} \tag{1.41}$$

The variation of A_{FB} with s in the region of the Z^o peak is shown in Figure 1.4.

1.5.2 Average polarisation

The average polarisation of the tau is defined as

$$A_{pol} = \frac{\sigma_R - \sigma_L}{\sigma_{total}} \tag{1.42}$$

where σ_R is the cross section for producing a right-handed τ^- (or a left-handed τ^+), and similarly for σ_L. Equations 1.35 and 1.37 when integrated over all angles are proportional to σ_R, and Equations 1.36 and 1.38 to σ_L. The polarisation on the Z^o peak is given by the expression

$$A_{pol} = -2\frac{c_V^\tau c_A^\tau}{c_V^{\tau 2} + c_A^{\tau 2}} = \mathcal{A}_\tau \tag{1.43}$$

and thus depends only on the couplings of the tau to the Z^o. A_{pol} is shown as a function of s in Figure 1.4.

The expression for A_{pol} is independent of the θ range covered, if it is symmetric in $\cos\theta$. More generally, the average polarisation as a function of θ is given by

$$\begin{aligned} A_{pol}(\cos\theta) &= \frac{d\sigma_R(\cos\theta) - d\sigma_L(\cos\theta)}{d\sigma_{total}(\cos\theta)} \\ &= \frac{(1+\cos^2\theta)\mathcal{A}_\tau + 2\cos\theta\mathcal{A}_e}{(1+\cos^2\theta) + 2\cos\theta\mathcal{A}_\tau\mathcal{A}_e} \end{aligned} \tag{1.44}$$

where the second expression is valid on the Z^o peak. A_{pol} is shown as a function of $\cos\theta$ on the Z^o peak in Figure 1.4. In this analysis, the region covered was restricted to $47^o < \theta < 133^o$.

Note that since σ_R for a τ^- is equal to σ_L for a τ^+, $A_{pol}(\tau^-) = -A_{pol}(\tau^+)$.

1.5.3 Comments on the observables

One can make the approximation

$$\frac{c_V c_A}{c_V^2 + c_A^2} \approx \frac{c_V}{c_A} \approx 1 - 4\sin^2\theta_W \tag{1.45}$$

using the fact that for leptons, $c_V \ll c_A$. Thus A_{pol} has a linear dependence on $\sin^2\theta_W$, whereas A_{FB} has a quadratic dependence. The uncertainty on a measurement of $\sin^2\theta_W$ from a polarisation uncertainty $\Delta(A_{pol})$ is about a factor 4 less than that corresponding to an identical forward-backward asymmetry uncertainty $\Delta(A_{FB})$. Also, since A_{FB} involves the square of $c_V c_A$ (assuming universality), it gives no information about the relative sign of c_V and c_A.

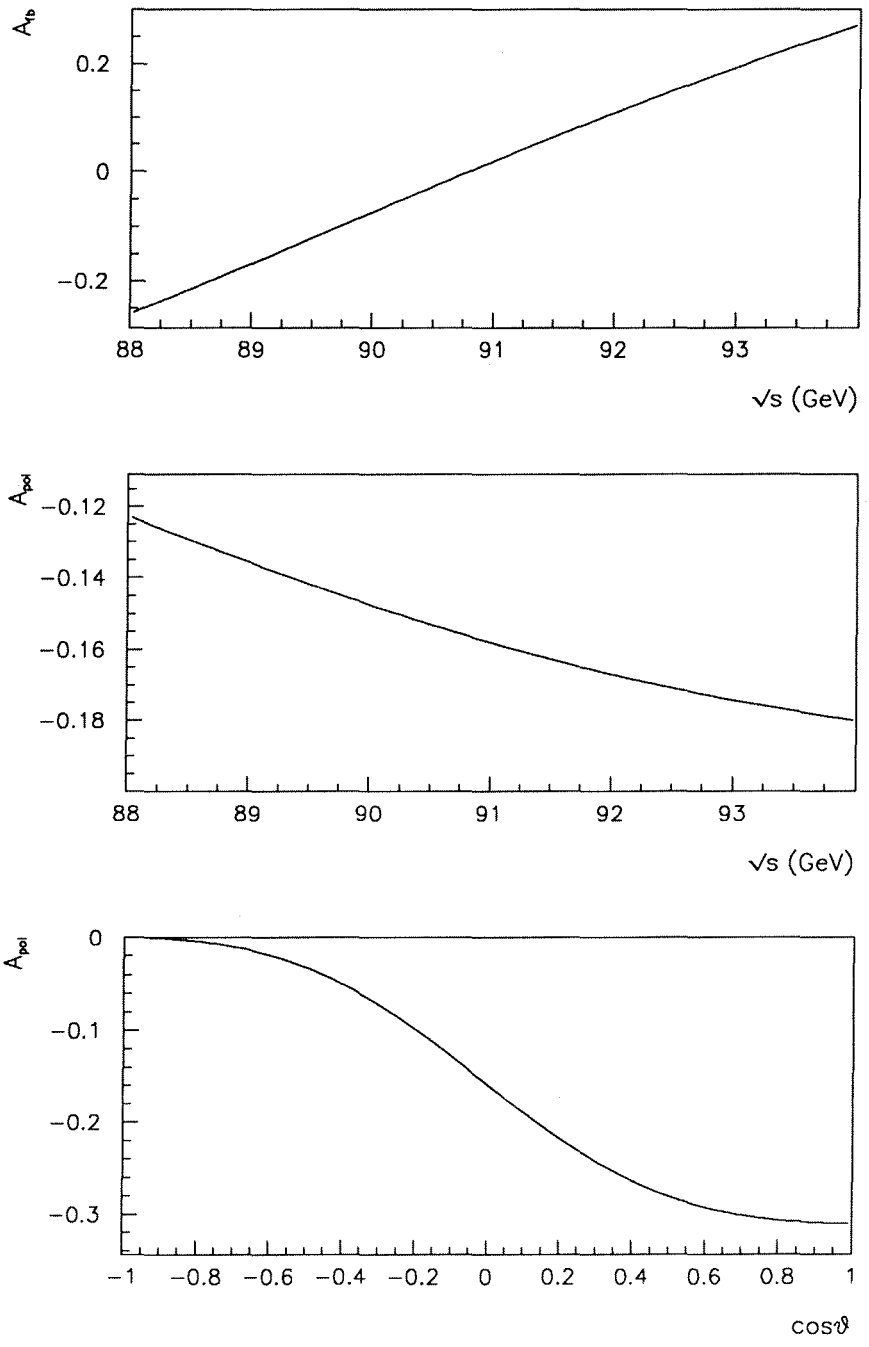

Figure 1.4: *The dependence of A_{FB} and A_{pol} on the centre of mass energy $\sqrt{s}$, and the θ dependence of A_{pol}. The curves are to lowest order only, and the values of the parameters used are: $M_Z = 91$ GeV, $\Gamma_Z = 2.5$ GeV and $sin^2\theta_W = 0.23$.*

Under the transformation $(x, y, z) \rightarrow (-x, -y, -z)$ (the parity operation) particle directions are reversed, whereas spins are not. Therefore, left-handed particles are transformed into right-handed ones and vice versa. Thus A_{pol} which is an observable dealing with the difference in production probabilities of right-handed and left-handed τ^-s does not have the same value in the space-inverted frame and is thus parity-violating. However, A_{FB} depends on the difference in numbers of τ^-s in the forward and backward regions. Production is enhanced in the forward region when the e^- and τ^- have the same helicities and in the backward region when they have opposite helicities (refer to Figure 1.3). Therefore, on changing the handedness of both e^- and τ^-, A_{FB} retains the same value and is thus not parity-violating.

As can be seen from Figure 1.4, A_{FB} is strongly varying with s compared with A_{pol}. This makes it more susceptible to initial state radiative effects. The measurement of A_{FB} for the 1991 tau data sample is given in [11].

1.5.4 s variation of A_{pol}

Equation 1.43 is valid on the Z^o peak. In this analysis, data is collected at a range of energies between 88 and 94 GeV, and this will influence the relation between A_{pol} and $\mathcal{A}_\tau$. The effect is small for two reasons:

1. A_{pol} is not strongly varying with s.

2. Most of the data is collected at peak, and approximately equal amounts above and below.

The shift in $\mathcal{A}_\tau$ has been estimated for the 1991 data sample and is found to be negligible [12].

1.5.5 Effects of higher order processes on A_{pol}

The basic lowest order expression for the polarisation asymmetry on the Z^o peak (Equation 1.43) undergoes some modifications due to higher order processes. The main effects are described below.

Propagator corrections

Propagator effects (see Figure 1.5) have loops which involve all possible particles, and thus, in the Standard Model, will be dependent on the unknown parameters m_t and

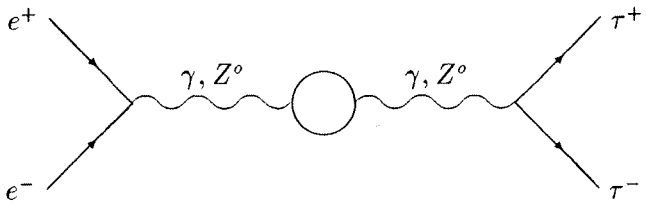

Figure 1.5: *Feynman diagram representing propagator corrections to the process* $e^+e^- \rightarrow \tau^+\tau^-$.

M_H for the masses of the top quark and Higgs boson respectively. In fact, sufficiently precise measurements of observables can place limits on their possible values.

The effect of propagator corrections on the observables which have been described above can be quantified by the replacement of the parameter $\sin^2\theta_W$ by a universal *effective* $\sin^2\theta_{W_{eff}}$ at the energy scale $s = M_Z^2$ [13].

Vertex corrections

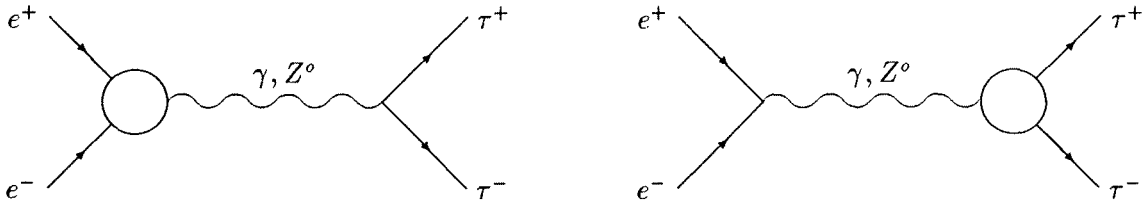

Figure 1.6: *Feynman diagrams representing vertex corrections for the process* $e^+e^- \rightarrow \tau^+\tau^-$.

Vertex corrections (see figure 1.6) can be represented in terms of s-dependent form factors for the vector and axial-vector coupling constants [13]. These give an additional correction to $\sin^2\theta_{W_{eff}}(M_Z^2)$ dependent on the fermion type. For a $Z - l^+ - l^-$ vertex, the correction is [14]

$$\sin^2\theta^l_{W_{eff}}(M_Z^2) = \sin^2\theta_{W_{eff}}(M_Z^2) + 0.0007 \tag{1.46}$$

Bremsstrahlung effects

Initial state and final state radiation can affect A_{pol} in two ways: directly by changing the polarisation state of the tau, or indirectly by changing the kinematic distributions

which are used to measure A_{pol}. The non-negligible contributions are from the direct effect of initial state radiation and the indirect effect of final state radiation [15]. The second effect is taken into account in the fit procedure as the Monte Carlo distributions used to fit the data include the kinematic changes due to radiation. The first effect can be expressed in terms of a multiplicative factor of 0.983 on A_{pol} [16].

The γ exchange and $\gamma - Z^o$ interference terms which have been neglected in the derivation of Equation 1.43 introduce a multiplicative factor of 0.995 on A_{pol} [16].

Both these corrections amount to an experimentally measured value of A_{pol} +0.003 greater than $\mathcal{A}_\tau$.

Chapter 2

Tau physics

The possibility of the existence of a lepton heavier than the muon, and its subsequent decay modes, was already speculated upon by Tsai [17] four years before the actual discovery of the tau [18]. Experimental evidence [19] is consistent with the tau being the third charged lepton with similar properties to the electron and muon. There is also indirect evidence [19] that it is accompanied in its weak decays by its own neutrino, distinct from the electron or muon neutrino. Thus it is well accommodated in the Standard Electroweak Model.

The large mass of the tau (1777 MeV/c^2) allows it several decay modes (see Figure 2.1 for a Feynman diagram representation). Around 99.9 % of the decays are into 1 or 3 charged particles, with accompanying neutrals (neutrinos, photons and π^0s). The branching ratios for the main decay modes are given in Table 2.1 [9]. An accurate determination of the tau branching ratios, could, if discrepancies show up between prediction and observation, indicate the presence of 'new' physics. At present, there seems to be some uncertainty over the measurements of some of the decay modes, with inconsistent results between different experiments. For instance, ALEPH give the branching ratio for the mode $\tau^- \rightarrow h^- 2\pi^0 \nu_\tau$ where h stands for a pion or kaon as 10.38 $\pm$ 1.05 % [20] whereas Crystal Ball find a value of 5.6 $^{+1.8}_{-1.1}$ % [21]. Another inconsistency occurs in the $\tau^- \rightarrow h^- h^- h^+ \nu_\tau$ mode, with ALEPH quoting a branching fraction of 9.49 $\pm$ 0.73 % [20], and an older result from DELCO giving 5.4 $\pm$ 1.0 % [22]. Discrepancies of this kind result in some experiments observing that their exclusive measurements do not or would not add up to 100 % as expected if all the tau decay modes are known, while others see no such difficulty. Thus further, more precise measurements are required for the tau branching ratios, and they should agree with the theoretical

expectations (where given).

Another important area concerns the relationship between the tau lifetime, tau mass and leptonic branching ratios (see Section 2.1) which could indicate a deviation from lepton universality. Here, precise measurements of the branching ratios for $\tau^- \rightarrow \mu^- \bar{\nu}_\mu \nu_\tau$ and $\tau^- \rightarrow e^- \bar{\nu}_e \nu_\tau$, and of the tau lifetime are essential.

Parity is violated in tau decays since only left-handed neutrinos (or right-handed antineutrinos) are produced, and hence the decay distributions depend on the tau spin direction. This enables measurements of the tau polarisation to be performed. This is further explained in Section 2.3 with reference to the muon decay mode.

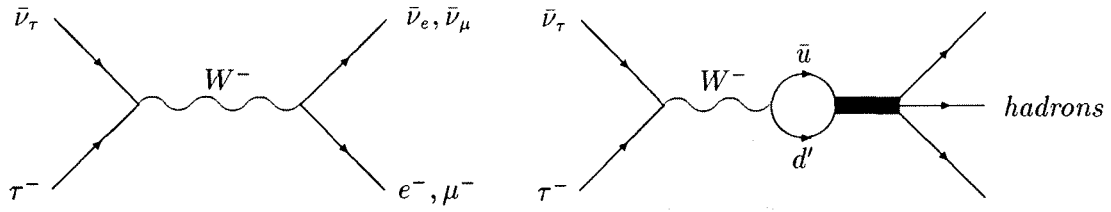

Figure 2.1: *Feynman diagrams representing the tau decay processes into leptonic (left) and hadronic decay modes.*

Decay mode	Branching ratio (%)
$\tau^- \rightarrow \mu^- \bar{\nu}_\mu \nu_\tau$	17.58 ± 0.27
$\tau^- \rightarrow e^- \bar{\nu}_e \nu_\tau$	17.93 ± 0.26
$\tau^- \rightarrow \pi^- \nu_\tau$	11.6 ± 0.4
$\tau^- \rightarrow \rho^- \nu_\tau$	24.0 ± 0.6
$\tau^- \rightarrow K^- \nu_\tau$	0.67 ± 0.23
$\tau^- \rightarrow K^{*-} \nu_\tau$	1.42 ± 0.18
$\tau^- \rightarrow h^- 2\pi^0 \nu_\tau$	10.3 ± 0.9
$\tau^- \rightarrow h^- (> 2\pi^0) \nu_\tau$	2.7 ± 0.9
$\tau^- \rightarrow h^- h^- h^+ \nu_\tau$	8.4 ± 0.4
$\tau^- \rightarrow h^- h^- h^+ (> 0\pi^0) \nu_\tau$	5.3 ± 0.4

Table 2.1: *Experimental values for main tau branching ratios. h^- indicates π^- and K^- modes are not distinguished.*

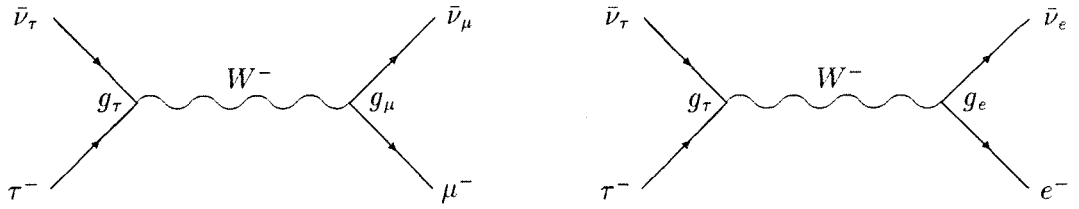

Figure 2.2: *Feynman diagrams for the processes* $\tau^- \rightarrow \mu\bar{\nu}_\mu\nu_\tau$ *and* $\tau^- \rightarrow e\bar{\nu}_e\nu_\tau$.

2.1 Leptonic decay modes and universality tests

The purely leptonic decays of the tau, $\tau^- \rightarrow e^-\bar{\nu}_e\nu_\tau$ and $\tau^- \rightarrow \mu^-\bar{\nu}_\mu\nu_\tau$ have a well-defined matrix element in the Standard Model, with the $V-A$ form for the charged current interaction (see Section 1.3). Thus the partial widths and decay distributions are precisely calculable. The decay width for $\tau^- \rightarrow l^-\bar{\nu}_l\nu_\tau$ where $l = e, \mu$ assuming a standard weak interaction (and massless neutrinos[1]) is calculated to be [23]

$$\Gamma(\tau^- \rightarrow l^-\bar{\nu}_l\nu_\tau) = \frac{g_\tau^2 g_l^2 m_\tau^5}{192\pi^3} F\left(\frac{m_l^2}{m_\tau^2}\right)\left(1+\frac{3}{5}\frac{m_\tau^2}{m_W^2}\right)\left[1+\frac{\alpha(m_\tau)}{2\pi}\left(\frac{25}{4}-\pi^2\right)\right] \qquad (2.1)$$

where g_τ, g_l are the effective weak coupling constants at the τ^-–W–$\bar{\nu}_\tau$ and l^-–W–$\bar{\nu}_l$ vertices respectively (see Figure 2.2) and m_τ, m_l and m_W are the masses of the tau, the lepton and the W boson respectively. The function

$$F(y) = 1 - 8y + 8y^3 - y^4 - 12y^2 \ln y \qquad (2.2)$$

is a phase space factor taking into account the finite mass of the lepton. The term in parentheses corrects for the non-zero momentum transfer in the W propagator, and the term in square brackets takes into account most of the electromagnetic corrections to the decay process, including the radiation of real photons. Remaining electroweak corrections are absorbed into the effective g_ls. The electromagnetic coupling constant is evaluated at the tau mass scale and is given by

$$\alpha(m_\tau) \approx \frac{1}{133.3} \qquad (2.3)$$

Using the following values for the particle masses m_e [9], m_μ [9], m_τ [24] and m_W [9]:

$$m_e = 0.511 \text{ MeV/c}^2 \qquad (2.4)$$

$$m_\mu = 105.658 \text{ MeV/c}^2 \qquad (2.5)$$

[1]The ν_τ mass limit of 35 MeV/c^2 at 95 % C.L. [9] introduces a maximum correction of 0.04 %.

$$m_\tau = 1776.9^{+0.4}_{-0.5}\ \mathrm{MeV/c^2} \tag{2.6}$$

$$m_W = 80.22 \pm 0.26\ \mathrm{GeV/c^2} \tag{2.7}$$

where the errors on the electron and muon mass are negligible, the ratio of the muon and electron branching ratios is given to be:

$$\frac{Br(\tau^- \to \mu^- \bar{\nu}_\mu \nu_\tau)}{Br(\tau^- \to e^- \bar{\nu}_e \nu_\tau)} = 0.9726 \left(\frac{g_\mu}{g_e}\right)^2 \tag{2.8}$$

This relation can be used as a test of the equality of the couplings g_μ and g_e (the uncertainty on the factor 0.9726 is negligible since it is purely a phase space factor arising from the difference in the masses of the electron and muon).

The decay width for the process $\mu^- \to e^- \bar{\nu}_e \nu_\mu$ is also described by Equation 2.1 with the appropriate replacements:

$$\Gamma(\mu^- \to e^- \bar{\nu}_e \nu_\mu) = \frac{g_\mu^2 g_e^2 m_\mu^5}{192\pi^3} F\left(\frac{m_e^2}{m_\mu^2}\right)\left(1 + \frac{3}{5}\frac{m_\mu^2}{m_W^2}\right)\left[1 + \frac{\alpha(m_\mu)}{2\pi}\left(\frac{25}{4} - \pi^2\right)\right] \tag{2.9}$$

with the electromagnetic coupling constant evaluated at the muon mass scale to be

$$\alpha(m_\mu) \approx \frac{1}{136} \tag{2.10}$$

The decay width for $\mu^- \to e^- \bar{\nu}_e \nu_\mu$ is related to the muon lifetime by

$$\tau_\mu = \frac{\hbar}{\Gamma(\mu^- \to e^- \bar{\nu}_e \nu_\mu)} \tag{2.11}$$

For the tau lifetime we have instead

$$\tau_\tau = \frac{\hbar Br(\tau^- \to \mu^- \bar{\nu}_\mu \nu_\tau)}{\Gamma(\tau^- \to \mu^- \bar{\nu}_\mu \nu_\tau)} \tag{2.12}$$

since several decay modes are open to the tau. Thus,

$$Br(\tau^- \to \mu^- \bar{\nu}_\mu \nu_\tau) = \frac{\tau_\tau}{\tau_\mu}\frac{\Gamma(\tau^- \to \mu^- \bar{\nu}_\mu \nu_\tau)}{\Gamma(\mu^- \to e^- \bar{\nu}_e \nu_\mu)} \tag{2.13}$$

This can be simplified by evaluating the terms describing corrections in the expressions for the widths to become:

$$Br(\tau^- \to \mu^- \bar{\nu}_\mu \nu_\tau) = 0.9730 \frac{\tau_\tau}{\tau_\mu}\left(\frac{m_\tau}{m_\mu}\right)^5 \left(\frac{g_\tau}{g_e}\right)^2 \tag{2.14}$$

Again, the uncertainty on the factor 0.9730 is negligible compared with the uncertainties on the other terms in this expression.

Hence it is seen from Equations 2.8 and 2.14 that the measurement of $Br(\tau^- \to \mu^- \bar{\nu}_\mu \nu_\tau)$

can give information on the ratios $(g_\mu/g_e)^2$ and $(g_\tau/g_e)^2$. With the Standard Model assumption of generation-independent couplings, these ratios should be consistent with 1, and and are deduced in Chapter 6 using the measurement made of $Br(\tau^- \to \mu^- \bar{\nu}_\mu \nu_\tau)$.

2.2 Hadronic decay modes

The calculation of the partial decay width for the decay $\tau^- \to \bar{u}d'\nu_\tau$ is complicated by the quantum chromodynamic corrections to the $\bar{u}-W-d'$ vertex, which are large at the mass scale of the tau. Recent work [25] has considered the corrections up to $O(\alpha_s^3)$ where α_s is the strong coupling constant.

The subsequent hadronisation of the quarks is dominated by resonances, and no absolute predictions of the hadronic decay widths exists. Rather, relative predictions can be made by invoking results concerning related processes. We can assume that the hadronic current at the $\bar{u}-W-d'$ vertex has vector and axial-vector components, each of which can be strangeness changing or conserving [17]. Specifically, G-parity considerations indicate that states with an even number of pions are produced through a vector current interaction, and the conserved vector current principle (CVC) [26] is used to relate processes such as $\tau^- \to \rho^-\nu_\tau \to \pi^-\pi^0\nu_\tau$, $\tau^- \to \pi^-\pi^-\pi^+\pi^0\nu_\tau$ and $\tau^- \to \pi^-\pi^0\pi^0\pi^0\nu_\tau$ to the processes $e^- + e^+ \to \rho^0 \to \pi^-\pi^+$, $e^- + e^+ \to \pi^-\pi^-\pi^+\pi^+$ and $e^- + e^+ \to \pi^-\pi^+\pi^0\pi^0$ respectively. States with odd numbers of pions such as $\tau^- \to \pi^-\nu_\tau$ and $\tau^- \to a_1^-\nu_\tau \to \pi^-\pi^-\pi^+\nu_\tau, \pi^-\pi^0\pi^0\nu_\tau$ are produced through an axial-vector current interaction and do not have the equivalent of the CVC principle. However, we can relate the widths for $\tau^- \to \pi^-\nu_\tau$ and $\tau^- \to K^-\nu_\tau$ to the measurements for $\pi^- \to \mu^-\nu_\mu$ and $K^- \to \mu^-\nu_\mu$ assuming universality at the $l^-W-\bar{\nu}_l$ vertex. Isospin considerations [27] give equal partial widths for the 1 charged pion and 3 charged pion states of the a_1 resonant decay.

In general, where definite predictions exist, good agreement is observed experimentally for the hadronic decay modes of the tau. A more complete description can be found in [19, 27].

2.3 Tau decays as polarisation analysers

The observed decay products of the tau contain information on the tau polarisation because of the restrictions on the allowed helicities of the particles emitted. In particu-

lar, only left-handed neutrinos and right-handed antineutrinos can be emitted in $V-A$ theory.

To illustrate this effect, consider the following simple situation in which a τ^- decays in its rest frame into a μ^-, $\bar{\nu}_\mu$ and ν_τ along its direction of spin, and where the μ^- has maximum energy. Then, by conservation of momentum, the $\bar{\nu}_\mu$ and ν_τ must be emitted opposite to the μ^-. The four possible scenarios that conserve angular momentum for this case (taking into account the allowed neutrino helicities) are given in Figure 2.3. Diagrams (c) and (d) are highly suppressed because the μ^- is left-handed to a factor v/c in $V-A$ theory [28], and v/c is close to 1 because of the much smaller mass of the muon compared with the tau. A boost applied to diagrams (a) and (b) then results, in the lab frame, in *either* a tau helicity of $+1$ and a muon momentum close to zero *or* in a tau helicity of -1 and a muon momentum close to maximum, i.e. the muon has different momenta depending on the tau polarisation.

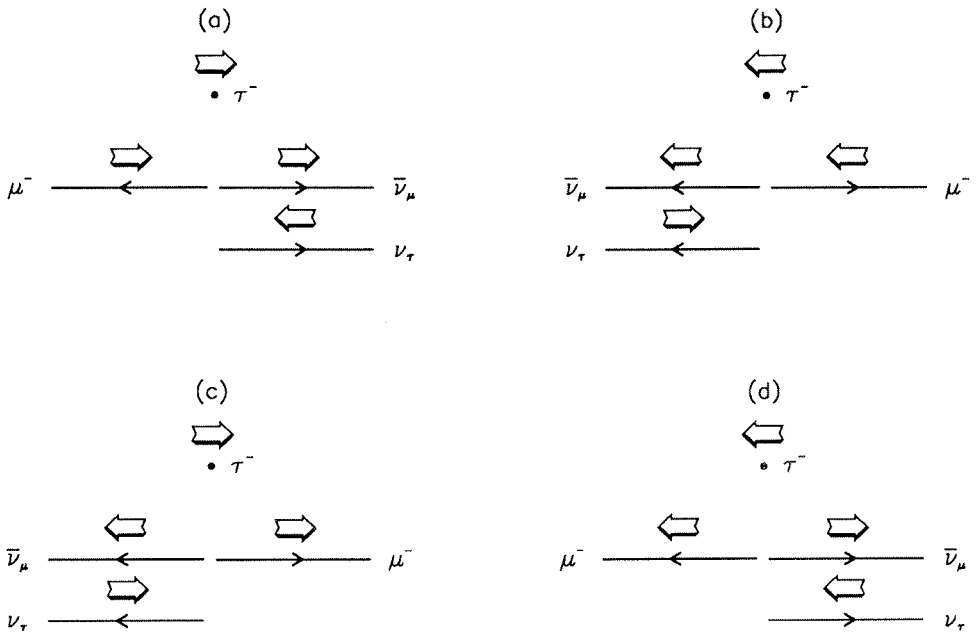

Figure 2.3: *Spin configurations in a kinematically simplified* $\tau^- \to \mu^-\bar{\nu}_\mu\nu_\tau$ *decay. The thin arrows represent the momentum direction of the particle, and the thick arrows its spin direction.*

In practice, the muon is emitted at varying angles and energies, resulting in a rather lower sensitivity to the tau polarisation. The general decay distribution in the tau rest

frame for a tau polarisation P is given by [17]

$$\frac{dN}{dx\,d(\cos\theta)} = x^2[(3-2x) + \mathrm{P}(1-2x)\cos\theta] \tag{2.15}$$

where θ is the angle between the muon momentum direction and the tau spin direction, and x is the muon momentum as a fraction of its allowed maximum (which is $\approx \frac{1}{2}m_\tau$). Boosting along the tau spin direction gives the observable distribution in the lab frame as [29]

$$\frac{dN}{dy} = \frac{1}{3}[(5-9y^2+4y^3) + \mathrm{P}(1-9y^2+8y^3)] \tag{2.16}$$

for a tau longitudinal polarisation P in terms of y, the fractional muon momentum in the lab frame. The above expressions neglect the finite muon mass, which gives a small correction at low y.

The distribution for the charge conjugate decay $\tau^+ \rightarrow \mu^+\nu_\mu\bar{\nu}_\tau$ is given by

$$\frac{dN}{dy} = \frac{1}{3}[(5-9y^2+4y^3) - \mathrm{P}_{\tau+}(1-9y^2+8y^3)] \tag{2.17}$$

if one assumes the decay is CP invariant. Thus, since $\mathrm{P}_{\tau-} = -\mathrm{P}_{\tau+}$, $\tau^+ \rightarrow \mu^+\nu_\mu\bar{\nu}_\tau$ decays can also be used in the measurement of A_{pol}.

The muon momentum distributions for P = -1 and P = $+1$ are shown in Figure 2.4, together with the distributions for an unpolarised tau sample and a sample with A_{pol} = -0.16, which is the Standard Model prediction for a value of $\sin^2\theta_W$ of 0.23 (see Equations 1.43 and 1.45).

The muon decay mode, with three particles in the final state, has a much reduced sensitivity[2] to the tau polarisation compared with two body decays. The $\tau^- \rightarrow \pi^-\nu_\tau$ channel is the most sensitive mode, since the pion is a spin 0 particle. The $\tau^- \rightarrow \rho^-\nu_\tau$ and $\tau^- \rightarrow a_1\nu_\tau$ channels also have lower sensitivities than the pion channel due to the possibility of the spin 1 hadron being in either of two helicity states (0, -1). Some sensitivity is regained if one makes use of the information on the hadron spin state given by its subsequent decay products. The actual weight that a particular decay mode carries in an overall tau polarisation measurement using all the modes must take into account the sensitivity of the mode, its branching ratio and selection efficiency, the

[2]The ideal sensitivity of a decay mode depends on the functional form of the decay distribution and can be defined as $S = (\Delta A_{pol}\sqrt{N})^{-1}$, where ΔA_{pol} is the uncertainty on the measurement of A_{pol} and N is the number of events used in the measurement, taken in the limit of infinite statistics [29].

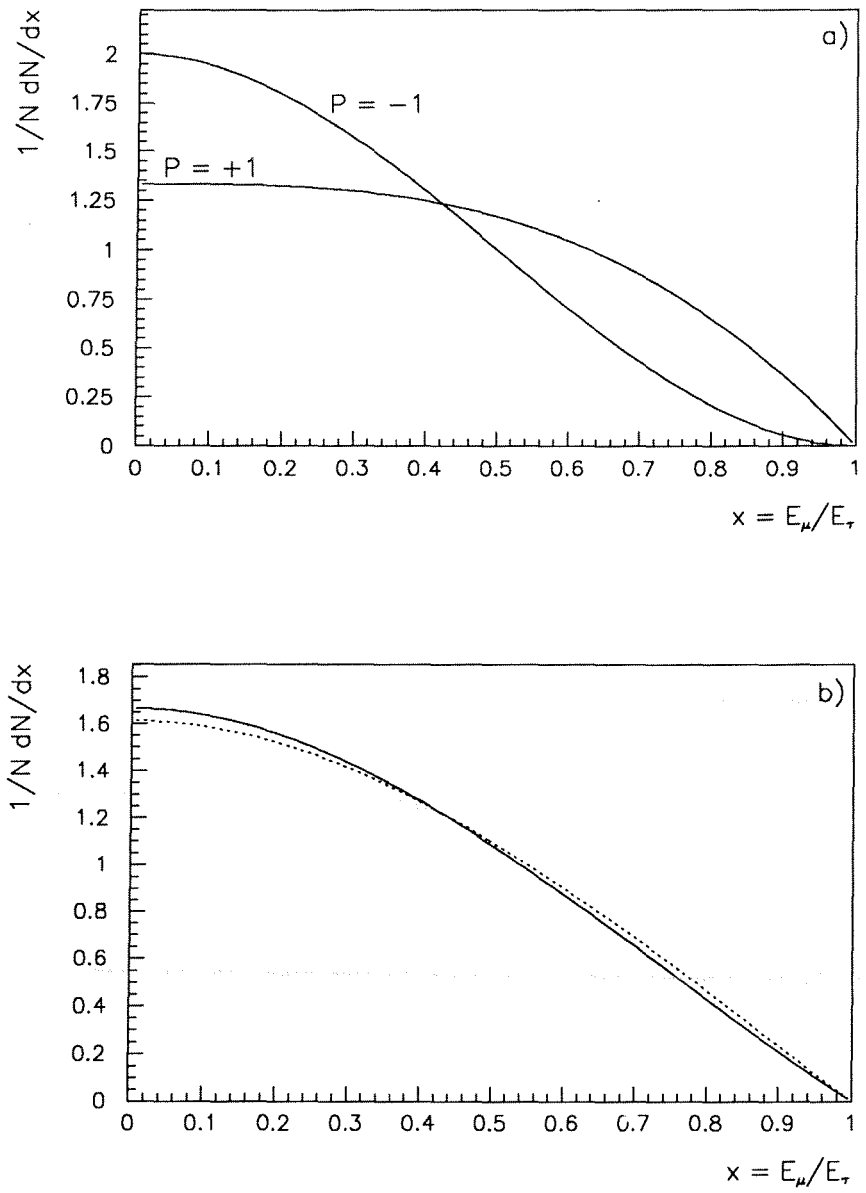

Figure 2.4: *The muon momentum distributions for a) $P = -1$ and $P = +1$, and b) for a tau sample with $A_{pol} = 0$ and $A_{pol} = -0.16$ (dashed line).*

last being analysis-dependent. Ideal sensitivities and weights for the main tau modes are given in Table 2.2.

Decay mode	Sensitivity	Weight
$\tau^- \to \pi^- \nu_\tau$	0.60	1.0
$\tau^- \to \rho^- \nu_\tau$	0.52	1.6
$\tau \to a_1 \nu_\tau$	0.44	0.4
$\tau^- \to e^- \bar{\nu}_e \nu_\tau$	0.22	0.2
$\tau^- \to \mu^- \bar{\nu}_\mu \nu_\tau$	0.22	0.2

Table 2.2: *Ideal sensitivities and weights (relative to the pion channel) of tau decay modes in the polarisation measurement, using the methods of measurement outlined in* [29], *and in the case of the* a_1, *in* [30].

Chapter 3

The Apparatus

3.1 The LEP collider

The LEP (**L**arge **E**lectron-**P**ositron) collider [3] was built to produce Z^0s and W^+W^- pairs for a precision study of the electroweak interaction. After careful studies of the parameters required and costs involved in achieving them, a 26.66 km circumference tunnel capable of providing centre of mass energies of up to 200 GeV (comfortably above the threshold for W^+W^- pair production) was decided upon, and its construction commenced in 1982. The first phase of operation is at energies around the Z^0 resonance, first collisions being observed in summer 1989. On addition of superconducting RF cavities the second phase energies are expected to be achieved in 1995.

Pre-injection phase

Electrons produced by thermionic emission are accelerated in a LEP injector linac (LIL) to 200 MeV before hitting a positron converter target. The electrons and positrons are then accelerated in a second linac to 600 MeV before passing to a 600 MeV accumulator (EPA). From the accumulator they are injected into two colliders which were originally built for other experiments before LEP – the Proton Synchroton (PS) which takes the beams to 3.5 GeV followed by the Super Proton Synchroton (SPS) which accelerates to 20 GeV before injecting into LEP for acceleration to final energies [31] (see Figure 3.1).

The LEP ring

The tunnel consists of 8 curved sections of bending radius ρ = 3096 m with 8 straight sections in between. The RF acceleration system, consisting of 128 5-cell room tem-

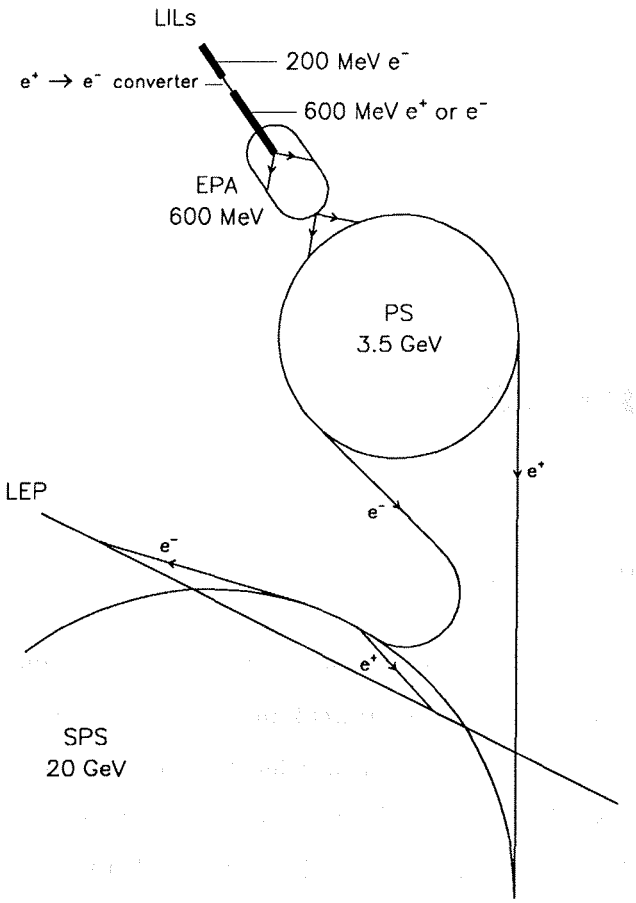

Figure 3.1: *The LEP injector scheme.*

perature cavities powered by 16 1 MW klystrons, is located in the straight sections. Power loss due to heating is reduced by coupling each accelerating cavity to a spherical low-loss storage cavity. The four detectors operating at LEP (ALEPH, DELPHI, L3 and OPAL) are housed in alternate straight sections. Each curved section contains 31 standard cells, with a cell consisting of in order: a defocussing quadrupole, a vertical orbit correcting magnet, six bending dipoles, a focussing sextupole, a focussing quadrupole, a horizontal orbit correcting magnet, a further six dipoles and a defocussing sextupole [32]. This complex system is essential to achieve the bunch containment required, both in energy and position.

Vacuum tube

To achieve a long beam lifetime (typically of a few hours) particle losses due to collisions with residual gas molecules in the tube must be kept to a minimum. The tube is pumped out into a channel containing a non-evaporable getter strip, which is made of a material

forming stable compounds with most active gases [32]. The pressure in the tube is of the order 10^{-9} torr.

Beam dimensions and luminosity

The RF field has the effect of focussing particles longitudinally into bunches as the energy is increased. Particles perform *synchroton* oscillations longitudinally and in energy about the nominal trajectory. Similarly the magnetic forces cause *betatron* oscillations in the radial (x) and vertical (y) directions. Synchroton radiation and its random nature combine to give the bunch a gaussian form in space and energy [33]. At an energy per beam of 45.6 GeV, the typical energy spread in the bunch is given by $\sigma(E)/E$ = 7 x 10^{-4} [32]. The bunch length is 1 to 2 cm [32], and dimensions in x and y (related to betatron wavelengths β_x and β_y) are given by $\sigma_x \approx 140$ μm and $\sigma_y \approx 7$ μm in the interaction regions [34].

The beam intensity can be quantified by the *luminosity* L which is defined as [32]

$$L = \frac{N^2 f_{rev} n_b}{4\pi\sigma_x\sigma_y} \tag{3.1}$$

where N is the number of particles in each bunch (assumed equal for electron and positron bunches), f_{rev} is the revolution frequency for a bunch and is 1.1 x 10^4 Hz at LEP and n_b is the number of electron(positron) bunches. Currently LEP operates with 4 electron bunches and thus there is the possibility of collisions at eight points in the collider. Collisions at unwanted points are avoided by means of electrostatic separators. σ_y is reduced just before the particles reach the interaction points by strong focussing superconducting quadrupoles. Typical luminosity values are of the order 5 x 10^{30} $cm^{-2}s^{-1}$ [54].

The luminosity is related to the event rate for a particular process by

$$\frac{dN}{dt} = \sigma L \tag{3.2}$$

where σ is the cross section for the process. The Bhabha cross section at low angles which is dominated by t-channel scattering is used to measure the integrated luminosity run by run (see Section 3.2.7 for further details).

The energy of the beam is measured from the resonant depolarisation of the electron beam at an energy of 46.5 GeV to $\pm$ 5 MeV [35].

3.2 The DELPHI detector

DELPHI, a **D**etector for **L**epton, **P**hoton and **H**adron **I**dentification [4] is situated 100 m below ground at one of the four designated areas for electron-positron collisions in the LEP collider. The detector is in three separate components, a cylindrical *barrel* region and two approximately conical *endcap* regions to provide altogether almost full coverage of the solid angle. The DELPHI coordinate system is shown in Figure 3.2. The incoming e^- beam is in the direction of $+z$. The polar angle θ is measured from the $+z$ axis. The $+x$ direction is horizontally towards the centre of the LEP ring, and the $+y$ direction is vertically upwards. The azimuthal angle ϕ is measured anticlockwise from the $+x$ axis. The radius r is measured in the $x-y$ plane outwards from the origin. Coordinates in the barrel region are conveniently expressed in terms of r, ϕ, θ and z, and in the endcap regions, in terms of x, y and z. The detector components in the barrel have varying polar angle coverage but conventionally the barrel region covers the angular range $43° < \theta < 137°$.

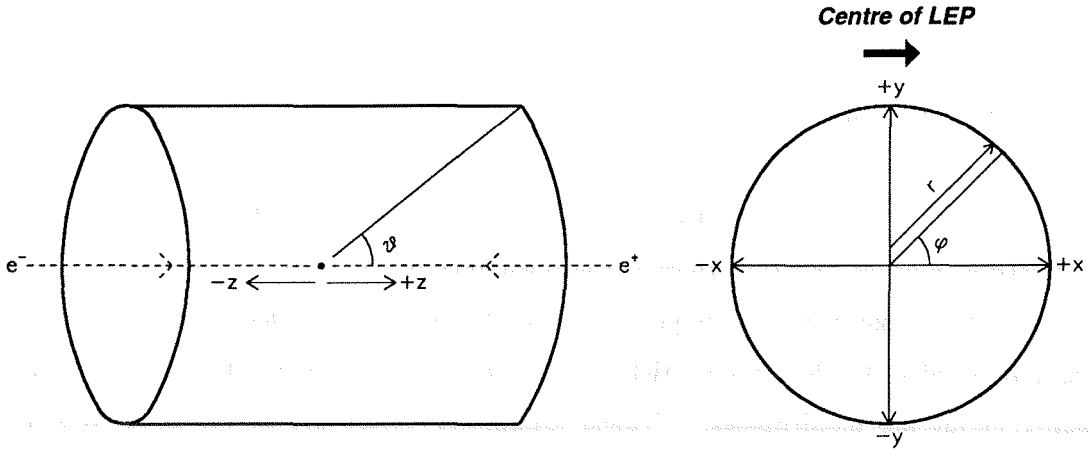

Figure 3.2: *The DELPHI coordinate system.*

DELPHI has several tracking subdetectors which provide an accurate reconstruction of the passage of charged particles through the detector. Electromagnetic and hadronic calorimeters allow shower reconstructions and energy measurements for interacting particles, or give signals for minimum ionising particles. Muon chambers are placed outermost to allow identification of muons which pass through the calorimeters without interacting. Luminosity monitors tag Bhabha events providing run by run luminosity

values for the eventual calculation of cross sections. Unique amongst the LEP detectors are the Ring Imaging Cherenkov detectors which provide π-K-p separation. Longitudinal and transverse views of the detectors are shown in Figure 3.2. The components of DELPHI playing a part in the analysis carried out in this thesis are described below. A description of all the subdetectors in DELPHI can be found in [4].

3.2.1 Beam pipe

The beam pipe surrounding the interaction region is chosen with dimensions and material to best meet several requirements. Prime among these are that the Microvertex detector should be able to start as close to the interaction region as possible to limit the effects of multiple scattering in the material and to allow a good extrapolation of tracks and reconstruction of event vertices. However, levels of synchroton radiation which is emitted at low angles to the circulating beam and upon entering the detector could degrade the pattern recognition must be kept under control. The material should be of low Z to limit particle interactions with the beam pipe walls and photon conversions.

The present beam pipe was installed at the end of the 1990 run to replace the original larger one. It is a beryllium cylinder 570 mm long with an internal diameter of 106 mm and a thickness of 1.4 mm [4].

3.2.2 Tracking detectors

Track reconstruction in DELPHI normally encompasses information from several tracking detectors. Because of the presence of the Cherenkov detectors, there is a lever arm tracking detector placed after them – the Outer Detector in the barrel region and Forward Chamber B in the endcap regions – in order to improve the momentum resolution, especially for dimuon and Bhabha events.

The Microvertex detector

The Microvertex detector (VD) [36] is a three layer silicon strip detector installed to give very precise $r\phi$ measurements for tracks close to the interaction region. The *closer* layer is at an average radius of 6.3 cm from the origin, the *inner* layer at 9.0 cm and the *outer* layer at 11.0 cm. Each layer consists of 24 modules in ϕ, and each module has 4 plaquettes along z. There is between 10 and 15 % overlap between modules. The inner and outer layers are 24 cm long and the closer layer is 22 cm long, providing

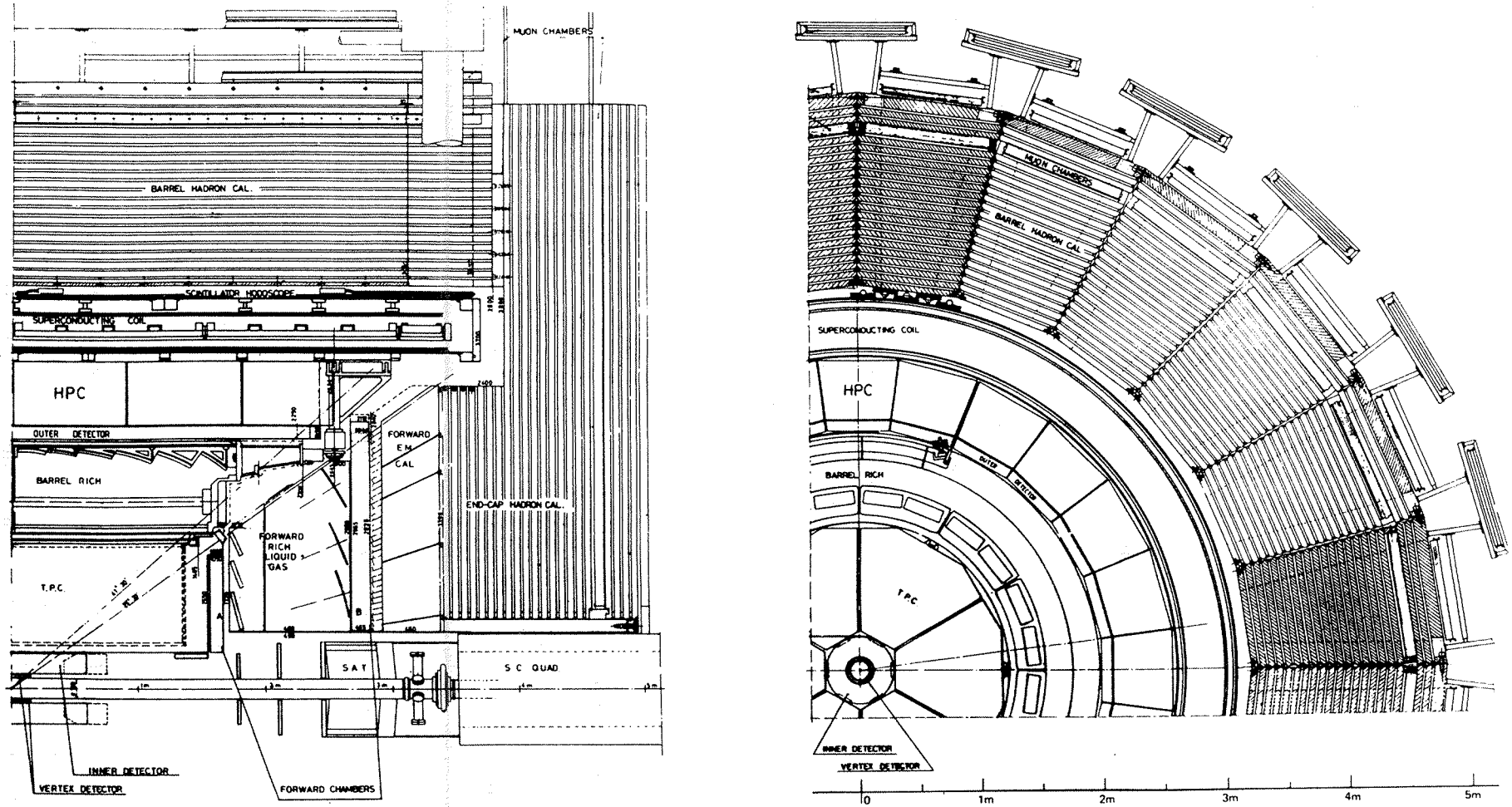

Figure 3.3: *a) Longitudinal and b) transverse view of DELPHI.*

polar angle coverage from 43° to 137° for all three layers and from 30° to 150° for the closer layer (see Figure 3.4). The material of the detector represents 0.9 to 2.0 % of a radiation length – thus conversions in the detector are at a low level. The silicon strips in the plaquettes are spaced 25 μm apart parallel to the z axis and alternate strips are read out. The signal-to-noise ratio is typically 15:1.

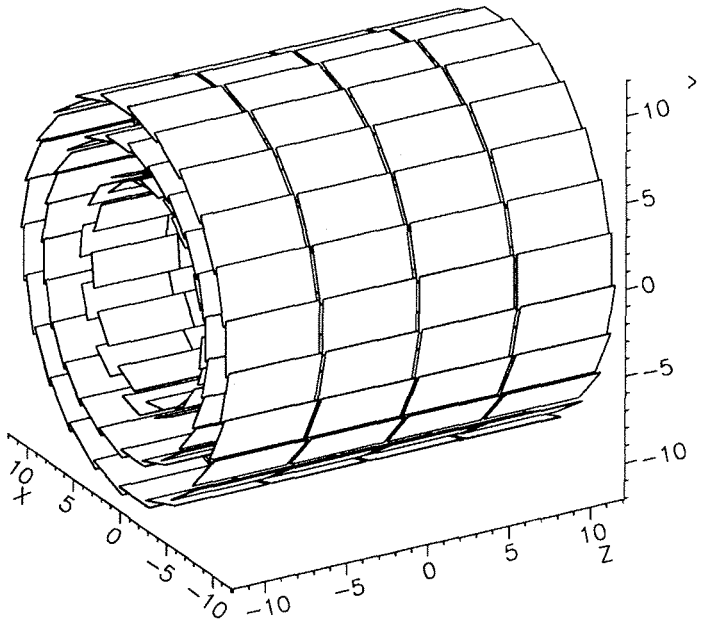

Figure 3.4: *View of plaquettes in the microvertex detector.*

The resolution per point in the VD after a proper alignment of the detector is found to be 8 μm [37] and the two track separation is 100 μm [4]. VD hits are associated to tracks which have first been found by the other tracking detectors and then extrapolated back. A refit of the track is then performed including the VD hits. The efficiency overall for association of a VD hit to an isolated track is found to be 96.4 % [38]. Including the VD hits in the track fit improves the momentum resolution for dimuons from 8 % to 3.5 %.

The Inner detector

The Inner detector (ID) [4, 39] consists of two sections, a jet chamber at a radius of 11.8 cm out to 22.3 cm, and covering polar angles from 17° to 163°, and a trigger chamber from 23 cm to 28 cm covering polar angles from 30° to 150° (see Figure 3.5).

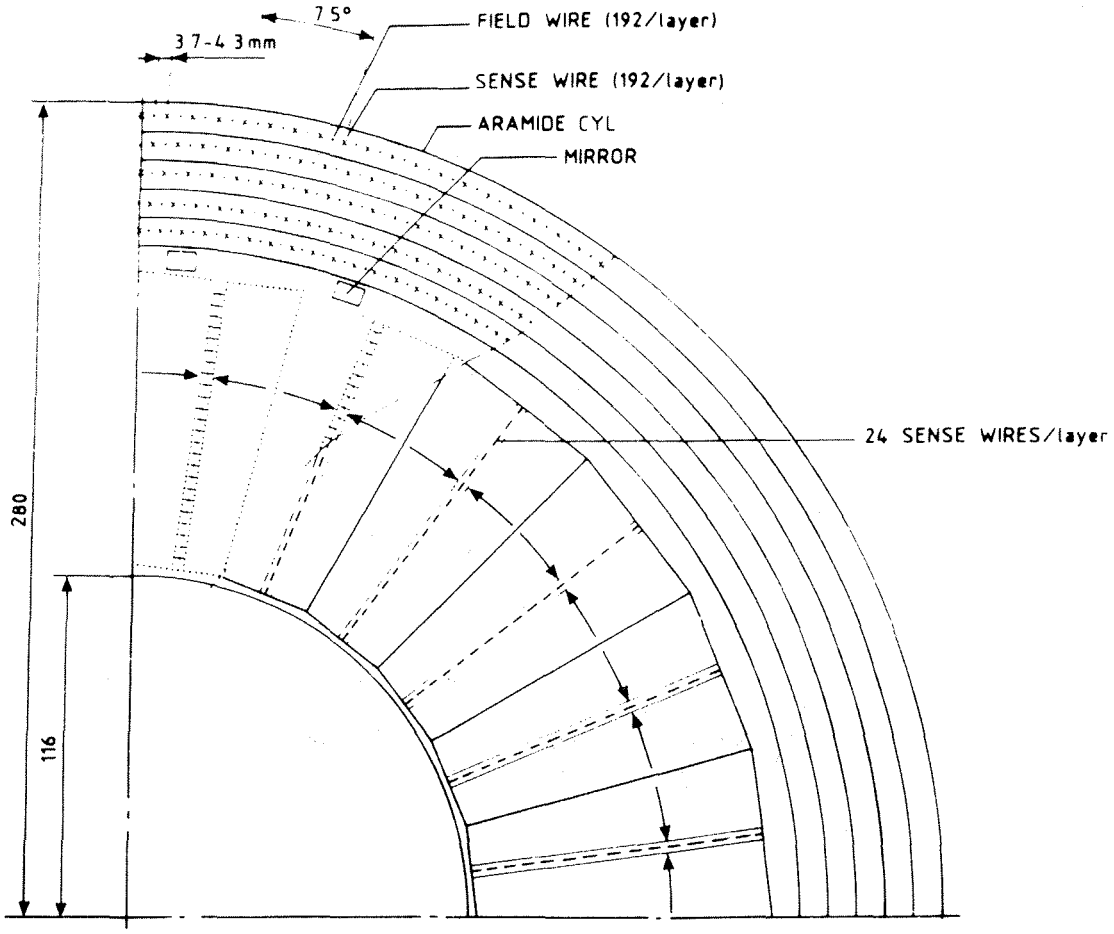

Figure 3.5: *Transverse view of inner detector.*

The jet chamber is a drift chamber consisting of 24 sectors in $r\phi$ each with 24 central sense wires. The gas mixture and electric field strength have been chosen such that the drift velocity is proportional to r. Thus a set of coincident pulses is an indication of a track originating from the interaction region and this fact can be implemented in a trigger. The resolution per point in $r\phi$ is 90 μm.

The trigger chamber consists of five concentric layers of proportional wire detectors. Sense wires 8 mm apart giving a total of 192 wires per layer are alternated with field wires. Reconstruction of hits in the trigger layers resolves the left-right ambiguity which is present in the jet chamber for the hit positions reconstructed from the drift times in the sectors. The time difference between signals received at either end of the sense wires provides information on the z of the tracks with a resolution of around 1 mm. The main function of the trigger layers is to provide a fast pattern recognition of hits

for the first level trigger decision.

The Time Projection Chamber

The Time Projection Chamber (TPC) [4] is the main tracking chamber in DELPHI, covering a radius of 35 cm to 111 cm and polar angles from 20° to 160°. It is constructed in two halves in $+z$ and $-z$, each 130 cm long and operates at a pressure of 1 atmosphere.

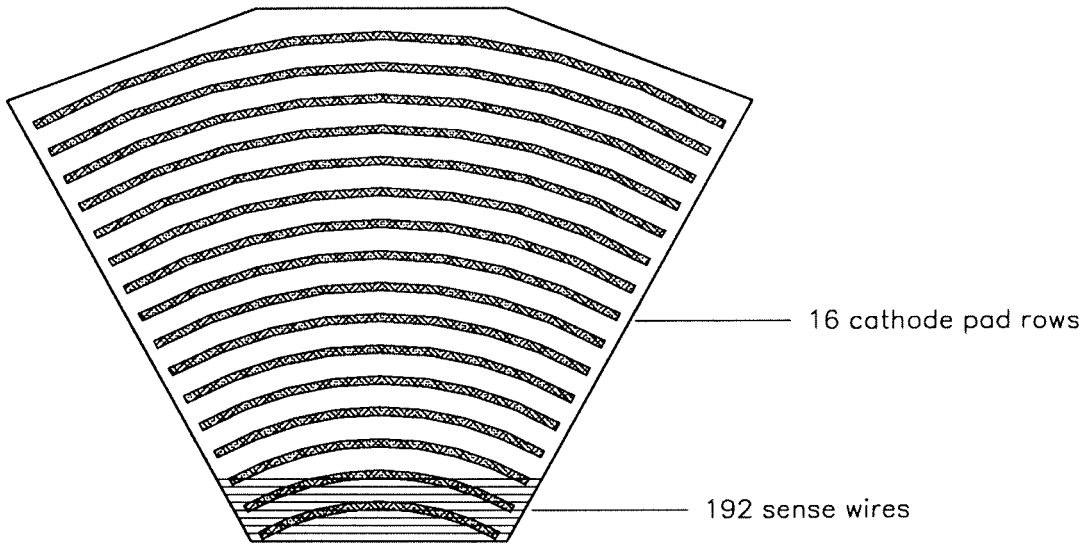

Figure 3.6: *Transverse view of a TPC sector showing the pad rows and the sense wires in front.*

The readout planes at either end of the drift length consist of 6 sectors, each with 192 sense wires with a spacing of 4 mm, and 16 rows of cathode pads (see Figure 3.6). Each row contains a multiple of 16 pads of constant surface area, forming a total of 1680 pads per sector. Electrons drift under the action of a uniform field until they reach a cathode grid 4 mm before the sense wires, onto which they then avalanche. The pad rows define a maximum of 16 points in $r\phi$ for transverse momentum reconstruction and the drift times onto each pad row are used to reconstruct the z (and θ) of the track. The signals induced on the sense wires provide dE/dx information on the tracks, which can be used to separate electrons from pions up to a momentum of around 8 GeV/c. The resolution per point is found to be 230 μm in $r\phi$ and 900 μm in z. The two track separation is 1.5 cm.

The Outer detector

The Outer detector (OD) [4] is situated at a radius of 1.98 m from the origin and covers polar angles from 43° to 137°. Its main functions are to give fast trigger information as well as improve the momentum resolution in a lever arm role. It consists of 24 planks along z each with 5 layers of drift tubes. Each drift tube is made of aluminium with a cross section of 1.75 cm x 1.75 cm. The drift tubes are staggered to avoid left-right ambiguity and neighbouring planks are interlocking, reducing the gaps in ϕ (see Figure 3.7). All layers provide $r\phi$ information and in addition the middle three layers give z information by the time difference between signals at either end of the planks. The resolution per point is 110 μm in $r\phi$, and 4.4 cm in z.

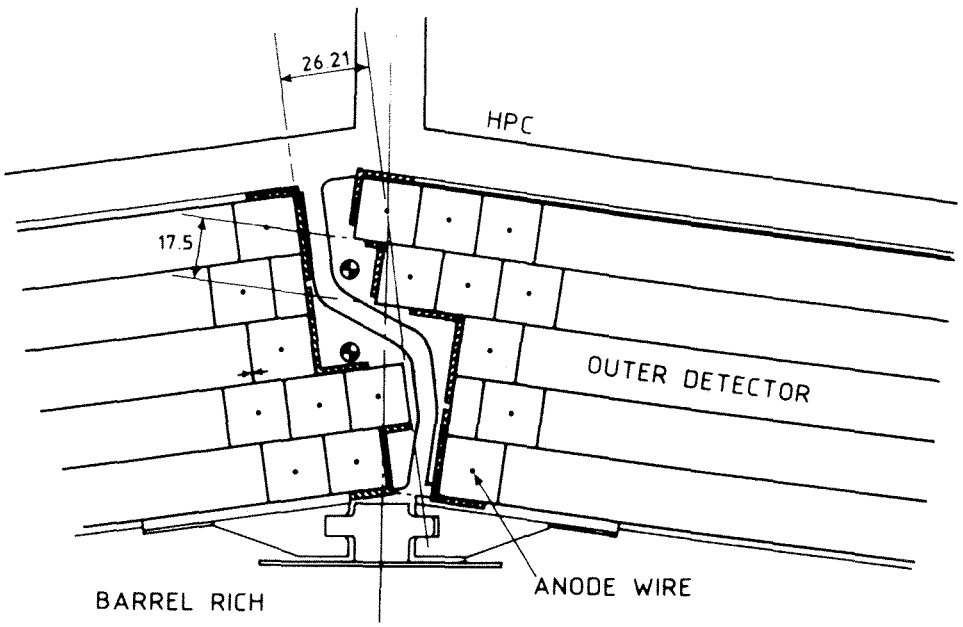

Figure 3.7: *Transverse view of outer detector drift tubes in two neighbouring planks.*

3.2.3 Calorimetry

The High Density Projection Chamber

The High Density Projection Chamber (HPC) [4, 40] is a gas sampling electromagnetic calorimeter capable of high granularity three-dimensional reconstruction of particle showers as well as sensitivity to minimum ionising particles. It lies between a radius of 2.08 m and 2.55 m and covers polar angles from 43° to 137°. It consists of 24 sections

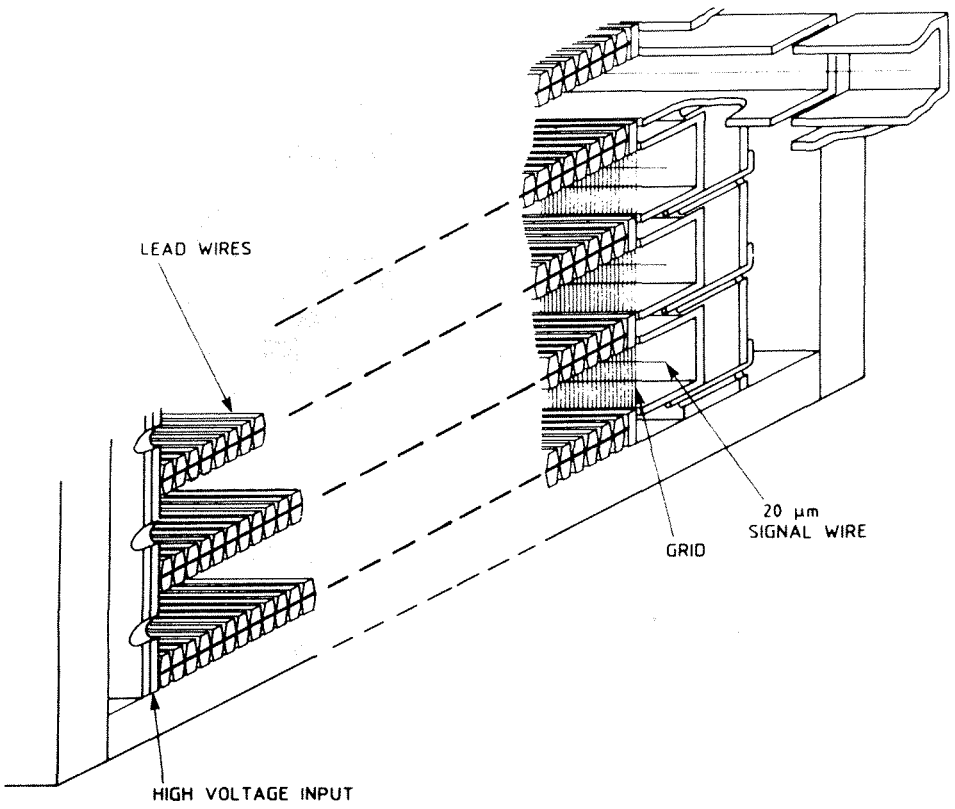

Figure 3.8: *View of lead wires in an HPC module.*

in ϕ, each section containing 6 trapezoidal modules along z of 85 cm length each. The material of the converter is formed by rows of pairs of trapezoidal lead wires of height 1.7 mm and spacing 0.2 mm glued back-to-back onto a fibreglass-epoxy support (see Figure 3.8). At the edges of the module, the wires are bent back to form an overall 41 layer accordion-like structure with 8 mm gaps between the layers of wires for the gas. The gas is an 80-20 % mixture of argon and methane at 1 atmosphere pressure.

The lead wires double as the electric field cage. Electrons produced in the lead cause secondary ionisation in the gas, which drifts along z to readout planes at the end of the module consisting of rows of cathode pads. The pad layout is shown in Figure 3.9 and provides granularity of 1° in ϕ and nine layers of radial sampling. The first three layers have a depth of 1.4 X_0 each, the next three 1.9 X_0 each and the last three 2.8 X_0 each (see Figure 3.9). A scintillator layer is inserted after the first three layers for fast triggering purposes.

The z position of showers is reconstructed from the drift time information. The angular resolutions are $\sigma_\phi = 3.8$ mrad and $\sigma_\theta = 2.6$ mrad (or 5.5 mm in z) [41]. Two showers

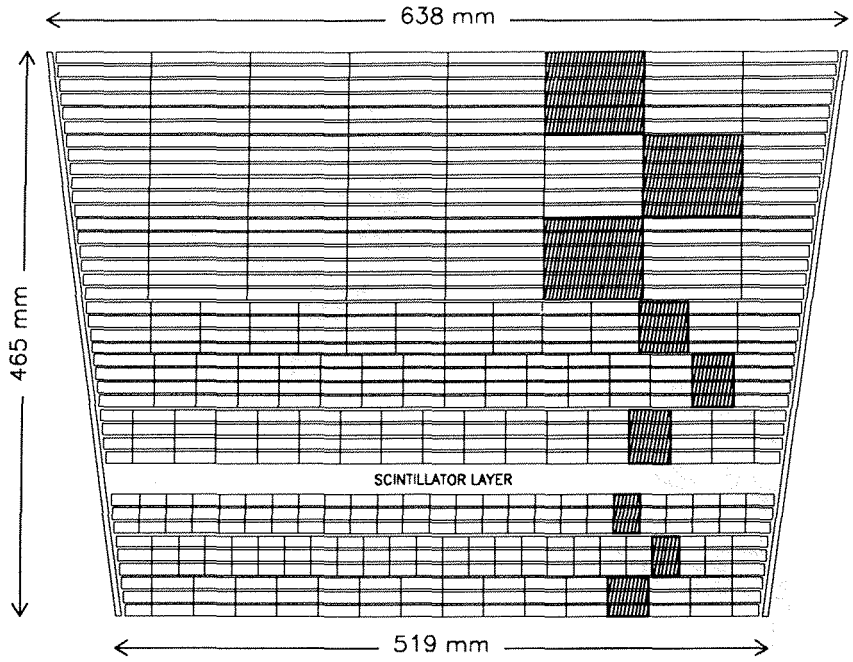

Figure 3.9: *Pad layout at the end of an HPC module. The pad units in each radial layer are shaded.*

can be separated if they are around 2^o apart. The energy resolution is given by [42]

$$\frac{\sigma(E)}{E} = \frac{29}{\sqrt{E}} \oplus 7\% \tag{3.3}$$

and is around 8 % for Bhabhas on the peak.

The Hadron calorimeter

The Hadron calorimeter (HCAL) [4] is a gas sampling calorimeter placed after the magnet between a radius of 318.5 cm and 477.5 cm and covering polar angles from 11^o to 169^o. There is a gap for cables in the 40^o region between the barrel and endcap sections. The barrel section consists of 24 trapezoidal modules in ϕ, displaced by 7.5^o with respect to the HPC modules to avoid coincidence of ϕ gaps in the two calorimeters. Each module has 20 layers of 5 cm thick iron plates with 2 cm gaps in between into which are inserted planes of limited streamer mode detetctors. A detector consists of 8 streamer tubes, each with a central anode wire surrounded by a graphite-coated cathode cell of dimensions 9 x 9 mm^2 (see Figure 3.10). There is a gap at 90^o between the streamer tubes. The inner layer of the barrel muon detector (see Section 3.2.4) is inserted into a 9 cm gap between the 18th and 19th layers. The endcap sections consist

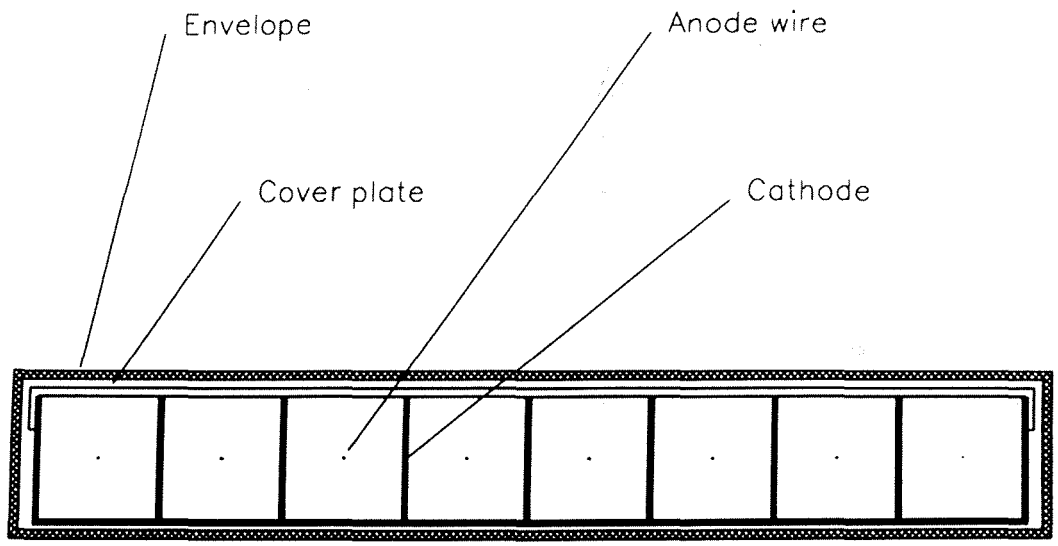

Figure 3.10: *A limited streamer mode detector in the HCAL.*

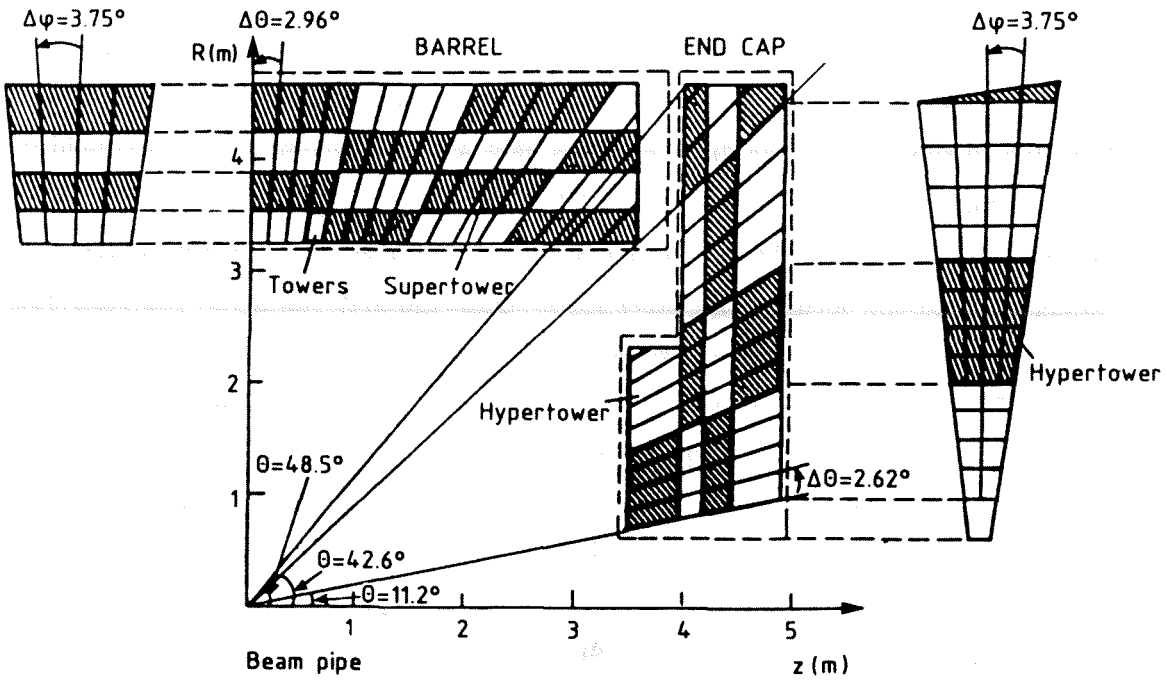

Figure 3.11: *HCAL tower, supertower and hypertower structure.*

of 19 layers of plates. The iron plates also serve as the return yoke of the magnetic field. The calorimeter is six interaction lengths deep at $\theta = 90^o$.

The streamer charges produced are grouped for readout purposes into *towers*. A tower covers a volume of equal angular dimensions pointing back to the origin. In the barrel section, the signals from 5 layers of detectors are grouped together for one tower, giving an overall readout of 4 radial layers. In the endcap, 4 or 7 layers radially form a tower. The angular dimension of a tower is $\Delta\phi = 3.75^o$ and $\Delta\theta = 2.96^o$ (2.62^o) in the barrel (endcap). For trigger purposes, 4 x 4 adjacent towers in $z\phi$ form a *supertower* and 4 radially stacked supertowers form a *hypertower* [43] (see Figure 3.11).

Calibration of the HCAL signals is performed using hadrons and dimuons from Z^0 decays. The energy resolution for incident hadrons is given by [4]

$$\frac{\sigma(E)}{E} = \frac{120}{\sqrt{E}}\% \tag{3.4}$$

3.2.4 Muon chambers

Barrel muon detector

The barrel muon detector (MUB) [4, 44] consists of 7 layers of staggered proportional wire drift chambers covering polar angles from 51^o to 129^o (full efficiency from 55^o to 125^o due to geometry). The drift chambers have a central anode wire in a cuboid of typical length 365 cm and cross section 2.0 x 20.8 cm^2. In each z half, there are 24 modules in ϕ. The first three drift chamber layers are placed within the HCAL at a radius of 445.5 cm, forming the *inner layer*. Only the first two layers are read out, the third set of chambers being used as spares. The next two layers of chambers are outside the iron of the HCAL at an average radius of 479.3 cm and form the *outer layer*, consisting of 12 modules in ϕ. The last two layers are at an average radius of 532.0 cm (radius varies due to support legs, cabling, cryogenic ducts and so on) forming the *peripheral layer*. The 12 modules of the peripheral layer cover alternate regions of ϕ to the modules of the outer layer (see Figure 3.12). Thus it is possible for a particle to have up to six hits when passing through an overlap region. A delay line in each chamber provides z measurements.

The resolutions obtained are $\sigma_{r\phi} = 4$ mm, and $\sigma_z = 2.5$ cm. The efficiency for detecting a muon within the angular coverage of the MUB is around 98 %.

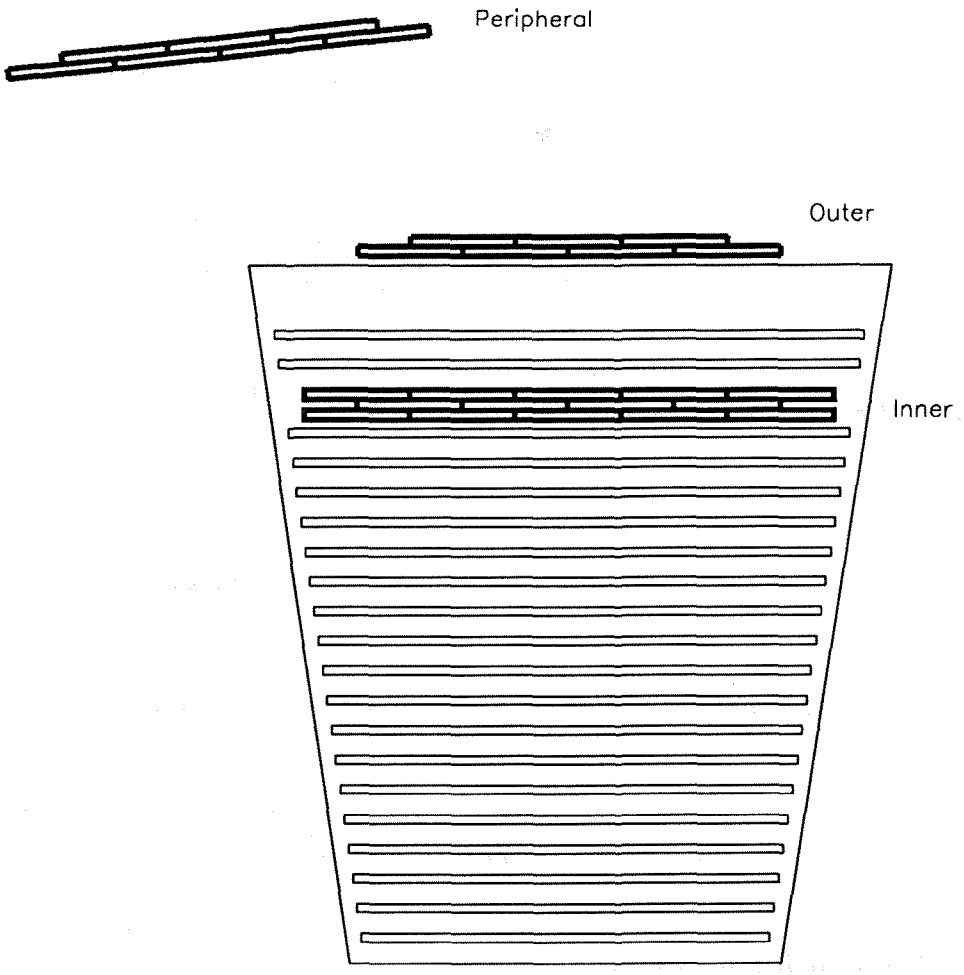

Figure 3.12: *The layout in ϕ of the barrel muon chambers. The inner layer lies within a module of the barrel HCAL.*

Forward muon detector

The forward muon detector (MUF) [4, 45] provides coverage from around 53^o down to 11^o and from 127^o to 169^o. However, due to geometry, this coverage is ϕ-dependent and rather limited until fully into the forward region. Each endcap detector consists of 2 planes of 4 quadrants of dimensions 4.4 x 4.4 m^2. The first plane is at a z of $\pm$ 464 cm and lies within the endcap section of the HCAL. The second plane is at a z of $\pm$ 501 cm. Each quadrant has two orthogonal layers with 22 limited streamer mode drift chambers per layer. A cross section through a drift chamber is shown in Figure 3.13.

The x and y coordinates are measured from the drift time to the anode and the difference betwen the two times measured at the ends of a delay line, using the delay line

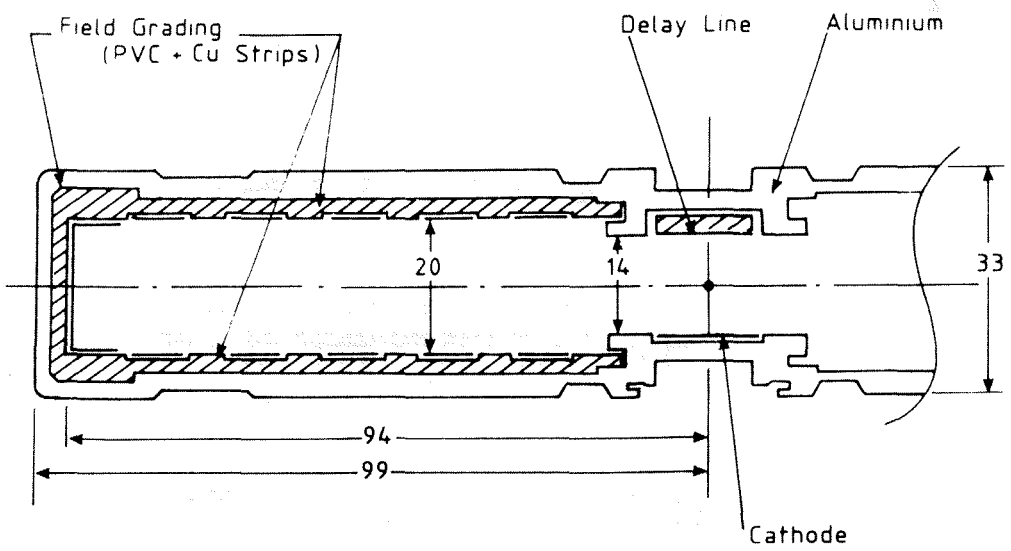

Figure 3.13: *Cross section through a MUF drift chamber.*

information of the crossed layer to resolve left-right ambiguities arising from the drift part. The resolution in x and y from the drift time measurement is 1 mm.

3.2.5 Time of flight detector

The time of flight detector (TOF) [4] is mainly used as a fast trigger in the barrel, covering polar angles from 41° to 139°. It is mounted just outside the solenoid and consists of a layer of scintillator counters, 86 in each half of z with dimensions 355 x 19 x 2 cm^3, with dead zones at 90° in θ and at the support legs of the cryostat. Time resolution is around 3 ns, and the efficiency to detect a minimum ionising particle is 85 % [46].

3.2.6 Magnet

The DELPHI magnet [4] is a superconducting solenoid of length 7.4 m at a radius of 2.60 m, just after the HPC. The superconducting cable is made from 17 twisted wires containing Nb-Ti filaments embedded in a copper matrix. The cable is wound onto an Al support cylinder which is cooled externally by liquid He at 4.5 K. The field of 1.2 T is provided by a 5000 A current flowing through the cable. Two 35 cm long end sections containing a second layer of cable improve field homogeneity. This is important

for detectors with long drift volumes. The field has been measured to be homogeneous to within 10 G inside the TPC.

3.2.7 Luminosity detectors and measurement

Small angle tagger

The small angle tagger (SAT) [47] consists of two arms in $+z$ and $-z$, each with a tracker followed by a calorimeter. It covers polar angles from 43 to 135 mrad. The tracker at present is only partially commissioned, with 2 out of the 3 foreseen planes of silicon detectors installed in one arm only. The readout segmentation has a radial pitch of 1 mm and and an angular pitch in ϕ of 5^o. Some data were recorded using the tracker in 1991, providing a valuable cross check of the impact point reconstructed in the calorimeter section [11].

The calorimeter consists of alternating layers of lead sheets and scintillating fibres mounted on an aluminium support in the form of half-cylinders. The total thickness is 28 X_o. To define the acceptance of the calorimeter, a 12 X_o thick lead mask is installed in front of the calorimeter in the arm without the tracker. The lead mask covers the inner 3 cm of the calorimeter and defines the acceptance with a precision of better than 100 μm. The region of $\phi \pm 15^o$ from the vertical which includes the dead zone between the half-cylinders was also excluded by a lead mask. The readout segmentation of the calorimeter in $r\phi$ is shown in Figure 3.14. The energy resolution is 4.4% for the arm in $+z$, and 4.8% for the arm in $-z$ for Bhabhas at 45 GeV.

The Very Small Angle Tagger

The Very Small Angle Tagger (VSAT) [4] is situated at $z = \pm$ 7.7 m, just before the superconducting quadrupoles, and covers polar angles from 5 to 7 mrad. The detector consists of two rectangular stacks per arm, each 5 cm high, 3 cm wide and 10 cm long, and covering angles in ϕ of $\pm$ 45^o from the horizontal. Each stack has 12 layers of tungsten plates interleaved with silicon detectors, giving a total depth of 24 X_o. The energy resolution obtained for Bhabhas is 5 % at 45 GeV.

Measurement of luminosity

The integrated luminosity as mentioned in Section 3.1 must be known in order to obtain any cross sections. Therefore, to measure it, we *choose* a theoretically well-understood

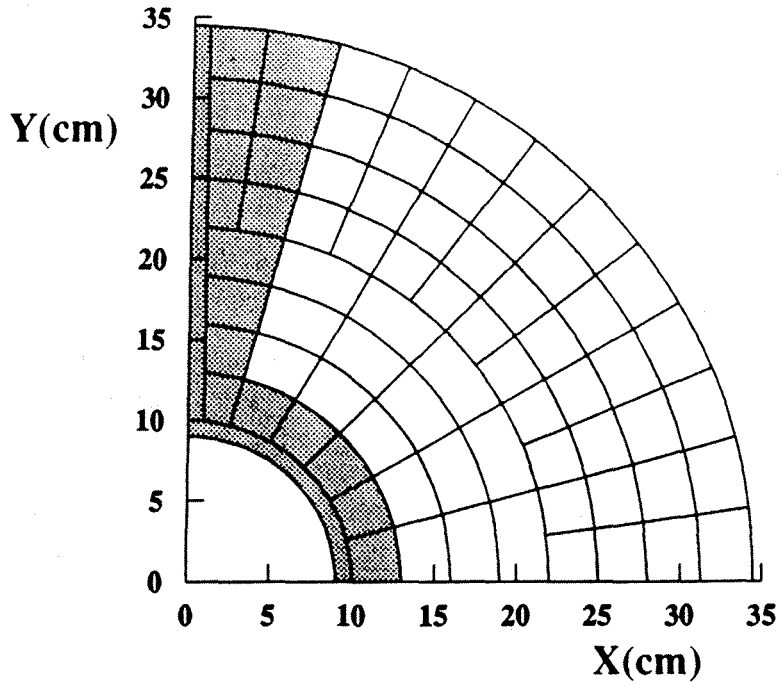

Figure 3.14: *Readout segmentation in $r\phi$ of the SAT showing position of the lead mask (shaded).*

cross section and use the number of events seen by that process to measure $\int L\mathrm{d}t$. Bhabha scattering at small θ angles is especially suitable, as the γ t-channel scattering, which is a QED process, dominates [48] :

$$\frac{d\sigma}{d(\cos\theta)} \propto \frac{1}{\theta^4} \quad (\theta \ll 1 \text{ rad}) \tag{3.5}$$

The absolute luminosity is measured with the SAT with a total systematic uncertainty of 0.6 % [11]. The statistical error on the luminosity is reduced on the off-peak energy points by normalising the data from the VSAT (which has higher statistics, but also higher absolute systematic errors) in terms of the SAT luminosity on the peak [49].

3.3 The Data Acquisition System

The DELPHI Data Acquisition System and control (DAS) [50] consists of a set of *partitions*, each one more or less corresponding to a subdetector. This provides each detector with the ability to perform tests and calibrations in standalone mode. Each partition consists of:

- The Fastbus readout system

- The Slow Control system which monitors and controls aspects such as the gas, volts and temperature.
- Organisation of the data flow in the online computers.
- Overall partition control

Two of the partitions are for the trigger and the central readout.

3.3.1 The Trigger System

With a luminosity of $\approx 5 \times 10^{30}$ cm^{-2}s^{-1} and a cross section for e^+e^- annihilation via γ, Z^0 production of 34 nb on the Z^0 peak [52] the expected event rate for standard physics is ≈ 0.17 Hz. Other contributions to the event rate come from t-channel Bhabhas (used to measure the luminosity) and two-photon interactions. However, there is potentially a large rate of not so interesting events – cosmics, beam-gas and beam-wall interactions, synchroton radiation, off-momentum beam particles and noise in general which can burden the data acquisition system. An ideal trigger system is designed to meet several requirements:

- High trigger efficiencies for all standard channels.
- High degree of redundancy such that each channel can be triggered by two or more independent triggers, in order that the efficiencies may be calculated from data.
- A loose enough trigger to accept almost all interesting events as well as a level of uninteresting events that still maintains a low percentage of dead time.[1] This requirement is generally achieved by requiring a trigger to be based on a combination of signals from more than one detector, thus reducing the susceptibility to detector noise.
- Possibility to trigger on non-standard channels (e.g. the Higgs boson, other new particles).

The DELPHI trigger [53] has been designed to have four successive levels, each performing a more refined selection of events. The first level decision, T1, relies on information

[1]The percentage dead time can be thought of as the total fraction of bunch crossings happening while the detector is responding to a possible event.

from detectors with short drift times and is taken ≈ 4 μs after the beam crossover signal (BCO). If this is negative (T1_NO), the detectors halt data acquisition and their front end electronics are reset in preparation for the next BCO. If it is positive (T1_YES), a more sophisticated processing of the data for the second level trigger T2 takes place with additional information becoming available from detectors with longer drift times. The T2 decision is made ≈ 44 μs after the BCO. If the decision is positive (T2_YES), the data in the front end electronics is read into local buffers in a time of ≈ 4 ms. The third (T3) and fourth (T4) level triggers are software triggers. T3 runs on the data in the buffers to further select events to be transferred to a single global event buffer. T4 then performs a tagging of the event type before the data are written onto tape. Up to 1991, T3 and T4 were not yet implemented.

The average rate for the first level trigger was around 500 Hz, and 4 Hz for the second level [54]. This corresponded to a minimum dead time of around 3 % [51].

The trigger hardware

The trigger hardware consists of *central* modules and *local* modules for each partition (see Figure 3.15).

CENTRAL

- The Trigger Supervisor Decision Box or PYTHIA. This receives trigger signals via the Trigger Data Lines (TDLs) from the detector partitions and makes T1 and T2 decisions based on programmable look-up tables. The signals are monitored via a set of scalers.
- The Trigger Supervisor Control Box or ZEUS. This distributes timing signals to the detector partitions. It also receives the trigger decisions from PYTHIA and transmits them to the partitions.

LOCAL

- The Local Trigger Supervisor Decision Box or LTS_DB. This prepares trigger signals for the partition (in some cases there is also a Subtrigger Decision Box) which are sent on the TDLs to PYTHIA.
- The Local Trigger Supervisor Control Box or PANDORA. This communicates with the LTS_DB, receives the timing signals from ZEUS and controls the timing of the front end electronics.

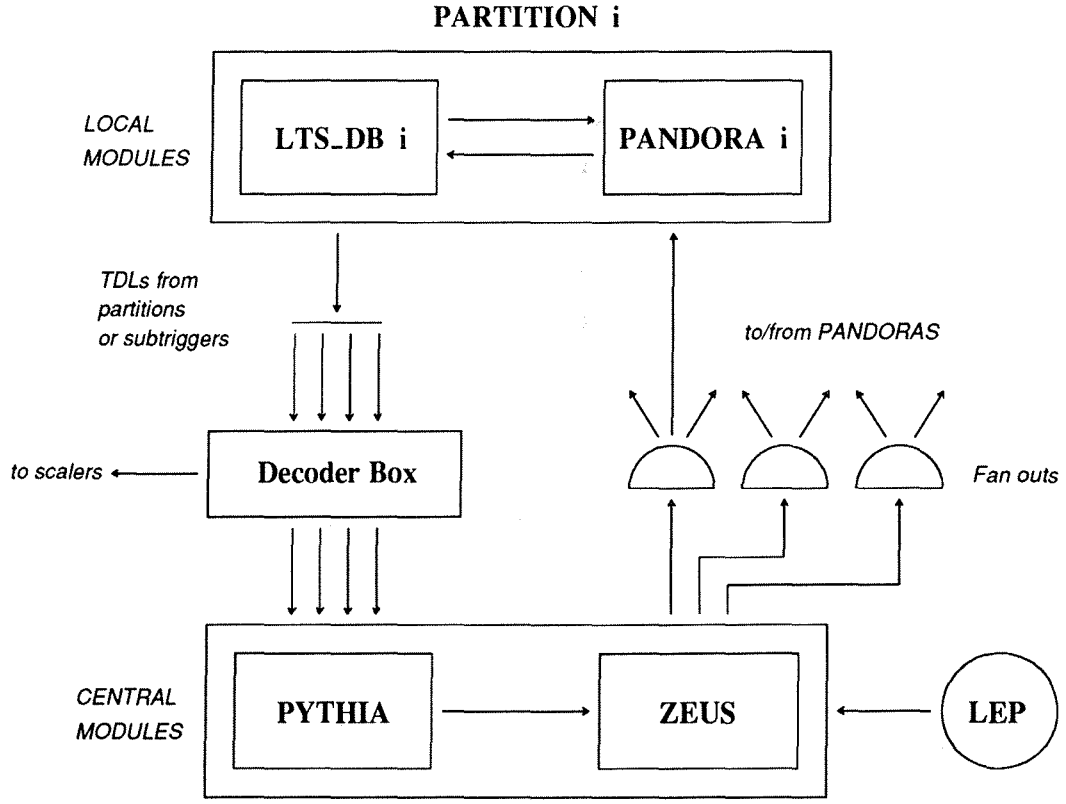

Figure 3.15: *The central and local (shown here for a partition* i*) trigger modules.*

PYTHIA trigger signals

The PYTHIA module receives signals from several subtriggers. Information on the multiplicity (0, 1, 2 or > 2) of tracks and energy depositions found can be sent using pairs of coded TDLs. The decision at each level is the *OR* of 16 Decision Functions corresponding to the loaded look-up tables.

Track trigger

The detectors contributing signals are the TPC, the forward tracking chambers FCA/B, ID/OD, and the TOF. The signals are generally based on simple track finding algorithms for either single tracks or multiple tracks which may or may not be geometrically correlated. In the barrel region, the TPC contributes at the 2nd level only. The signals from the ID and OD may be combined as they share the same LTS_DB.

Muon trigger

This is based on hits in quadrants or octants of the MUB and MUF. The MUF con-

tributes to the 2nd level only because of its long drift times.

Electromagnetic trigger

The 1st level HPC trigger is based on hits in the scintillator layer with an energy deposition threshold of 2 GeV in each ϕ sector. The 2nd level HPC trigger is not yet operational. The forward electromagnetic calorimeter (FEMC) signals are the same for the 1st and 2nd levels and has high (2.5 GeV) and low (1.2 GeV forward endcap, 1.5 GeV backward endcap) thresholds.

Hadron trigger

There are three thresholds for energy deposition – muon (0.5 GeV), low (2 GeV) and high (5-7 GeV). The signals are the same for both 1st and 2nd levels.

Bhabha trigger

The SAT 1st level has low (11 GeV) and high (30 GeV) thresholds, with various single and coincident signals. The VSAT requires coincidences for energies above 25 GeV. Due to the large number of Bhabhas in the VSAT, up to 12 events can be stored locally, and when the buffers become full, a forced T2_YES is sent to PYTHIA.

B1 trigger

This simplified trigger system has been operational since data taking first began. Signals from the ID, OD, HPC, TOF, FCA/B, FEMC and forward scintillator counters (HOF) are combined using NIM electronics instead of Fastbus as for the standard PYTHIA signals. The final B1 signal is an *OR* of several components and is sent at 1st level via a TDL to PYTHIA. Some of the components are also sent separately at 1st and 2nd level.

The average trigger efficiency for $e^+e^- \rightarrow \tau^+\tau^-$ events has been estimated from data to be 99.9 $\pm$ 0.1 % for the 1991 data taking period [55].

3.4 Offline data processing

The data written onto tape by the data acquisition system for events selected by the 2nd level trigger is ZEBRA-structured *raw data.* The raw data basically consists of uncalibrated signals such as ADC counts or time slot number.

3.4.1 DELSIM

The DELPHI simulation program is called DELSIM [56]. It has its own generators for various e^+e^- processes, or can be interfaced to external generators. Tracking of the generated particles and their secondary interactions with the material in DELPHI is performed. Detector simulation routines give the corresponding detector responses in terms of electronics signals. The output is raw data in the same format as that produced by real data.

3.4.2 DELANA

The DELPHI event reconstruction program is called DELANA [57]. This performs the decoding of the raw data, pattern recognition, track reconstruction and event tagging. In addition to general routines in DELANA, each detector provides routines for the processing of its recorded data. The data is stored in a well-defined, detector-independent, hierachial structure using the TANAGRA package [58].

The first stage pattern recognition involves a calibration and preprocessing of the raw data by individual detectors to produce Detector Data (TDs). The TDs may be wire hits or space points/cells, and the data banks contain information on their coordinates and the deposited energy (where applicable). The TDs are the input to the local pattern recognition which attempts to reconstruct from them track elements (TEs) to be used as input to the track search. The TEs in the calorimeters are clusters of TDs assumed to originate from a single particle.

The next stage involves a charged track search, grouping together TEs to form track strings (TSs) with ambiguities allowed. The full track fit then follows, resolving ambiguities and providing the track fit parameters for each track (TK) found. The TKs are extrapolated through DELPHI to provide impact points at each detector surface. This allows tracking chambers to further associate any TEs to the extrapolated track, and the track can be refitted and re-extrapolated. The calorimeters are then able to perform associations of TEs (and thus energy deposits) to the extrapolated tracks.

The next step is to collect mass identification information from detectors able to provide it. A global processing gives a final mass assignment to each track.

The final stage involves a search for primary and secondary vertices. Groups of tracks possibly originating from the same vertex are stored as a track bundle (TB). Then a

global vertex fit solving ambiguities and giving the vertex position and track parameters at the vertex is performed to give the track vertex data (TVs).

The TANAGRA data is rather voluminous. Hence, the final data output of DELANA is generally in the form of Data Summary Tapes (DSTs) created by the package PXDST containing information on TEs, TKs, associations, fit parameters and so on [59]. In principle, all the information required to perform subsequent physics analyses should be contained on the DSTs. For special data sets tagged within DELANA (the Leptonics and Selected Two Prongs) master DSTs are also output which contain the raw data, TANAGRA data and the DST data. The data flow from the primordial interactions to the production of DSTs is illustrated in Figure 3.16.

In this analysis, the DELANA_E processing of 1991 data was used for both real data and simulation.

3.4.3 Event viewing

A useful tool in analysis is the ability to visually examine events. The DELPHI Graphics program DELGRA [60] uses the TANAGRA data of the event, and any or all of the banks can be displayed in a 3-D reconstruction of the event. Individual parts of the detector may be zoomed for closer inspection, and the event may be rotated. An example of a $e^+e^- \rightarrow q\bar{q}$ event as seen with the graphics package is shown in Figure 3.17.

3.4.4 Monte Carlo description

KORALZ [62] is a general $e^+e^- \rightarrow f\bar{f}$ generator through both γ and Z^o channels. It is used in this analysis for the generation of $e^+e^- \rightarrow \tau^+\tau^-$ events at the Z^o peak. The main effects taken into account include:

- Multiple photon initial state bremsstrahlung and single photon final bremsstrahlung (per fermion)
- $O(\alpha)$ electroweak corrections
- Longitudinal spin polarisation for initial $e^{\pm}$ and final $\tau^{\pm}$
- Spin polarisation effects in most tau decay processes (except for non-resonant multi-pion decay modes)
- Single photon bremsstrahlung for most tau decay modes

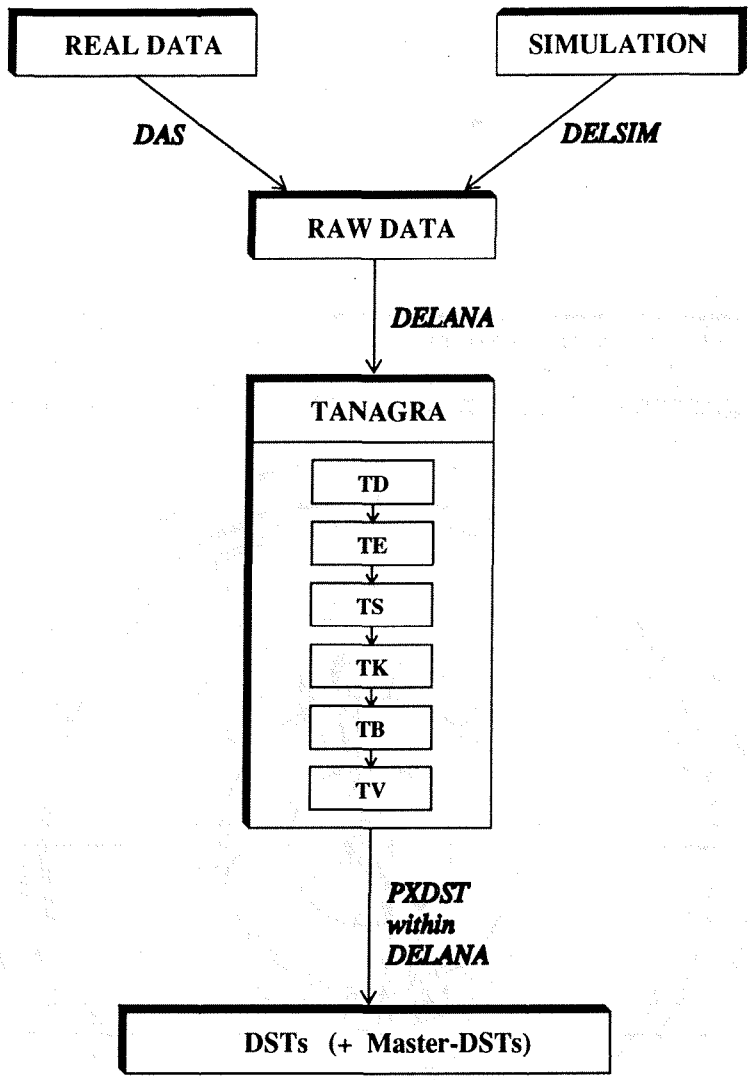

Figure 3.16: *Steps involved in the processing of initial data to produce DSTs.*

KORALZ uses the library TAUOLA [63] in order to simulate the decays of the tau. The decay modes $\tau^- \to e^-\bar{\nu}_e\nu_\tau$, $\tau^- \to \mu^-\bar{\nu}_\mu\nu_\tau$, $\tau^- \to \pi^-\nu_\tau$, $\tau^- \to \rho^-\nu_\tau$, $\tau^- \to a_1\nu_\tau$, $\tau^- \to K^-\nu_\tau$, $\tau^- \to K^{*-}\nu_\tau$, $\tau^- \to 4\pi^{\pm,0}\nu_\tau$, $\tau^- \to 5\pi^{\pm,0}\nu_\tau$, and $\tau^- \to 6\pi^{\pm,0}\nu_\tau$ are included.

Monte Carlo $e^+e^- \to \tau^+\tau^-$ events produced with KORALZ are interfaced with DELSIM to produce a fully simulated sample. Other event generators used to simulate e^+e^- processes at the Z^o peak include BABAMC [64] for $e^+e^- \to e^+e^-$ events, DYMU3 [65] for $e^+e^- \to \mu^+\mu^-$ events, and LUND [66] for $e^+e^- \to q\bar{q}$ events. The generator used for two-photon events is briefly described in Section 4.4.1.

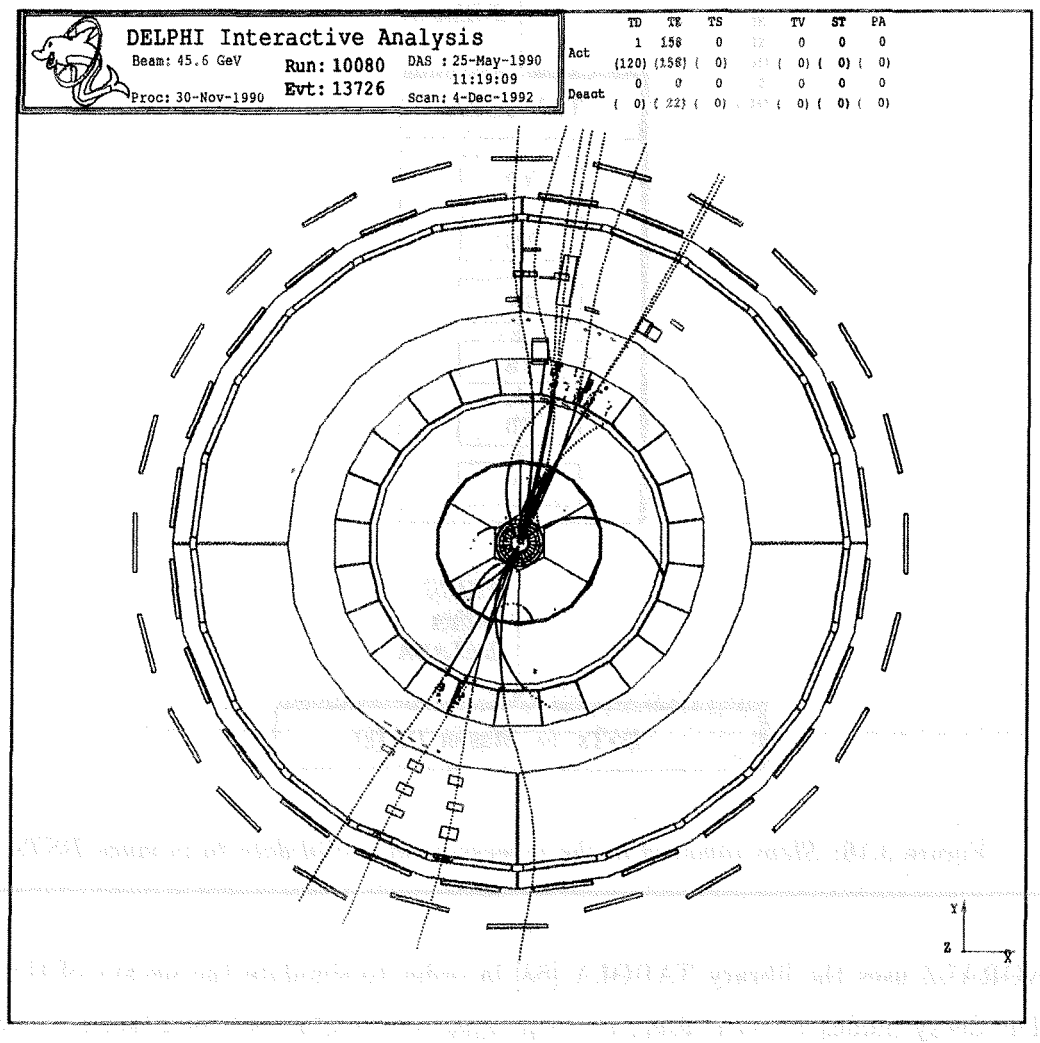

Figure 3.17: $e^+e^- \rightarrow q\bar{q}$ *event as viewed with the DELPHI Graphics program* [61].

3.5 The program PJTAG

The main analysis tool used in the framework of the DELPHI tau physics analysis group (Team 3) is the PJTAG program [67]. The program runs on DSTs and produces variables globally for the event, and for the charged tracks and neutrals (up to a maximum number for reasons of space) in the form of *ntuples*, which can then be accessed by subsequent analysis programs. These ntuples are produced in exactly the same way for data and simulation, and for simulated $e^+e^- \rightarrow \tau^+\tau^-$ events, there is additional information on the particle types generated. The user can define via control cards some event preselection criteria. The relevant variables contained in the ntuples for this analysis are described in Section 4.1.

Chapter 4

Selection of $e^+e^- \rightarrow \tau^+\tau^-$ events

The decay of the Z^o at LEP into $\tau^+\tau^-$ pairs has certain distinctive features which enable it to be well separated from its decays into e^+e^-, $\mu^+\mu^-$ and $q\bar{q}$ pairs. The presence of at least two neutrinos in each event which are undetectable means that the observed energy of the event can be substantially less than the Z^o mass. In $e^+e^- \rightarrow e^+e^-$ and $e^+e^- \rightarrow \mu^+\mu^-$ events however, no other particles are produced unless photons are radiated and thus generally the observed total energy of the event is close to the Z^o mass. $e^+e^- \rightarrow e^+e^-$ events have a signature of two beam momentum tracks depositing most of their energy as showers in the electromagnetic calorimeters. $e^+e^- \rightarrow \mu^+\mu^-$ events have a signature also of two beam momentum tracks which penetrate through the detector to the muon chambers. $e^+e^- \rightarrow \tau^+\tau^-$ events in contrast contain a mixture of hadrons and leptons. decay of the first tau versus a rho decay of the second. The decay of the tau into mostly 1 or 3 charged particles and neutrals also allows for an easy separation from hadronic decays of the Z^o which typically produce many charged particles.

A common selection for taus has been developed to enable a wide study encompassing the $e^+e^- \rightarrow \tau^+\tau^-$ cross section, forward-backward charge asymmetry, the lifetime of the tau, topological and exclusive branching ratios to be performed [5]. This selection is described below, and efficiencies and backgrounds discussed. The main feature of the selection is that it keeps the need to identify particles to a minimum, thus avoiding what could be a large systematic uncertainty due to the use of many detectors. In fact, the only detectors used are the tracking detectors of which the TPC is the main

detector, and the HPC. Apart from using the Outer Detector to aid in the elimination of cosmics, and the separate evaluation of the Monte Carlo efficiencies and correction factors required, the selection and analysis given is that presented in [5].

For a study of the polarisation of the tau using exclusive channels as polarimeters, cuts which would sharply cut off the momentum spectra of the tau decay products are relaxed in order not to introduce strong biases.

To ensure a good understanding of the detector response, the selection of taus is confined to the barrel region of DELPHI ($43^o < \theta < 137^o$).

In Sections 4.2 to 4.5, the cuts used to select $e^+e^- \rightarrow \tau^+\tau^-$ events are described in the context of the backgrounds they reject.

4.1 Event variables

r and z impact parameters

In order to be able to identify a track as being genuinely from the e^+e^- interaction region of DELPHI, the track is extrapolated back to the origin and two orthogonal impact parameters found. The r impact parameter[1] is defined as the distance of closest approach in the $x-y$ plane measured perpendicularly from the origin to the track (see Figure 4.1). The *perigee* is the point on the track at the end of the perpendicular. The z impact parameter is defined as the distance from the origin along the z axis to the perigee. (It is positive if the perigee is in the positive half of z and negative if in the negative half.) The origin is defined not to be exactly at (0,0,0) but to be the average interaction point or beamspot over the year of data taking. In 1991 this was $(-0.27, 0.05, -0.6)$ in units of cm.

Definition of 'good' tracks and hemispheres

A track as reconstructed by DELANA is considered to be 'good' if it is charged, and comes from a fiducial region around the interaction point. It must satisfy

$$| r | < 5 \text{ cm} \text{ and } | z | < 10 \text{ cm}$$

[1]It is signed geometrically with a plus or minus sign according to whether an observer standing at the perigee facing the direction of the track sees the origin on their right or left.

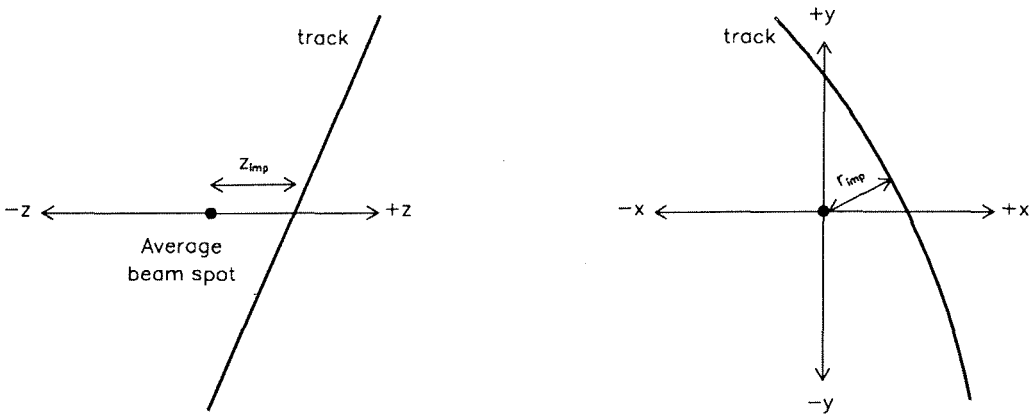

Figure 4.1: *Definition of z and r impact parameters.*

The 'good' tracks (hereafter referred to simply as tracks) in the event are used to calculate the thrust axis[2] of the event. The tracks in the event are divided into **hemisphere 1** or **hemisphere 2** depending on whether the dot product of the track's direction with the direction of the thrust axis is positive or negative.

Isolation angle and acollinearity

By conservation of momentum, in the absence of initial state radiation of a photon by the colliding electron or positron, the primary fermionic decay products of the Z^o should emerge back-to-back. Subsequent weak decays, hadronisation, final state radiation effects and detector effects mean that the number of charged tracks actually seen by the detector and their degree of collimation varies widely. Thus, a useful variable is the isolation angle θ_{iso} which is defined as the *minimum* angle between any pair of tracks in *opposite* hemispheres (see Figure 4.2). It is computed from the measured momenta, θ and ϕ angles of the tracks and is

$$\theta_{iso} \;=\; min_{i,j} \left\{ \cos^{-1} \left(\frac{\boldsymbol{p_i} \cdot \boldsymbol{p_j}}{p_i\, p_j} \right) \right\} \tag{4.1}$$

where the angles are taken between all combinations of tracks i in one hemisphere with the tracks j of the second hemisphere. In the special case of there being only 2 charged tracks in the event, the acollinearity of the event is defined to be

$$\theta_{acol} = 180^o - \theta_{iso} \tag{4.2}$$

[2]If one forms the sum of the components of the track momenta along an arbitrary direction, the thrust axis is defined to be the one which maximises this sum.

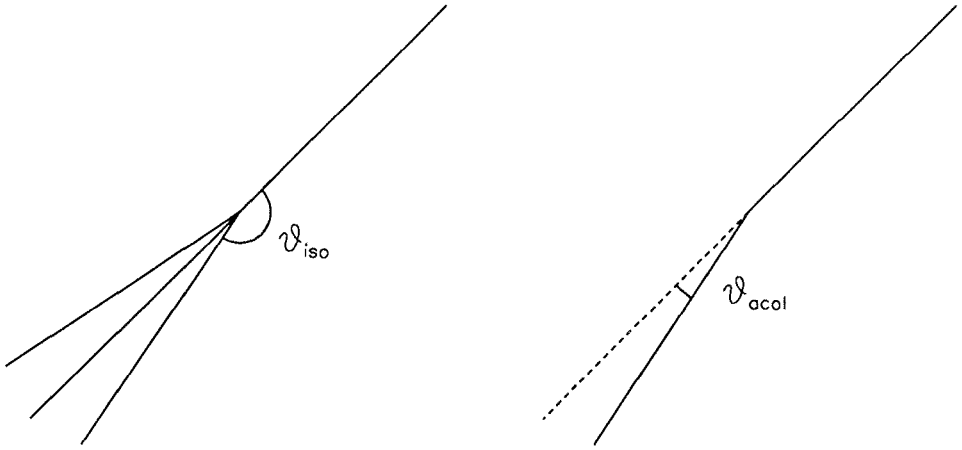

Figure 4.2: *Isolation angle and acollinearity definitions*

Total visible energy

The total visible energy of the event, E_{vis}, is formed by taking the sum of the momenta of all the charged tracks in the event, together with the energy of all HPC showers which have not been associated to a track, assumed to be the electromagnetic energy of the neutral particles in the event.

$$E_{vis} = \Sigma p_{charged} + \Sigma E_{neutrals} \tag{4.3}$$

Total transverse momentum

The total transverse momentum p_T of the event is obtained by combining the vectorial sum of the x components of the track momenta in the event with the vectorial sum of the y components of momenta.

$$p_T = \sqrt{(\Sigma p_x)^2 + (\Sigma p_y)^2} \tag{4.4}$$

Visible momentum

The visible momentum p_{vis} is defined as

$$p_{vis} = \frac{p_1 + p_2}{E_{beam}} \tag{4.5}$$

where p_1 is the momentum of the leading (i.e. highest momentum) track in hemisphere 1 and similarly for p_2.

Radial momentum

This is another way of combining the information on the highest momentum track from each hemisphere into a single variable. It is defined as

$$p_{rad} = \frac{\sqrt{p_1^2 + p_2^2}}{E_{beam}} \tag{4.6}$$

where p_1 and p_2 refer to the momentum of the leading track in hemispheres 1 and 2 respectively.

The variable p_{rad} emphasises the effect of having at least one track with high momentum in the event, at the same time understating the presence of lower momentum tracks (compared to beam energy). This makes it an excellent variable to use in elimination of $e^+e^- \rightarrow e^+e^-$ and $e^+e^- \rightarrow \mu^+\mu^-$ events, where both tracks are usually of high momentum. Even when one of the tracks is of low momentum due to final state radiation or poor momentum measurement, provided that the other hemisphere has momentum close to beam energy, p_{rad} will still be large compared to that for $e^+e^- \rightarrow \tau^+\tau^-$ events.

Radial electromagnetic energy

The variable E_{rad} is defined to be

$$E_{rad} = \frac{\sqrt{(E^1_{CONE})^2 + (E^2_{CONE})^2}}{E_{beam}} \tag{4.7}$$

where E^1_{CONE} and E^2_{CONE} represent the total sum of the HPC energy found in a 30° cone around the leading momentum track in hemispheres 1 and 2 respectively. This variable is used in addition to p_{rad} to eliminate the $e^+e^- \rightarrow e^+e^-$ background to $e^+e^- \rightarrow \tau^+\tau^-$ events.

4.2 Hadronic background

4.2.1 Multiplicity and isolation angle cuts

At LEP, the hadronic decays of the Z^o are characterised by high charged particle multiplicities, with typically around 20 tracks seen per event. The tau can only decay into 1, 3 or 5 charged particles, plus neutrals. Ideally one expects to observe event topologies of the type 1 v 1, 1 v 3, 1 v 5, 3 v 3 and 3 v 5. However, a photon conversion to an e^+e^- pair produces extra charged tracks. Also, the tracks of particles entering

the cracks in the TPC may fail to be reconstructed, or two tracks which are very close together may not be resolved. Thus, one observes events of the type 1 v 2. The migration matrix between the original topology of the event and the observed topology when 2 to 6 tracks are observed is shown in Table 4.1 [38].

Topology	1 v 1	1 v 3	1 v 5	3 v 3
1 v 1	78.26 ± 0.43	1.98 ± 0.25	< 2.8	< 0.5
1 v 2	6.25 ± 0.25	15.09 ± 0.66	< 2.8	1.32 ± 0.64
1 v 3	9.18 ± 0.30	66.36 ± 0.87	13.16 ± 5.76	3.53 ± 1.27
1 v 4	0.79 ± 0.09	4.32 ± 0.37	31.58 ± 7.68	< 0.5
1 v 5	0.50 ± 0.07	2.60 ± 0.29	44.74 ± 8.32	0.44 ± 0.46
2 v 2	0.24 ± 0.05	0.40 ± 0.12	< 2.8	0.88 ± 0.64
2 v 3	0.30 ± 0.06	2.67 ± 0.30	< 2.8	27.44 ± 3.01
3 v 3	0.18 ± 0.04	3.43 ± 0.33	< 2.8	56.64 ± 3.34

Table 4.1: *Percentages of different reconstructed topologies for a generated topology (along top).*

A multiplicity cut is first applied to reject hadronic events (see Figure 4.3). It is required that

- $2 \leq ntrack \leq 6$

The high number of tracks involved also mean that hadronic events produce jets which are not as collimated as in leptonic events. Thus, the hadronic background can be very easily rejected by simply requiring that

- $\theta_{iso} \geq 160^o$

(see Figure 4.4).

4.3 Cosmic background

There is a constant flux of cosmic ray muons resulting from interactions in the earth's atmosphere passing through the DELPHI detector. They fall to a minimum at $\phi = 0^o$ and $\phi = 180^o$ (corresponding to the sides of the detector), and are peaked around $\theta = 90^o$ because of the cut in z defining a good track (see Figure 4.5).

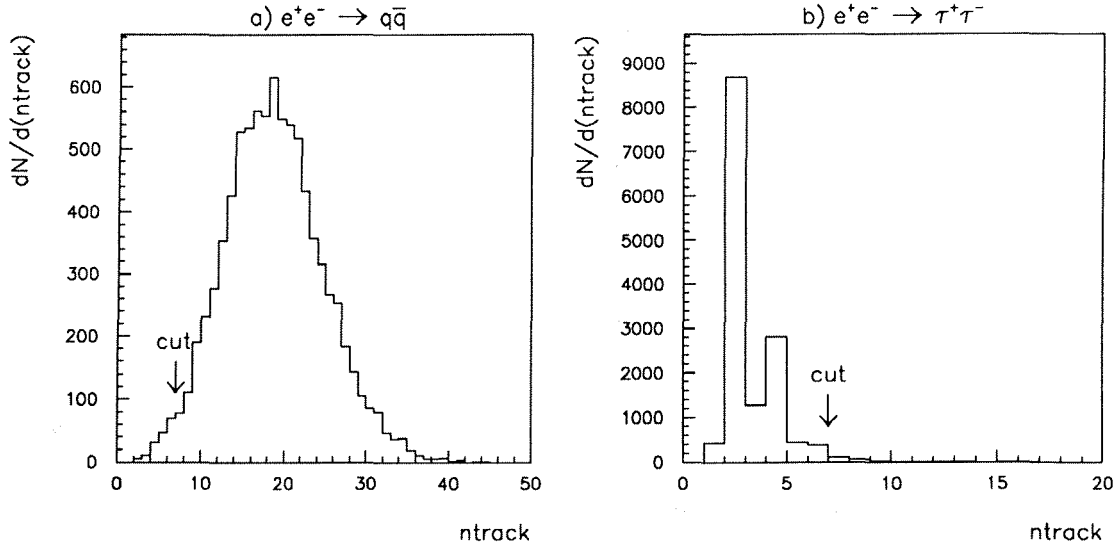

Figure 4.3: *Number of tracks in simulated a) hadronic events and b)* $e^+e^- \to \tau^+\tau^-$ *events.*

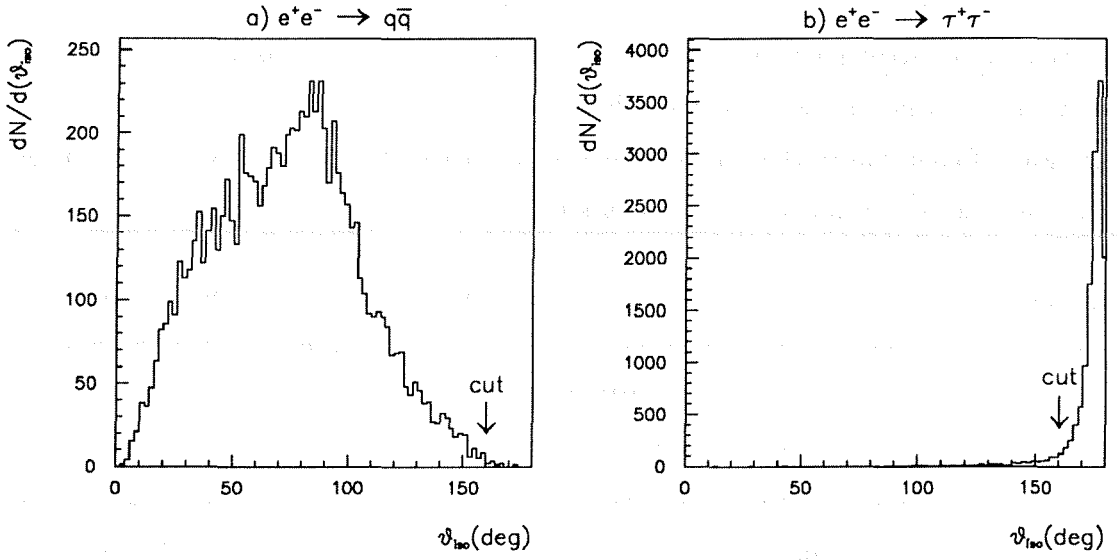

Figure 4.4: *Isolation angle distribution for simulated a) hadronic events and b)* $e^+e^- \to \tau^+\tau^-$ *events.*

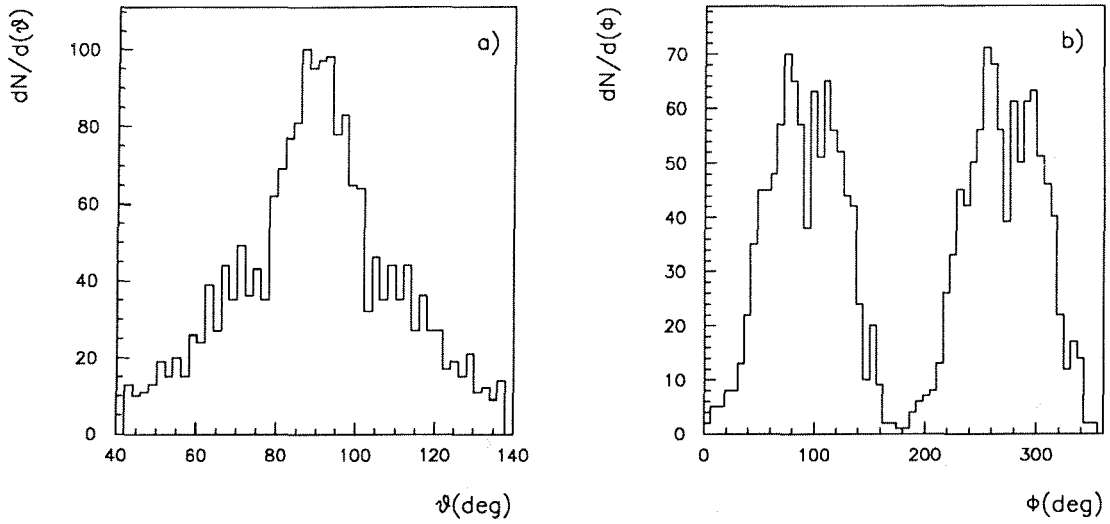

Figure 4.5: *a) θ and b) ϕ distributions for cosmic events. The dips at ϕ = 90° and ϕ = 270° are due to tracking inefficiencies in the TPC.*

Cosmic rays wil be reconstructed as 2 track events if they arrive within the data acquisition periods of the tracking detectors. As a result of this, a lot of cosmic events are seen as tracks in the TPC only, as this detector has the longest drift times of the tracking detectors. Characteristically, cosmics have a flat distribution in time compared to Z^o decays which happen close to the BCO (the beam crossover signal). Thus, if one knows the time of an event relative to the BCO, it could be eliminated as a cosmic. Also, a cosmic event would show a difference between the two times assigned to the ends of the tracks found due to the time required for the particle to traverse the detector, in contrast to an event happening at the origin.

Around the interaction region, cosmics are reconstructed with an almost flat distribution in r and z impact parameters, whereas e^+e^- interactions are reconstructed close to the beamspot near the centre of DELPHI. Thus, the cosmic background can be reduced substantially by applying further cuts in r and z. (These will also reduce beam gas and beam wall interactions to a negligible level.) By selecting events with two tracks outside the vertex region one can obtain a sample of cosmics with which to study distributions and the effects of cuts applied to them. Cosmic rays are an important background for the muon decay channel of the tau as naturally they will be identified as muons. They also have a falling momentum spectrum as do the muons coming from tau decays (see Figure 4.6).

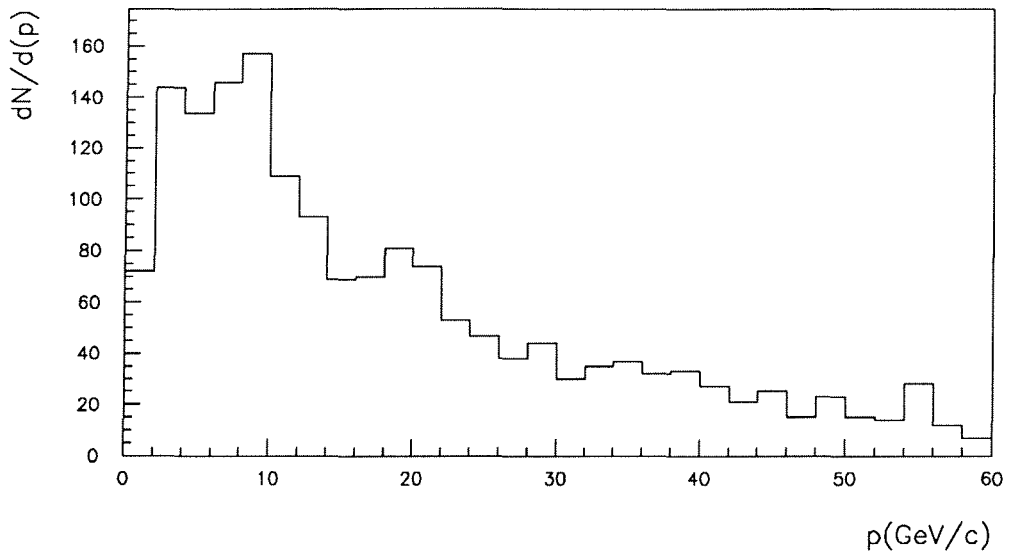

Figure 4.6: *Momentum spectrum of cosmic events (selected outside vertex region in r and z).*

4.3.1 Acollinearity cut

The acollinearity of cosmic ray events is expected to be close to zero, since they consist of a single particle. However, the momentum measurement of the two tracks can be poor because only the TPC contributed to the track fit, leading to a smearing of the acollinearity. An acollinearity cut of

- $\theta_{acol} > 0.5^o$

is applied to events with 2 tracks and eliminates about 70% of cosmic events.

4.3.2 r and z impact parameter cuts

Cuts in r and z impact parameters are uncorrelated within the interaction region, being in perpendicular planes. Previously, in the selection of good tracks, fairly loose cuts were applied. These are now hardened for the leading track in each hemisphere, requiring that

- $| r | < 1.5$ cm
- $| z | < 4.5$ cm

It is clear from the plots (see Figure 4.7) that the cuts could be made a lot narrower without significant loss in efficiency. However, the background due to cosmic rays can

be controlled effectively and to ensure good agreement between real data and simulated data which is too optimistic concerning misreconstructions, the cuts are loosely placed.

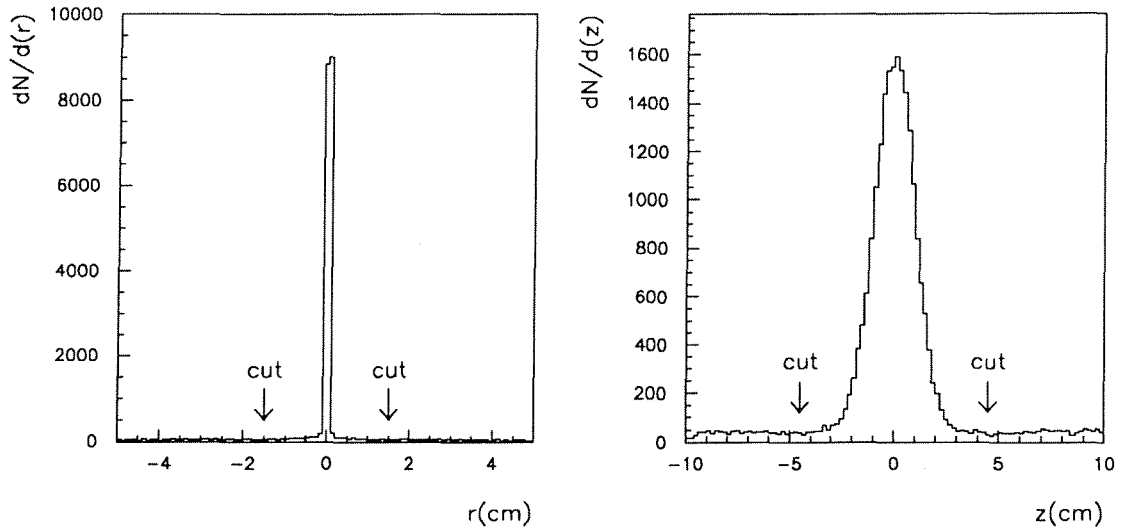

Figure 4.7: *r and z impact parameter distributions in data. The tails are mostly due to cosmics.*

4.3.3 TPC timing/z cut

An indirect way of cutting on the time of an event is to make use of the z information of the TPC. Because the TPC is divided into two halves in $+z$ and $-z$, each with opposite drift directions, a cosmic event which arrives out of time is reconstructed with its two tracks displaced in z. Consider a cosmic arriving t_1 before the BCO. Ionisation drifts in opposite directions in each half of the TPC taking time t_2. When the drift distances are reconstructed, they will be reconstructed relative to the BCO time, thus assuming a drift time of $t_2 - t_1$ and hence the track in each half will be reconstructed displaced from its true position by a distance vt_1 nearer the endplates of the TPC where v is the TPC drift velocity. Thus the two tracks will be displaced in z by $\mid z_1 - z_2 \mid = 2vt_1$ relative to each other. A cosmic event taking place t_1 after BCO time will have two tracks each reconstructed vt_1 closer to the central plane of the TPC, but again the relative displacement will be $2vt_1$. Thus, a cut in $\mid z_1 - z_2 \mid$ where z_1 is the z impact parameter of one track and z_2 the z impact parameter of the second track corresponds directly to a cut in the time of the event relative to BCO. A cut of

- $\mid z_1 - z_2 \mid < 3$ cm

is applied to 1 v 1 topologies which is equivalent to an event arrival time of less than 220 ns relative to the BCO.

4.3.4 The ODTIME program and OD timing cuts

To eliminate remaining cosmics from the tau sample, information from the OD on the time of the event and individual tracks is used. The OD attempts to make a track element for a particle by reconstructing drift circles in the tubes hit from the drift times registered, and fitting a line tangentially to the circles. This fit involves a parameter T_0, which is a constant time for Z^o events. Since cosmic events have a high probability of not arriving near the BCO time, the best track fit to the hits on the OD could be achieved if the T_0 was allowed to vary, and the new T_0 would then be a measure of how out of time the track was with respect to the BCO.

A standalone package called ODTIME [68] has been developed to perform such a re-fitting of the T_0. It performs fits to each track independently in the event and also to both tracks simultaneously. Each track is extrapolated to the OD in order to collect hits belonging only to that track and to obtain a good starting point to the fit. In the combined track fit, the two TPC TEs are forced to be on the same helix for extrapolation to the OD. This has the advantage of not using the OD TEs which have a fixed T_0, and thus not biasing the fitting of the OD track towards an in-time track. On average, there will be 5 data points per track, corresponding to the 5 layers of drift tubes in the OD. A straight line fit to the drift circles is made which is a good approximation for tracks with a transverse momentum of at least 2.5 GeV/c, given that the OD has a resolution of 100 μm per point and a depth of 8 cm. The sizes of the drift circles are changed by adjusting the T_0 until a successful fit is achieved.

Reasons for a failure to fit the track include:

1. Failure to extrapolate the track to the OD due to low momentum of track or a bad extrapolation.

2. Insufficient (< 4) hits on which to perform the fit.

3. No drift times recorded for the hits due perhaps to data acquisition problems or cosmic event happening outside the OD gate of 50 ns before BCO to 650 ns after.

The upper track for a cosmic event has an earlier T_0 than the lower track, indicating

the time of flight for a cosmic event. The expected time difference Δt is given by

$$\Delta t = 2R_{OD}/c \sin\theta \tag{4.8}$$

where R_{OD} is the radius of the OD. For a cosmic event incident at an angle $\theta = 90^o$, the time of flight across the OD which is at a radius of 2 m is about 13 ns (see Figure 4.8). A global χ^2 hypothesis test is performed for successfully fitted track pairs. For the Z^o hypothesis, the time difference between the top and bottom track, Δt = 0 $\pm$ 1 ns. For the cosmic hypothesis, Δt = 2R$_{OD}$/c sinθ $\pm$ 1 ns. A flag of IFLAG = -3 is set if the event is classified as a cosmic.

The approximation of taking the two tracks and forcing them onto the same helix is valid for cosmics which are a unique particle with a unique momentum, and for most $e^+e^- \rightarrow \mu^+\mu^-$ events since each muon is usually close to 45 GeV/c in momentum. However, in the case of taus, the tracks could have rather different momenta, and this can lead to misreconstruction of the times of the tracks such that some $\tau^+\tau^-$ events are flagged as cosmics although overall close in time to the BCO. Therefore, in order to avoid throwing away genuine taus, events are rejected as cosmics if

- IFLAG = -3 , and more than 50 ns from BCO

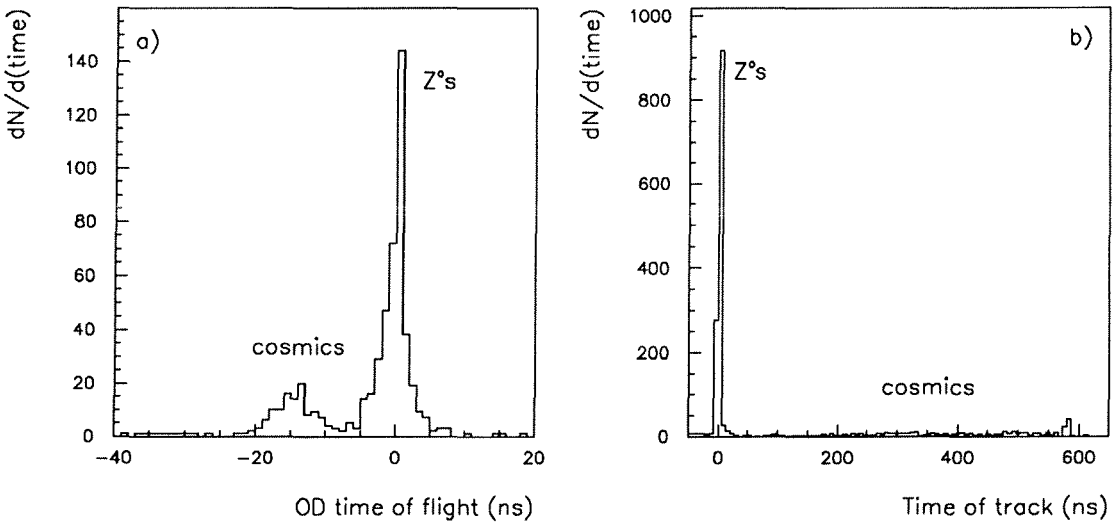

Figure 4.8: *a) The time-of-flight given by the Outer Detector showing a peak due to cosmics around -14 ns, and b) the absolute time of arrival of the track with tails to +650 ns from cosmics.*

4.4 Two-photon background

The colliding e^+ and e^- beams can be considered to be radiating virtual photons which have the possibility to interact via QED processes. A Feynman diagram representing a two-photon process is shown in Figure 4.9.

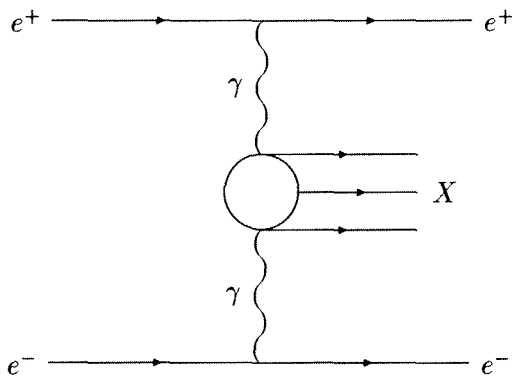

Figure 4.9: *Feynman diagram for* $e^+e^- \rightarrow e^+e^-X$.

The equation for such a reaction is typically represented as

$$e^+ + e^- \rightarrow e^+ + e^- + X$$

The final state of such an interaction consists of the scattered e^+, e^- and X which can for instance be a lepton pair or hadrons. Typically, the e^+ and e^- are lost in the beam pipe, and, within the barrel, only the particles in the X system can be observed. Thus, through the production of these particles, the two-photon mechanism provides an additional background to tau decays. The virtual photons are soft and hence the Q^2 of the interaction is small compared to beam energy, leading to low energy for the state X. Because they are radiated at small angles with continuous energy spectra, the state X is boosted along the beam axis and its transverse momentum is low [69]. In the case of a lepton or quark pair, the fermions are back-to-back in ϕ but emerge at a range of θ angles to each other. Thus, the characteristics of a two-photon event are an isolation angle distribution that is approximately flat, low E_{vis} and low p_T (see Figures 4.11, 4.12, and 4.10).

4.4.1 Monte Carlo description

The event generating programs written by Berends, Daverveldt and Kleiss [70] provide a detailed description of two-photon processes, including radiative corrections. There exists some limited statistics simulated data using this program and passing

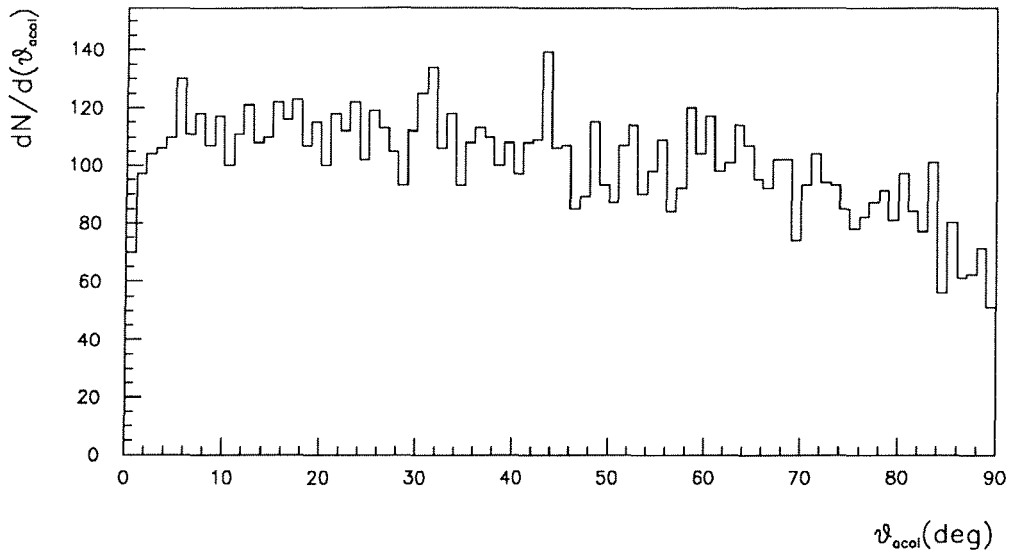

Figure 4.10: *Acollinearity distribution for simulated* $e^+e^- \rightarrow e^+e^-\mu^+\mu^-$ *events.*

the events generated through the DELPHI detector simulation program, DELSIM. The background for the linescan selection of $\tau^+\tau^-$ is estimated using real data (see Section 4.9.4). The Monte Carlo programs are used to find the background to the $\tau^- \rightarrow \mu^-\bar{\nu}_\mu\nu_\tau$ selection of Chapter 5.

4.4.2 E_{vis} and p_T cuts

The following cuts are applied to reject the two-photon background:

- $E_{vis} > 0.175\, E_{beam}$ (8 GeV at $E_{beam} = 45.6$ GeV/c)
- $p_T > 0.4$ GeV/c for 1 v 1 events

In addition, the isolation angle cut at 160° also reduces the background substantially.

4.5 Leptonic background

The remaining background which has to be eliminated comes from the other leptonic decay modes, namely:

$$e^+e^- \rightarrow e^+e^- \text{ and } e^+e^- \rightarrow \mu^+\mu^-$$

In the absence of initial or final state radiation, the reactions $e^+e^- \rightarrow e^+e^-$ and $e^+e^- \rightarrow \mu^+\mu^-$ would produce two perfectly collinear particles each with energy equal to beam energy. In reality, detector effects result in a smearing of the actual angles and momenta

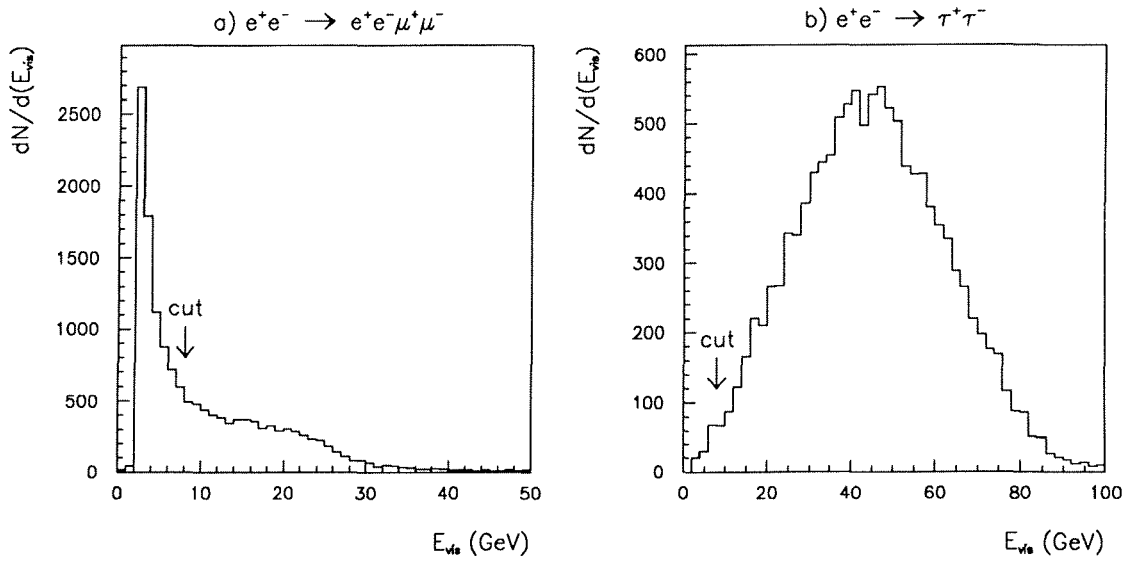

Figure 4.11: *Visible energy E_{vis} in simulated a) $e^+e^- \rightarrow e^+e^-\mu^+\mu^-$ events and b) $e^+e^- \rightarrow \tau^+\tau^-$ events. The cutoff of E_{vis} at 2 GeV for the two-photon events is due to an invariant mass cut applied in the generator.*

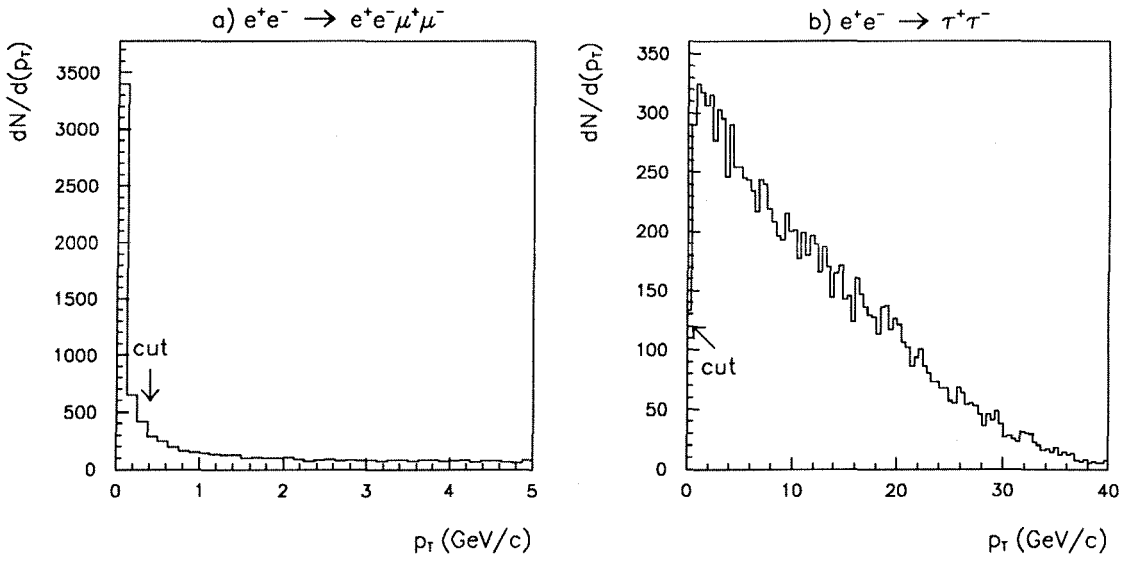

Figure 4.12: *Total transverse momentum p_T in simulated a) $e^+e^- \rightarrow e^+e^-\mu^+\mu^-$ events and b) $e^+e^- \rightarrow \tau^+\tau^-$ events.*

of the tracks, and they are measured to be acollinear. The momentum resolution worsens particularly when the Outer Detector or the Vertex Detector is not used in the track fitting, or when the track passes through a TPC crack. In these cases, the measured momenta can be quite different to the beam energy.

Final state radiation of one or more photons by either or both particles causes the particles to be acollinear (the harder the photon, the more acollinear). The photon may convert into an e^+e^- pair, leading to more than two tracks in the event. The acollinearity cut described above at $\theta_{acol} > 0.5^o$ eliminates around 80 % of $e^+e^- \rightarrow \mu^+\mu^-$ events and 70 % of $e^+e^- \rightarrow e^+e^-$ events, while only losing 1 % of $e^+e^- \rightarrow \tau^+\tau^-$ events (see Figure 4.13).

4.5.1 p_{rad} cut

In $e^+e^- \rightarrow \tau^+\tau^-$ events, the charged tracks have a wide range of momentum, depending on the amount the neutrino(s) in a tau decay carries off. This means that the distribution in p_{rad} is substantially different for taus compared to that of dimuons and Bhabhas (see Figure 4.14). Although, to a great extent, the variables p_{rad} and p_{vis} provide correlated information, the separation between $e^+e^- \rightarrow \tau^+\tau^-$ events and the other two leptonic channels is cleaner using the p_{rad} variable as this takes most advantage of the presence of at least one high momentum track. This can be visualised easily by looking at a scatter plot of p_1 against p_2 of data events (see Figure 4.15). The spread of points at all combinations of p_1 and p_2 are mainly $\tau^+\tau^-$, while the concentration of points around $p_1 \approx p_2 \approx E_{beam}$ represents mainly dimuons and Bhabhas. The tails with one track near E_{beam} represent the radiative tails or poor momentum reconstruction.

In applying a p_{rad} cut, the shape of the cut traces a circular path. With a p_{vis} cut, the cut is a straight line across the axes. In the figure, the circle represents a p_{rad} cut at 1. Line 1 represents a p_{vis} cut at 1 – this would lead to slightly lower leptonic background to the taus but clearly the loss in efficiency is substantial. Line 2 represents a cut in p_{vis} of $\sqrt{2}$ (tangential to the circle of the $p_{rad} = 1$ cut). In this case, although the efficiency of tau selection is slightly enhanced, the cut does not eliminate the tails of the background. Thus, for optimum efficiency and level of background, it is seen that a p_{rad} cut is better than a p_{vis} cut.

The cut for the common or **linescan** selection is

- $p_{rad} < 1.0$, linescan

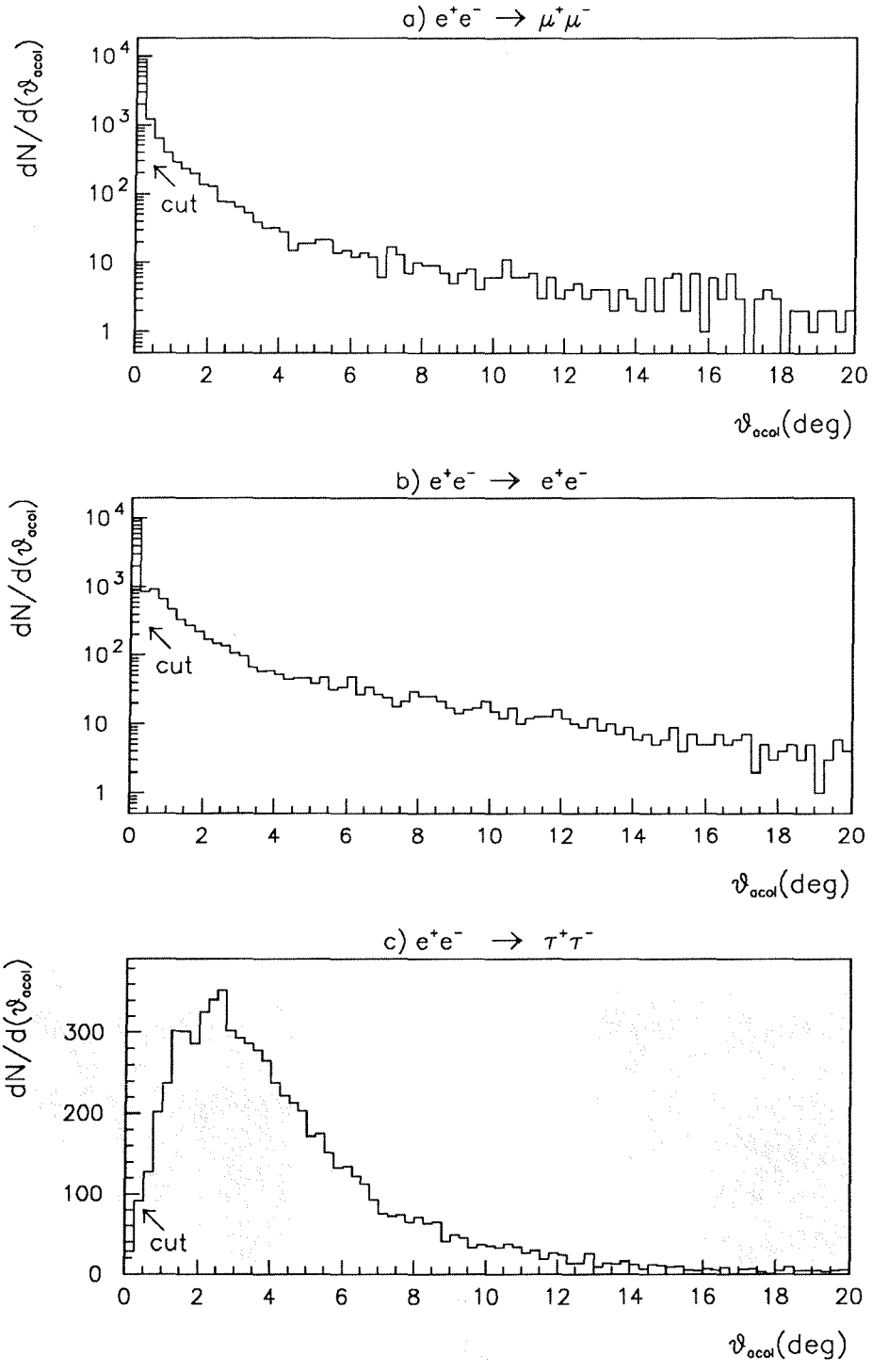

Figure 4.13: *Acollinearity distribution for simulated a)* $e^+e^- \rightarrow \mu^+\mu^-$, *b)* $e^+e^- \rightarrow e^+e^-$ *and c)* $e^+e^- \rightarrow \tau^+\tau^-$ *events.*

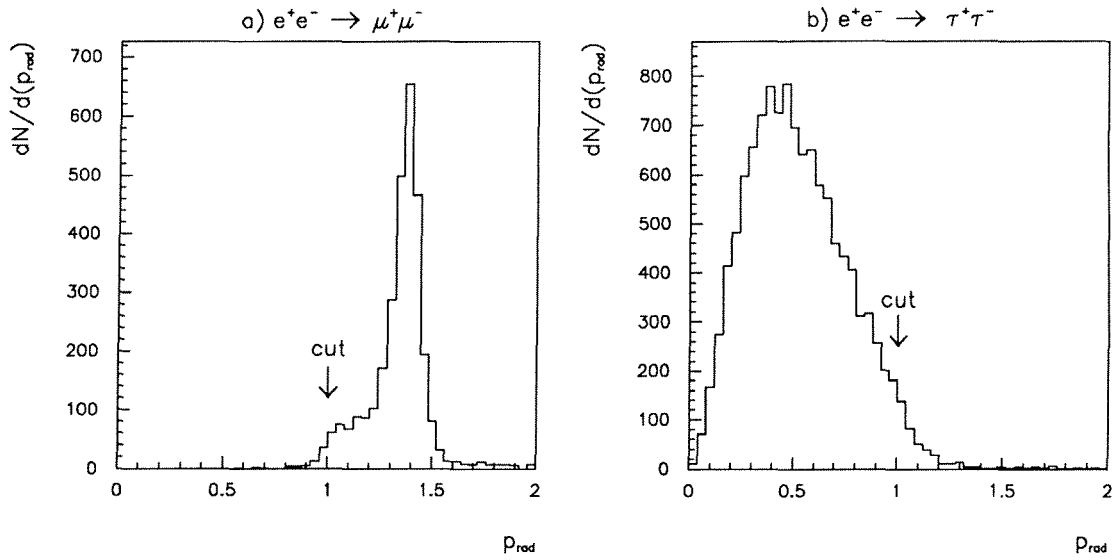

Figure 4.14: *p_{rad} distribution for simulated a) $e^+e^- \rightarrow \mu^+\mu^-$ and b) $e^+e^- \rightarrow \tau^+\tau^-$ events after acollinearity cut at 0.5°. The cut for the linescan selection is shown.*

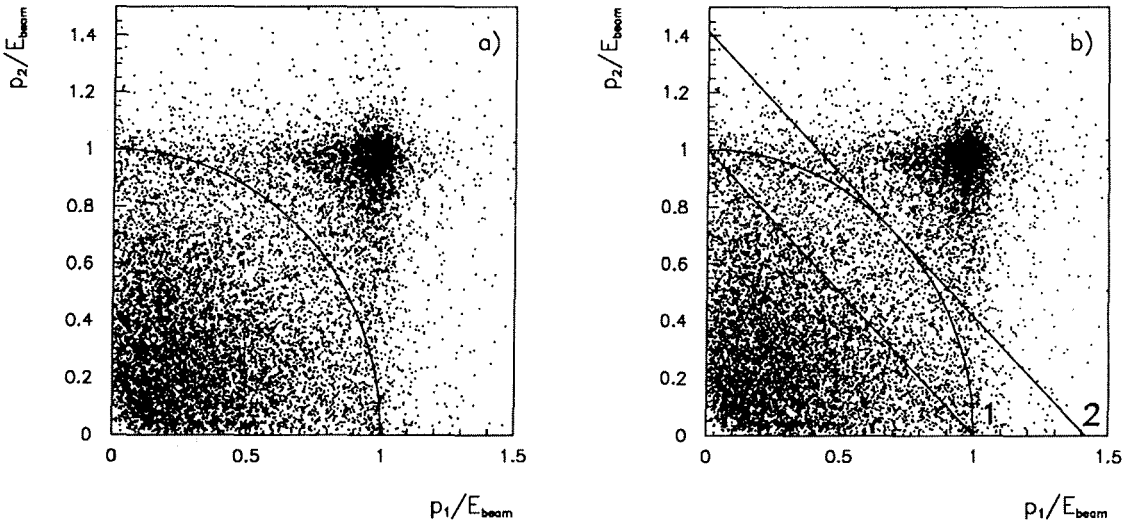

Figure 4.15: *p_1/E_{beam} vs p_2/E_{beam} for data events. a) shows shows a p_{rad} cut at 1. b) shows in addition a p_{vis} cut at 1 (line 1) and a p_{vis} cut at $\sqrt{2}$.*

For the **polarisation** selection, the above cut can severely bias the momentum spectra of the various decay modes. The cut is therefore relaxed to

- $p_{rad} < 1.2$, polarisation

4.5.2 E_{rad} cut

The dimuon background can be controlled effectively with the p_{rad} cut. However, although most of the Bhabha background is also eliminated, the p_{rad} cut is not as effective for two reasons:

1. They tend to have a larger radiative tail and thus more low momentum tracks than dimuons.

2. Electrons interact more in the TPC and barrel RICH, and can start showering before or in the Outer Detector. This degrades the track fitting and leads to poorer momentum resolution.

An electron entering a 'good' region of the HPC can be expected to deposit almost all its energy as an electromagnetic shower of energy $E_{HPC} \approx p$. However, if it enters a crack, the energy resolution is much worse and also, the energy deposited can be considerably less than its momentum.

For similar reasons to the p_{rad} cut, an E_{rad} cut also effectively separates taus from Bhabhas (see Figure 4.16). Even if a photon is radiated, because the energy is taken in a 30° cone, the photon shower is also usually included.

For the linescan selection, it is placed at

- $E_{rad} < 1.0$, linescan

For the polarisation selection, this cut is again relaxed to

- $E_{rad} < 1.2$, polarisation

4.6 Summary of selection cuts and Monte Carlo efficiency

The selection criteria applied in the isolation of the linescan sample of $e^+e^- \rightarrow \tau^+\tau^-$ events are listed in Table 4.2. In total, **6129** $e^+e^- \rightarrow \tau^+\tau^-$ events were found with the linescan selection cuts in the 1991 data set.

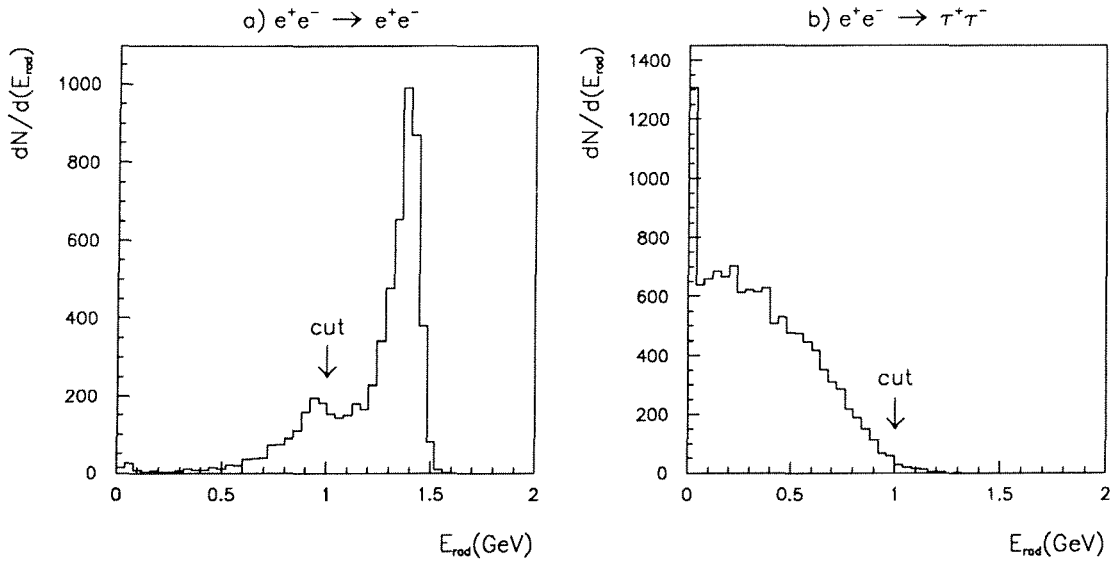

Figure 4.16: *E_{rad} distribution for simulated a) $e^+e^- \rightarrow e^+e^-$ and b) $e^+e^- \rightarrow \tau^+\tau^-$ events after acollinearity cut at 0.5°. The cut for the linescan selection is shown.*

The selection efficiency for $e^+e^- \rightarrow \tau^+\tau^-$ events selected with the above criteria is determined using Monte Carlo events generated with KORALZ and passed through the full detector simulation. From then onwards, these events follow the same analysis chain as the data. The Monte Carlo overall efficiency is found to be 53.73 $\pm$ 0.16 %, where the uncertainty on the efficiency is due to Monte Carlo statistics only.

4.7 Corrections to efficiency of linescan selection

The Monte Carlo efficiency determined has to be corrected for any differences that are found to exist between data and simulation. The main differences are in the following:

1. Momentum resolution is slightly worse in data than in simulation and the distributions are also offset.

2. HPC energy resolution is also better in simulation.

3. TPC cracks are less efficient in data.

4. r impact parameter distribution has larger tails in data.

Each of these differences is described below, and the correction factors required for the linescan selection are given.

$e^+e^- \rightarrow \tau^+\tau^-$ SELECTION CRITERIA	
$2 \leq ntrack \leq 6$	
$\theta_{iso} \geq 160^o$	
$\mid r \mid < 1.5$ cm	
$\mid z \mid < 4.5$ cm	
IFLAG $= -3$, and more than 50 ns from BCO	
$E_{vis} > 0.175\, E_{beam}$	
$p_{rad} < 1.0$	
$E_{rad} < 1.0$	
$\theta_{acol} > 0.5^o$	1 v 1 events
$\mid z_1 - z_2 \mid < 3$ cm	1 v 1 events
$p_T > 0.4$ GeV/c	1 v 1 events

Table 4.2: *Cuts used to select* $e^+e^- \rightarrow \tau^+\tau^-$ *events.*

4.7.1 Momentum distribution differences

From gaussian fits to the momentum distributions, the momentum resolution obtained in data for dimuons was found to be 3.5 % compared with 3.0 % for simulated dimuon events. In addition, a shift in the distribution downwards in data compared to Monte Carlo was observed. The shift was 0.4 GeV/c at 45.6 GeV/c and when correcting simulation, the effect was assumed proportional to momentum. The momenta of the leading tracks in simulation were also smeared to obtain agreement in resolution for the dimuon peak. For each event, a new p_{rad} was calculated from the corrected values of p_1 and p_2. Figure 4.17 shows the comparison between dimuon events in data and in Monte Carlo before and after correction.

Identical smearing and shifting of the leading tracks were applied to the simulated $e^+e^- \rightarrow \tau^+\tau^-$ sample. The correction factor required for the 'bare' Monte Carlo linescan selection efficiency was 1.002 ± 0.002, where the uncertainty stems mainly from the momentum scale uncertainty.

4.7.2 HPC energy differences

The HPC energy resolution in data was 8 % compared to 5 % in Monte Carlo for Bhabhas (see Figure 4.18). The HPC energies in simulated $e^+e^- \rightarrow e^+e^-$ events were

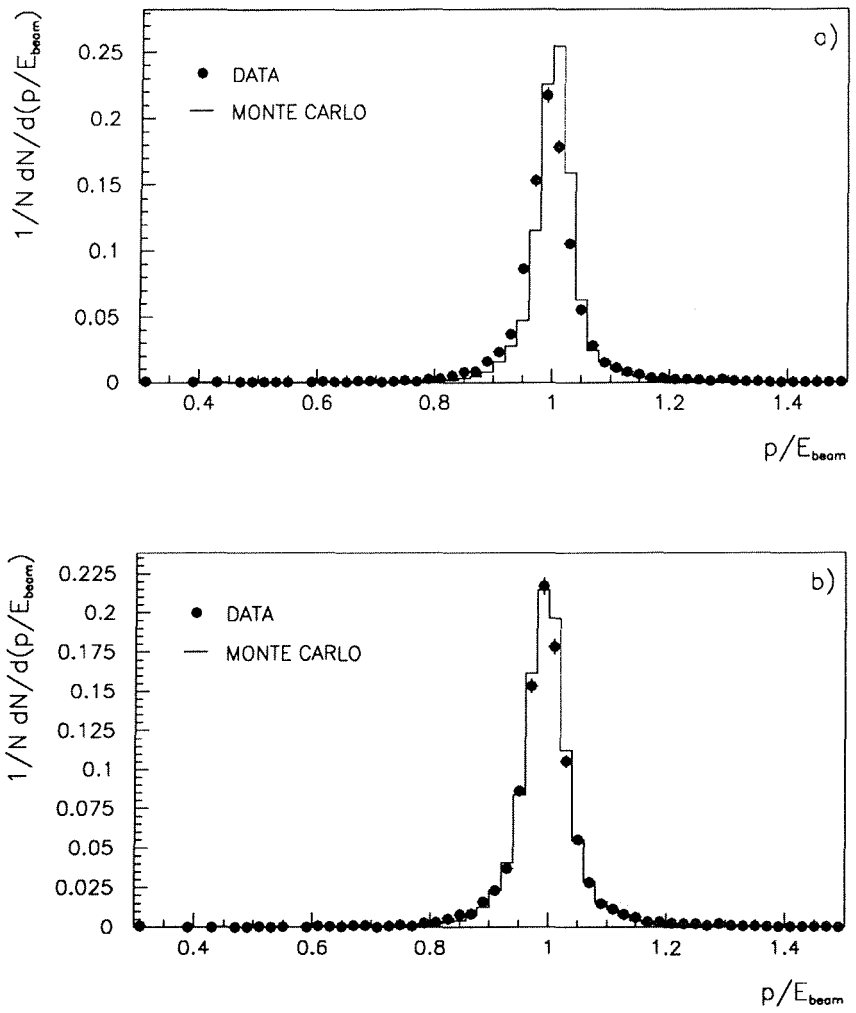

Figure 4.17: *Momentum peak for dimuons selected from data compared with simulation a) before and b) after correction of the simulation.*

smeared to obtain agreement between data and Monte Carlo, and the same smearing applied to simulated $e^+e^- \rightarrow \tau^+\tau^-$ events. A correction factor of 0.998 ± 0.001 was found to be needed for the 'bare' Monte Carlo selection efficiency.

4.7.3 TPC cracks

The track reconstruction efficiency of the TPC is found to be less in the ϕ cracks in data compared to simulation (see Figure 4.19). Events in the 1 v 1 and 1 v N (where N > 1) categories were treated independently. The correction factor required is obtained by normalising the Monte Carlo distribution to the data in the flat region outside $\pm$ 5° around the crack, and observing the difference between the total number of

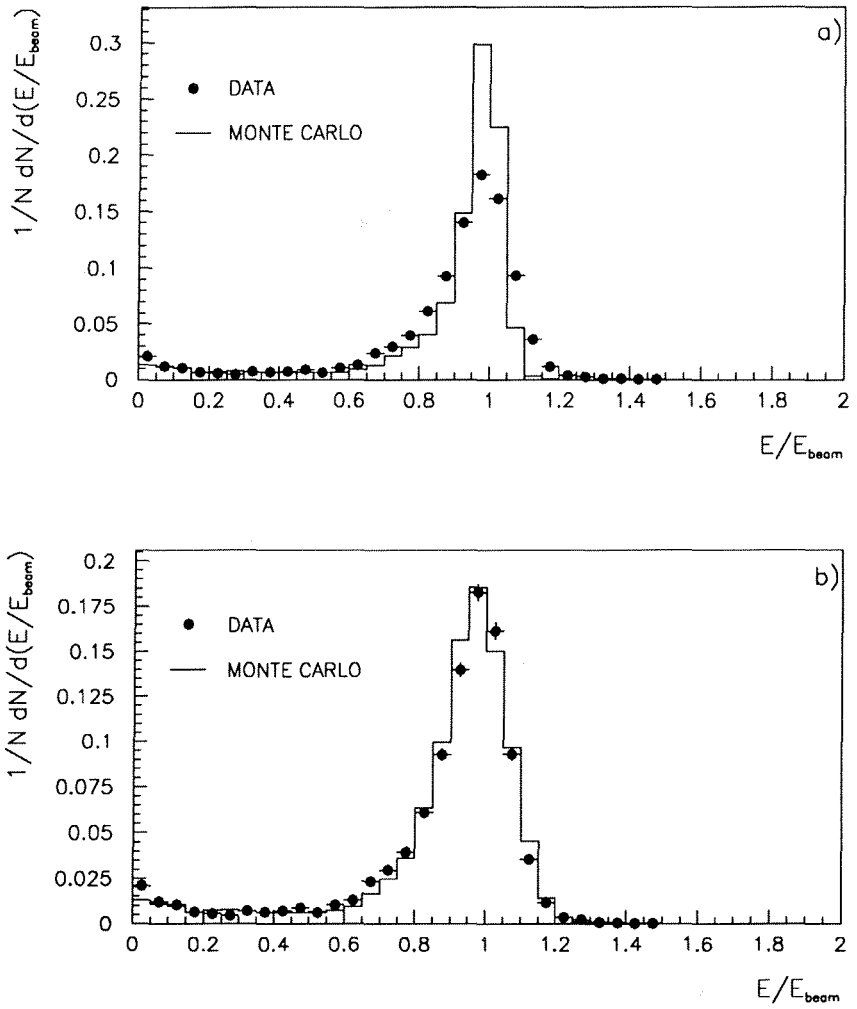

Figure 4.18: *HPC associated energy as function of beam energy for Bhabhas selected in data compared with simulation a) before and b) after correction of the simulation.*

events (taking into account the distribution in ϕ expected for the dimuon and Bhabha backgrounds). It was found to be 0.997 ± 0.003.

4.7.4 r impact parameter differences

The r impact parameter distributions also show disagreement between simulation and data (see Figure 4.19). The differences are found in both 1 v 1 and 1 v N (where N > 1) event topologies and are due to genuine losses in $e^+e^- \rightarrow \tau^+\tau^-$ events as well as to cosmics and poorly reconstructed dimuon and Bhabha events. From a study of the p_{rad} and E_{rad} distributions of the events in the tails and a visual scanning of events, the correction factor was estimated to be 0.992 ± 0.005.

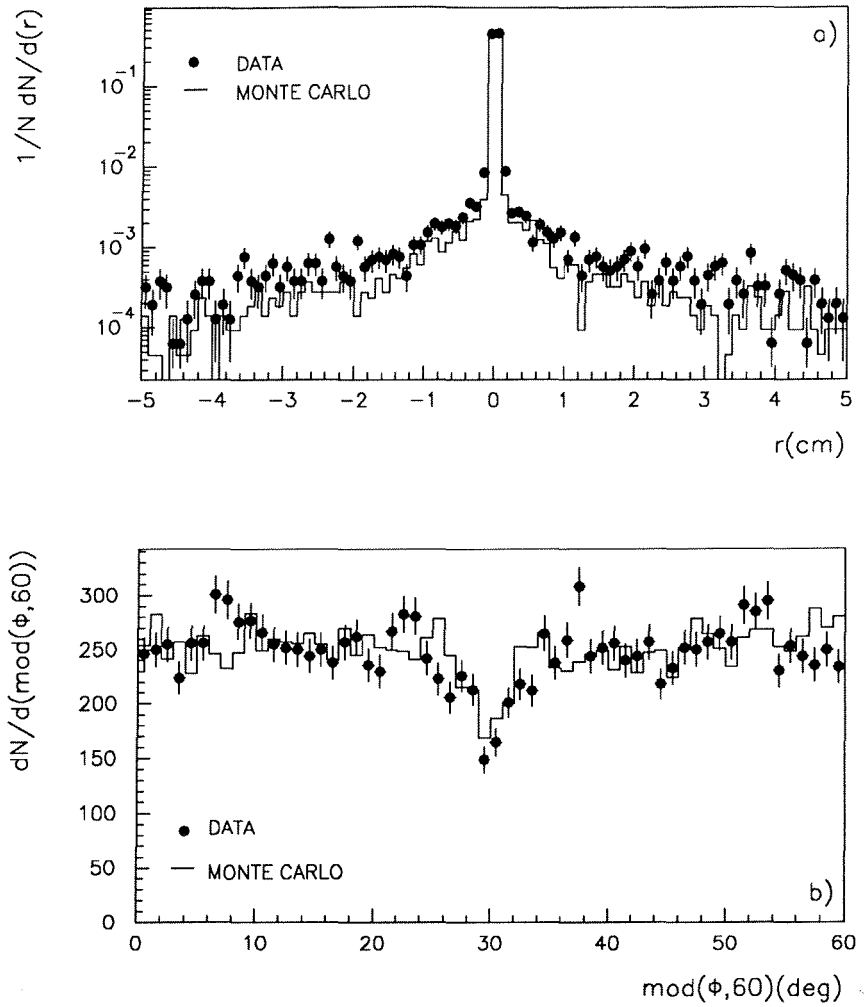

Figure 4.19: *a) r impact parameter distribution for selected taus compared with simulation, and b) ϕ distribution (folded in 60°) for selected taus in the 1 v 1 topology compared with simulation.*

4.8 Final efficiency number and systematics

The effect on the selection efficiency of each of the variables used in the linescan selection is estimated by applying all the cuts except the one being investigated, and varying that by $\pm$ 1 σ (where σ is an estimate of the resolution). If the difference between Monte Carlo (including all backgrounds) and data is statistically significant, a systematic uncertainty of the same amount is assigned. Distributions for some of the variables used comparing data and Monte Carlo are shown in Figure 4.20 and Figure 4.21, and good agreement between them is found. The variables giving rise to systematic uncertainties in this way (in addition to the systematics arising from the correction

factors) were found to be E_{rad}, θ_{acol} and θ_{iso} [5].

The main systematic uncertainties on the selection efficiency are listed in Table 4.3. They are added in quadrature to obtain the total uncertainty.

Systematic source	$\Delta\varepsilon/\varepsilon$
TPC ϕ cracks correction	0.3 %
p_{rad} correction	0.2 %
r impact parameter correction	0.5 %
E_{rad}	0.3 %
acollinearity	0.2 %
isolation angle	0.1 %
MC statistics	0.3 %
Total	0.8 %

Table 4.3: *Systematic uncertainties on the selection efficiency for* $e^+e^- \rightarrow \tau^+\tau^-$.

The efficiency obtained from Monte Carlo is corrected by the estimated correction factors and the efficiency of selection over 4π is found to be 53.14 ± 0.43 %. Within the fiducial region of $43^o < \theta < 137^o$, it is 82.1 ± 0.7 %.

4.9 Estimation of background to linescan selection

The various contributions to the background are estimated from data, and checked against the value obtained from simulation (where it exists) of the background type. Events belonging to the background type being studied are identified from the data using as far as possible an independent selection to the linescan selection. Then all the linescan selection cuts are applied, except the one that is most effective at rejecting the background type being studied. From a knowledge of the simulated distributions of $e^+e^- \rightarrow \tau^+\tau^-$ and $e^+e^- \rightarrow$ *background*, the data distribution for the background is extrapolated to the region inside the cut being applied, and the expected number of events within this region found. This number is then corrected by the identification efficiency to give the background.

A somewhat different procedure, described in Section 4.9.5, is used to estimate the cosmic event background, as there is no simulation available to describe it.

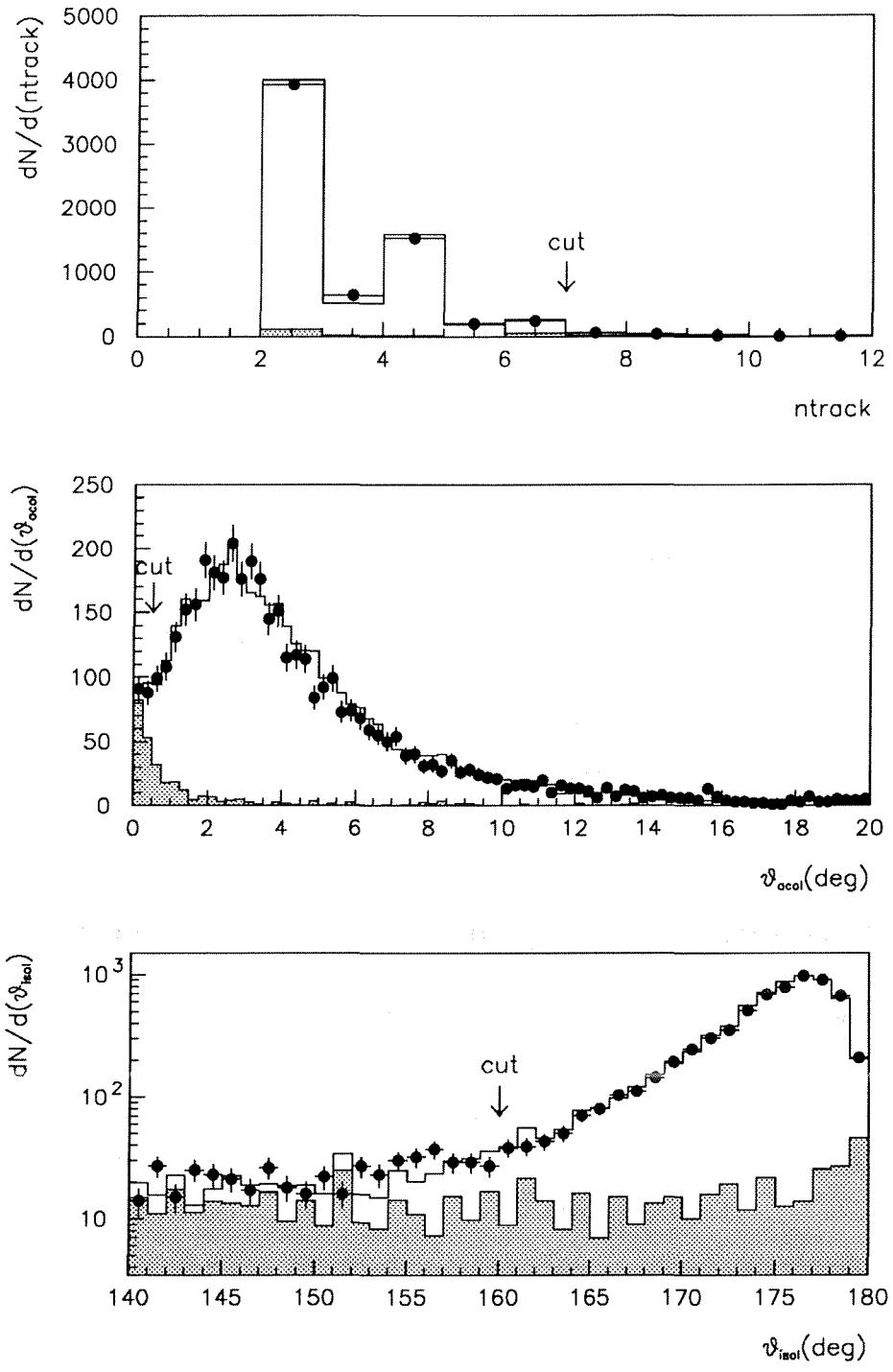

Figure 4.20: *Distributions for data (dots) and Monte Carlo (line) including background (shaded portion) for the variables ntrack, θ_{acol}, and θ_{iso}* [5].

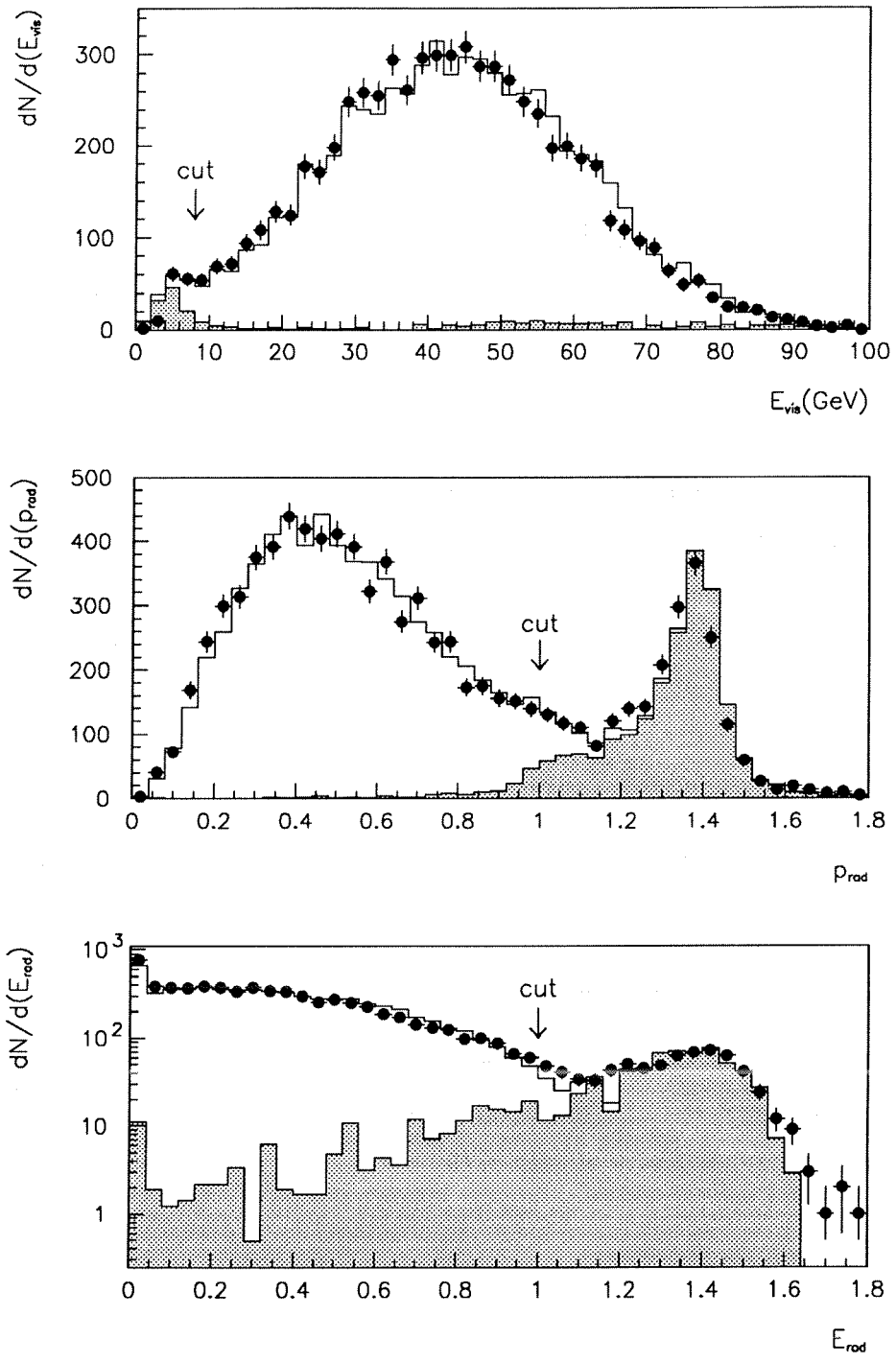

Figure 4.21: *Distributions for data (dots) and Monte Carlo (line) including background (shaded portion) for the variables E_{vis}, p_{rad}, and E_{rad}* [5].

4.9.1 $e^+e^- \rightarrow \mu^+\mu^-$ background

The most effective variable for rejecting this background is p_{rad}. Dimuon events are selected by requiring the leading track in each hemisphere to have at least one muon hit associated. This identification has an efficiency of 80 % for $e^+e^- \rightarrow \mu^+\mu^-$ events, and suppresses most of the $e^+e^- \rightarrow \tau^+\tau^-$. The background obtained is 0.4 $\pm$ 0.2 % [5].

4.9.2 $e^+e^- \rightarrow e^+e^-$ background

The variable considered here is E_{rad}. In order to identify $e^+e^- \rightarrow e^+e^-$ events independently of the linescan selection, it is asked that the leading track in each hemisphere have less than 2 GeV of HCAL energy associated to it. While almost 100 % of $e^+e^- \rightarrow e^+e^-$ events are selected in this way, a lot of $e^+e^- \rightarrow \tau^+\tau^-$ events are also picked up, causing a significant overlap of the two distributions. The $e^+e^- \rightarrow e^+e^-$ distribution is assumed to consist of two gaussians, corresponding to the cases when both electrons enter a good region of the HPC, and when one electron enters a dead region, giving a reduced central value of E_{rad}. The data is fitted for $E_{rad} > 1$, and extrapolated to $E_{rad} < 1$, giving a background of 1.1 $\pm$ 0.4 % [5].

4.9.3 $e^+e^- \rightarrow q\bar{q}$ background

The variable studied here is θ_{isol}, and the identification of events is made by asking that E_{vis} be greater than 20 GeV. The background estimated is 0.8 $\pm$ 0.3 % [5].

4.9.4 $e^+e^- \rightarrow e^+e^-X$ background

The variable θ_{isol} is used again, but the identification of two-photon events requires that E_{vis} be less than 15 GeV. The background obtained is 0.3 $\pm$ 0.1 % (2.0 $\pm$ 0.6 pb overall with a total luminosity of 9915 $\pm$ 19 nb^{-1}) [5].

4.9.5 Cosmic background

The r impact parameter distribution for cosmics is flat, with $(r_1 + r_2)$ peaking strongly around zero. Thus, the quantitative effect of any cuts on a sample of cosmic events can be estimated by selecting a sample of events outside the vertex region in r, applying the cuts one is interested in, and then scaling the number of events surviving to within the vertex region. This was done by looking at events with 2.5 cm $< r <$ 4.5 cm (for $r >$ 4.5 cm, the distribution for cosmics starts to tail off slightly). All the other linescan

Background type	Amount
$e^+e^- \rightarrow e^+e^-$	1.1 ± 0.4 %
$e^+e^- \rightarrow \mu^+\mu^-$	0.4 ± 0.2 %
$e^+e^- \rightarrow q\bar{q}$	0.8 ± 0.3 %
$e^+e^- \rightarrow e^+e^-X$	0.3 ± 0.1 %
Cosmic rays	0.2 ± 0.1 %
Total	2.8 ± 0.6 %

Table 4.4: *Background contributions to the $\tau^+\tau^-$ event selection.*

selection cuts were then applied, and the number of events surviving was assumed to be 4/3 times the number within $r < 1.5$ cm. The background was thus estimated to be 0.2 ± 0.1 %. As a consistency check, almost all the events surviving the selection cuts had muon hits associated to both tracks and thus these events selected outside the vertex were cosmics and not misreconstructed Z^o decays.

NOTE: The same procedure cannot really be used with the z impact parameter, because once one moves outside the vertex region in z to $z > 4.5$ cm, events in the TPC can start to be reconstructed with both tracks in the *same* half of the TPC. This means there is no separation in z visible, even though the event may be out of time, and thus there is no timing information present for these events, and they cannot be used to calculate the cosmic background.

The total background and errors are summarised in Table 4.4.

Chapter 5

Selection of $\tau^- \rightarrow \mu^- \bar{\nu}_\mu \nu_\tau$ decays

Once the initial global $\tau^+\tau^-$ sample has been identified, the individual decay channels of the tau can be searched for. The selection of $\tau^- \rightarrow \mu^- \bar{\nu}_\mu \nu_\tau$ decays (and its charge conjugate) using the DELPHI detector is described in this chapter.

Muons are minimum ionising particles, leaving little energy deposition in the electromagnetic and hadron calorimeters before reaching the muon chambers. In tau decays to muons, not only must the muon be identified as such with good efficiency, but backgrounds due to the other decay modes must be suppressed effectively. The pion decay mode leaves the most similar signal to the muon decay mode, and provides the largest background, but there are contributions from other hadronic decay modes as well. The $e^+e^- \rightarrow \mu^+\mu^-$, $e^+e^- \rightarrow e^+e^-\mu^+\mu^-$, and cosmic backgrounds to the overall $\tau^+\tau^-$ sample can be expected to be enhanced by an order of magnitude within the smaller $\tau^- \rightarrow \mu^- \bar{\nu}_\mu \nu_\tau$ sample and therefore, further cuts must be applied in order to control them.

90° crack

Good detector response is important for a well-understood selection efficiency, and essential for rejection of backgrounds. Almost all the detectors in DELPHI have a crack around the 90^o region, where performance is much hampered. Therefore, an isolated track (which may later be identified as a muon) is required to be out of the region $88^o < \theta < 92^o$. Already, without further cuts, this significantly reduces the cosmic background which is concentrated in this region (see Section 4.3). Dimuon background passing the $p_{rad} < 1$ cut of the selection is also reduced, as some of it is due to poor momentum reconstruction of tracks passing through the TPC crack at 90^o.

5.1 Identification of muons

In the following sections, the response of the HPC, HCAL and muon chambers to muons and other decays of the tau are described, and criteria given for the selection of muons using these detectors.

5.1.1 HPC response and energy cuts

Muons leave very little energy in the HPC, and thus are easily separated from electrons which generally deposit all of their energy as an electromagnetic shower starting in the first few layers of the HPC. An exception to this is when an electron enters a crack in the HPC in which case the energy deposition can be considerably less than that expected from their momentum. Pions generally leave little energy, but can undergo charge exchange interactions and give a large signal. The total HPC energy associated to the track is shown in Figure 5.1 for $\tau^- \rightarrow \mu^- \bar{\nu}_\mu \nu_\tau$, $\tau^- \rightarrow e^- \bar{\nu}_e \nu_\tau$ and $\tau^- \rightarrow \pi^- \nu_\tau$ decays.

A cut is placed on the total HPC energy E_{HPC} (see Figure 5.1) associated to the track. It is required that

- $E_{HPC} < 3$ GeV

Another feature of the muon decay mode is the low percentage which radiate a photon. However, the rho decay mode and multi-pion decay modes with one or more π^0s have a charged pion which could be misidentified as a muon accompanied by photons resulting from the decay of the π^0(s). Where one or more of these photons is detected in the HPC, there will be energy clusters present which are unassociated to the charged track and thus, background due to these modes can be reduced substantially by cutting on the total energy of such clusters.

The difference E_γ between the total HPC energy in a 30° cone around the track (E_{CONE}) and the energy associated to the track (E_{HPC}) is attributed to energy of photons, or to noise (see Figure 5.2). It is required that

- $E_\gamma < 1$ GeV

The HPC cuts are relatively loose to keep efficiencies high and in good agreement with data which has larger tails in the distributions – see Figure 5.19. It is found that the backgrounds are not reduced substantially by cutting harder.

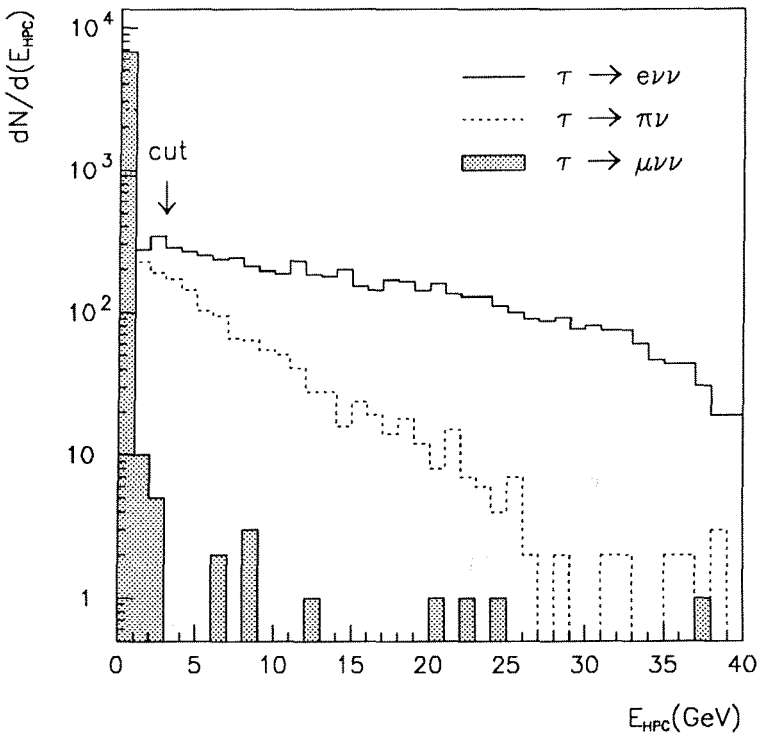

Figure 5.1: *Total HPC energy associated to track in* $\tau^- \rightarrow e^-\bar{\nu}_e\nu_\tau$, $\tau^- \rightarrow \pi^-\nu_\tau$ *and* $\tau^- \rightarrow \mu^-\bar{\nu}_\mu\nu_\tau$ *decays in simulated* $\tau^+\tau^-$ *events.*

5.1.2 HCAL response to muons and hadrons

Total energy

The hadron calorimeter provides the best means of adequately separating muons from hadronic decays. Unless a pion (or kaon) passes through a crack in the HCAL, or interacts in the HPC, most of its energy should be deposited in the form of a hadronic shower in the calorimeter. A muon will be minimum ionising, however, and will give rise to a maximum of one or two streamers in each of the 20 layers of the HCAL. For readout purposes, these layers are grouped together to provide energy deposition information in terms of 4 overall layers. Figure 5.3 shows for simulation a comparison between the total HCAL energy deposition for the decay modes $\tau^- \rightarrow \mu^-\bar{\nu}_\mu\nu_\tau$ and $\tau^- \rightarrow \pi^-\nu_\tau$.

When a muon passes through a layer of the HCAL at $\theta = 90^o$, only one streamer can be produced at most. However, when the muon passes through at an angle to the vertical, the path distance of the particle is lengthened and there is the possibility of

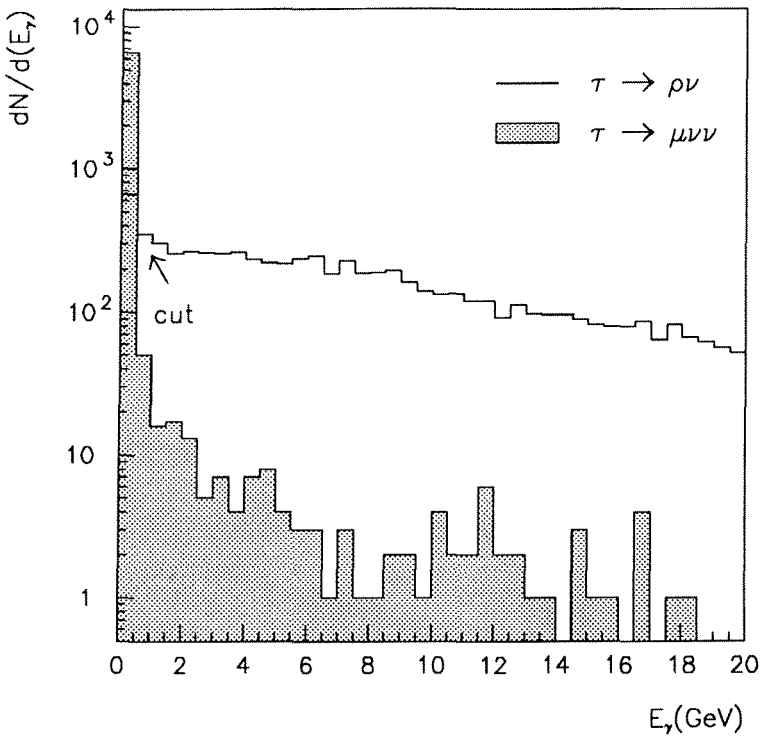

Figure 5.2: *HPC gamma energy within a 30° cone around track for* $\tau^- \rightarrow \rho^- \nu_\tau$ *and* $\tau^- \rightarrow \mu^- \bar{\nu}_\mu \nu_\tau$ *decays in simulated* $\tau^+\tau^-$ *events.*

two streamers per layer after a certain critical angle. In practice, the crossover point is not sharply defined and the effect manifests itself as an increase in the average energy found per minimum ionising particle as one moves away from the $\theta = 90^o$ plane towards the endcap regions. Pions give a relatively flat distribution of total energy over θ.

In both simulation and data, there is a sharp rise in the total energy deposited in a region of a few degrees around 90^o for muons (excluding $88^o < \theta < 92^o$ where due to the dead zone of the HCAL, the energy falls.) This is due to an overestimation of the correction required for charge lost at the ends of tubes in the 90^o plane. Pions do not exhibit this large rise as the pion shower is wide and the charge loss correction compensates for the dead space in $88^o < \theta < 92^o$; the pion energy distribution is more or less flat over the region of correction.

The energy rise is therefore corrected in this analysis for both data and all the decay modes of simulated $e^+e^- \rightarrow \tau^+\tau^-$ events (and in simulated dimuon events also) in order to give a physically more accurate flat distribution for muons in this region, and slightly lower energies for hadrons whose showers lose energy due to the dead space.

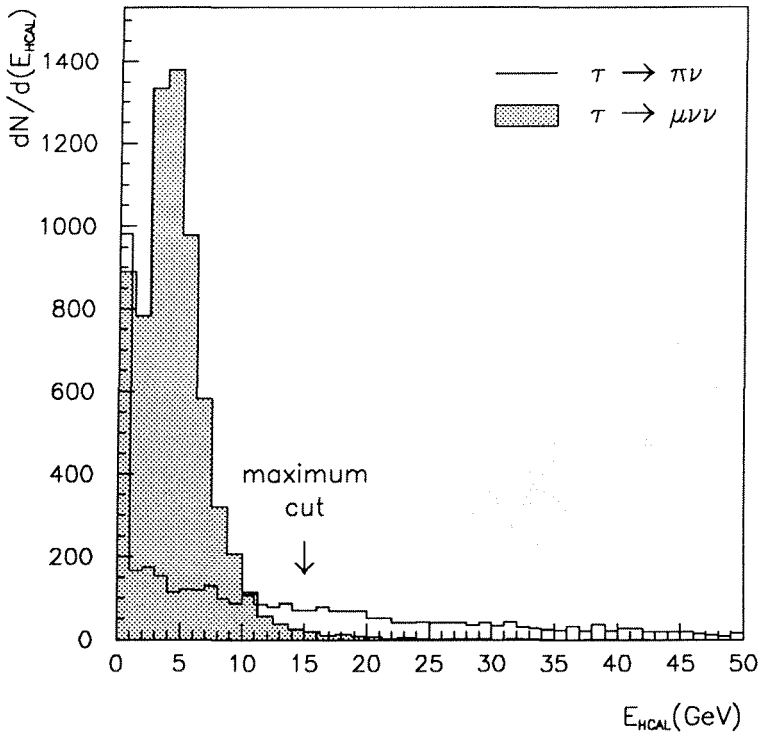

Figure 5.3: *Total HCAL energy associated to track in* $\tau^- \to \pi^-\nu_\tau$ *and* $\tau^- \to \mu^-\bar{\nu}_\mu\nu_\tau$ *decays in simulated* $\tau^+\tau^-$ *events.*

A cut in the total HCAL energy which follows approximately the θ variation seen in the distribution is applied to separate muons from the background of hadrons (see Figure 5.4). When there are only 3 layers present (in the endcap regions) less energy is deposited and so the cut is lower. The actual divisions occur at physical supertower divisions in the HCAL (see Figure 3.11). Because of poor calibration of the 1991 data for $\theta < 47^o$ and $\theta > 133^o$ which is not reproduced in simulation (see Section 5.2.5) the identification of muons is restricted to outside those regions. However, for the rejection of dimuon background, it is useful to have a cut defined.

- $54.5^o < \theta < 88.0^o$ and $92.0^o < \theta < 125.5^o$: $E_{HCAL} < 10.0/\sin^2\theta$ GeV
- $51.5^o < \theta < 54.5^o$ and $125.5^o < \theta < 128.5^o$: $E_{HCAL} < 15.0$ GeV
- $47.0^o < \theta < 51.5^o$ and $128.5^o < \theta < 133.0^o$: $E_{HCAL} < 12.5$ GeV
- $43.0^o < \theta < 47.0^o$ and $133.0^o < \theta < 137.0^o$: $E_{HCAL} < 15.0$ GeV

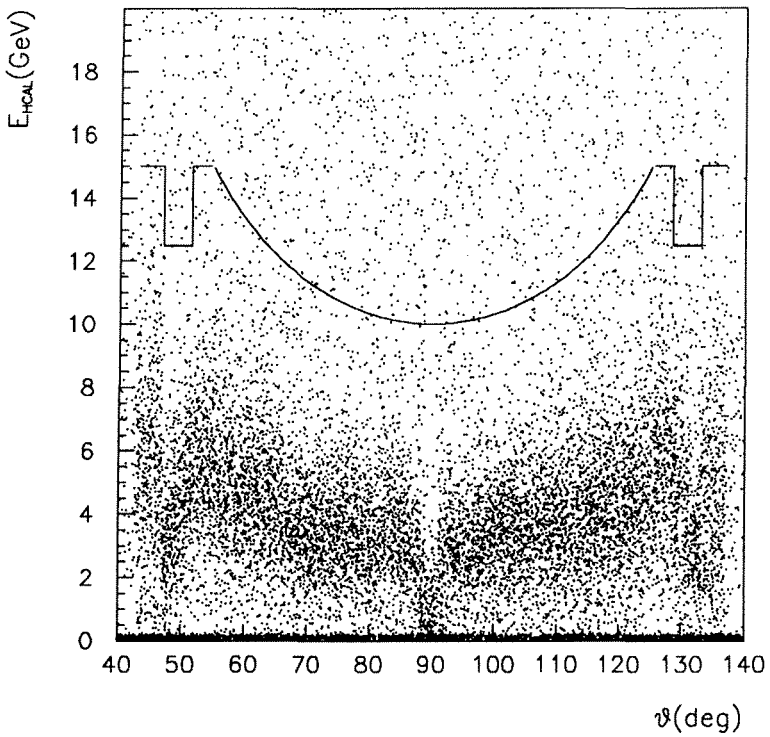

Figure 5.4: *Total HCAL energy deposited for simulated $e^+e^- \rightarrow \tau^+\tau^-$ events that pass the HPC cuts. Muons are concentrated at relatively low energies compared to the background of hadrons, and show a $\sin^2\theta$ dependence well within the barrel. The solid line marks the shape of the cut in E_{HCAL}. Note the energy deposition is much reduced in the dead region of $88^\circ < \theta < 92^\circ$.*

Layer Response

The total energy is the sum of the energy depositions in the four layers of the calorimeter. The proportions of the total energy in each of the layers is quite different for muons and hadrons – muons leave roughly the same amount in all four layers, whereas hadrons, interacting strongly in the material of the HCAL, lose most of their energy in the first two layers. This can be seen by plotting the quantity

$$\mathrm{R} = \frac{\mathrm{H3} + \mathrm{H4}}{\mathrm{H1} + \mathrm{H2}} \tag{5.1}$$

where H1 is the energy associated to the track in layer 1, and so on. R is thus in principle $\ll 1$ for hadrons and ≈ 1 for muons, but does not show sufficiently clean separation or efficiency to be used as a cut. The individual layer energy and R distributions for muons and pions are shown in Figures 5.5 and 5.6.

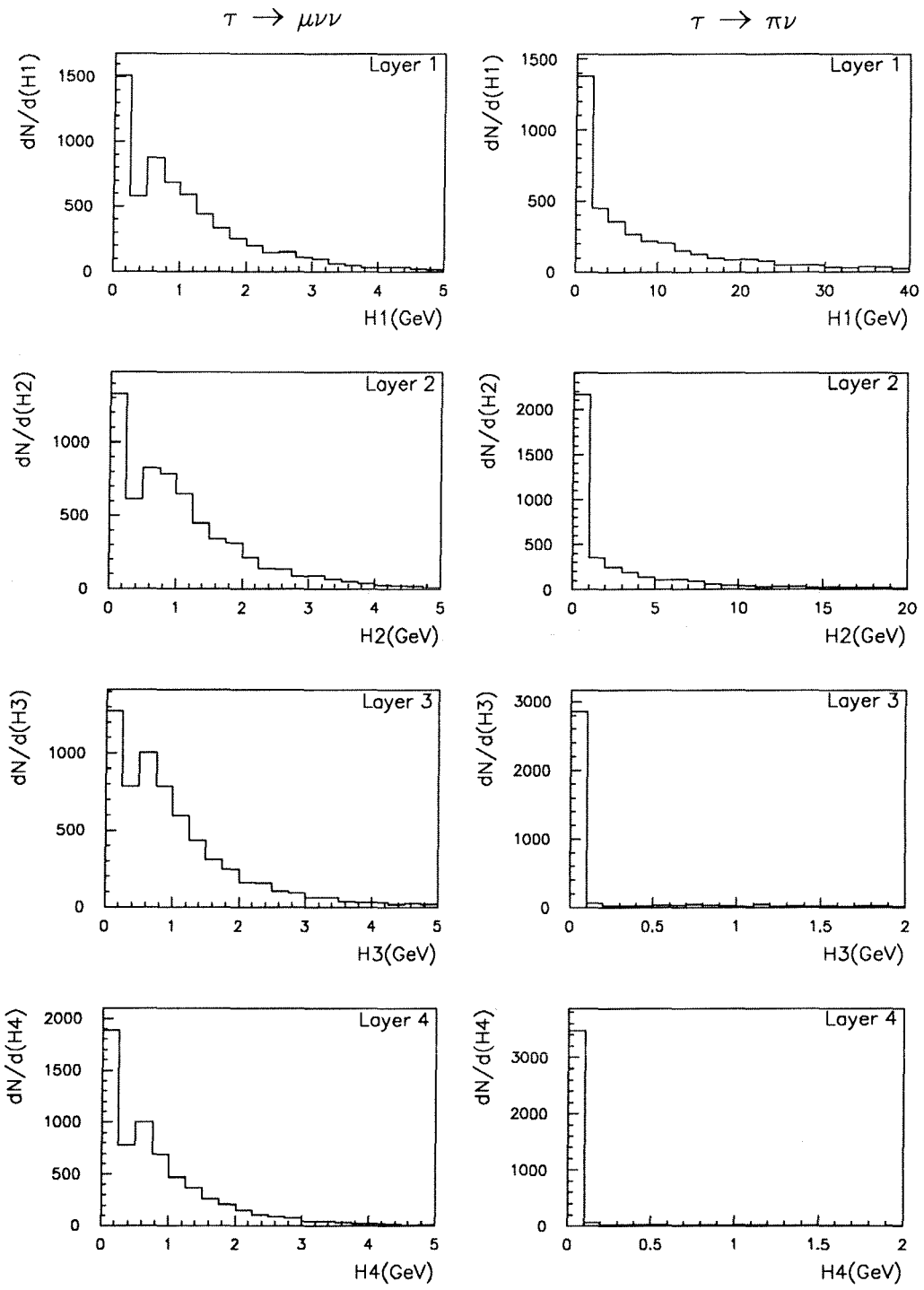

Figure 5.5: *Energy deposited in the individual layers of the HCAL for* $\tau^- \to \mu^- \bar{\nu}_\mu \nu_\tau$ *decays (left) and* $\tau^- \to \pi^- \nu_\tau$ *decays (right) in simulated* $\tau^+\tau^-$ *events. Note different energy scales for the pion layer energies.*

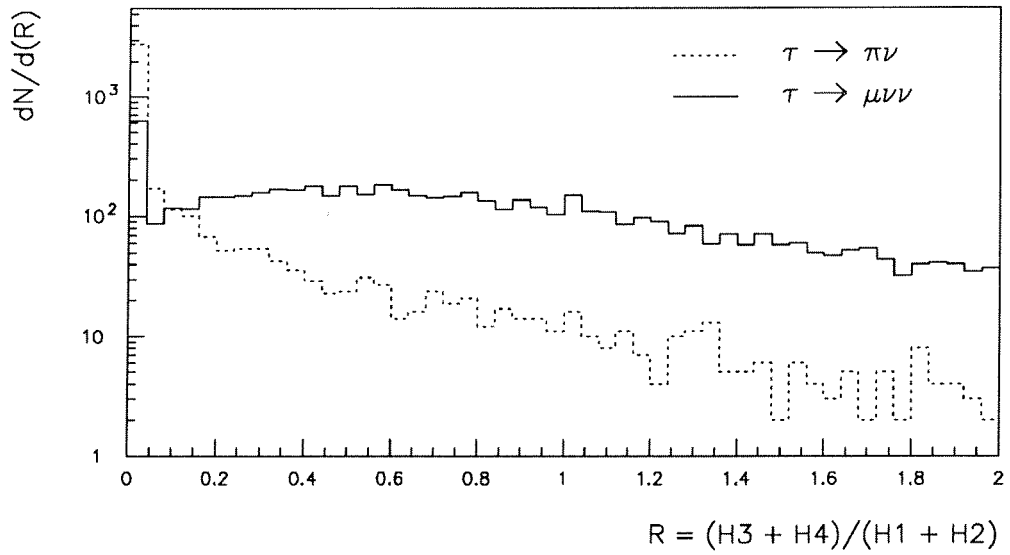

Figure 5.6: *Ratio of energy deposited in the last two layers of the HCAL to that deposited in the first two (given (H1 + H2) > 0) for simulated* $\tau^- \rightarrow \mu^- \bar{\nu}_\mu \nu_\tau$ *and* $\tau^- \rightarrow \pi^- \nu_\tau$ *decays.*

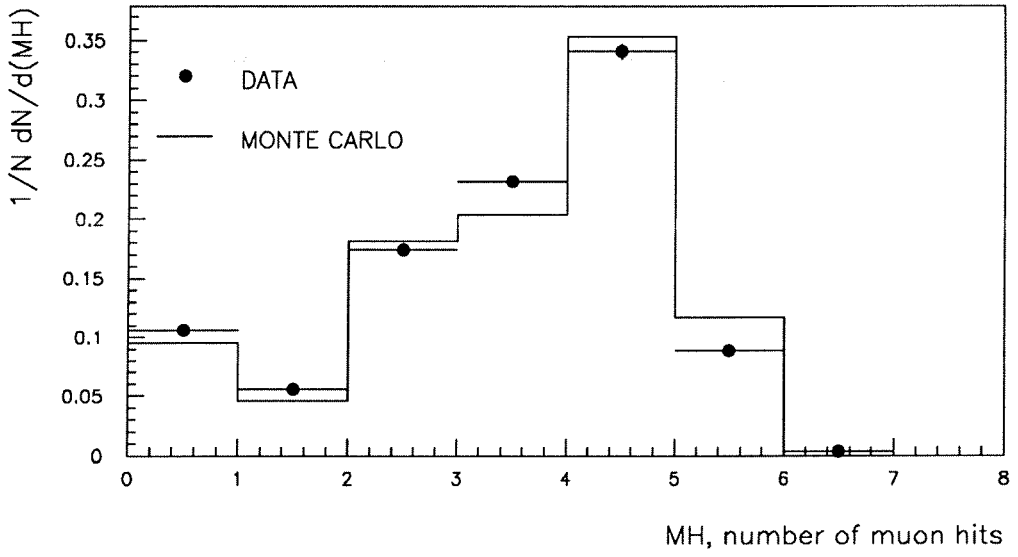

Figure 5.7: *Number of muon hits associated to track for dimuons selected from data and simulation.*

5.1.3 Muon chambers response

The innermost layer of the muon chambers lies within the iron of the HCAL, sandwiched between layers 3 and 4. The outer layer lies just outside layer 4 of the HCAL, directly above the inner layer, and the peripheral layer covers the gaps in ϕ between neighbouring outer layers (see Figure 3.12). As each of these layers consists of two rows of drift tubes, the number of hits associated to a track, MH, is between zero and six (see Figure 5.7). Any punchthrough pions will tend to leave hits mainly in the inner layer.

5.1.4 Selection of muon *candidates*

A charged track is classified as a muon *candidate* if it succeeds in penetrating through to the outermost layers of the HCAL, or leaves hits in the muon chambers. The actual criterion is θ-dependent, as there is a dead zone for the barrel muon chambers and fourth layer of the HCAL, and reduced efficiency for the third layer in the transition from barrel to endcap regions (see Figure 5.8).

The *candidate* requirement is

- $54.5^o < \theta < 88.0^o$ and $92.0^o < \theta < 125.5^o$: MH or H4 > 0
- $51.5^o < \theta < 54.5^o$ and $125.5^o < \theta < 128.5^o$: MH or H4 or H3 > 0
- $47.0^o < \theta < 51.5^o$ and $128.5^o < \theta < 133.0^o$: MH or H4 or H3 > 0
- $43.0^o < \theta < 47.0^o$ and $133.0^o < \theta < 137.0^o$: MH or H4 or H3 > 0

Although in this analysis muons are not selected outside the region 47^o to 133^o, it is useful to define a *candidate* criterion in this region in order to reject dimuon background (see Section 5.3.3).

A track is considered to be an *identified* muon if it satisfies the *candidate* requirement as well as the calorimeter energy cuts which have been given above. The minimum momentum of tracks leaving hits in the muon chambers is found to be around 2 GeV/c (see Figure 5.18) and therefore to ensure good agreement between simulation and data it is asked that

- $p > 0.066 E_{beam}$ (3 GeV/c at $E_{beam} = 45.6$ GeV)

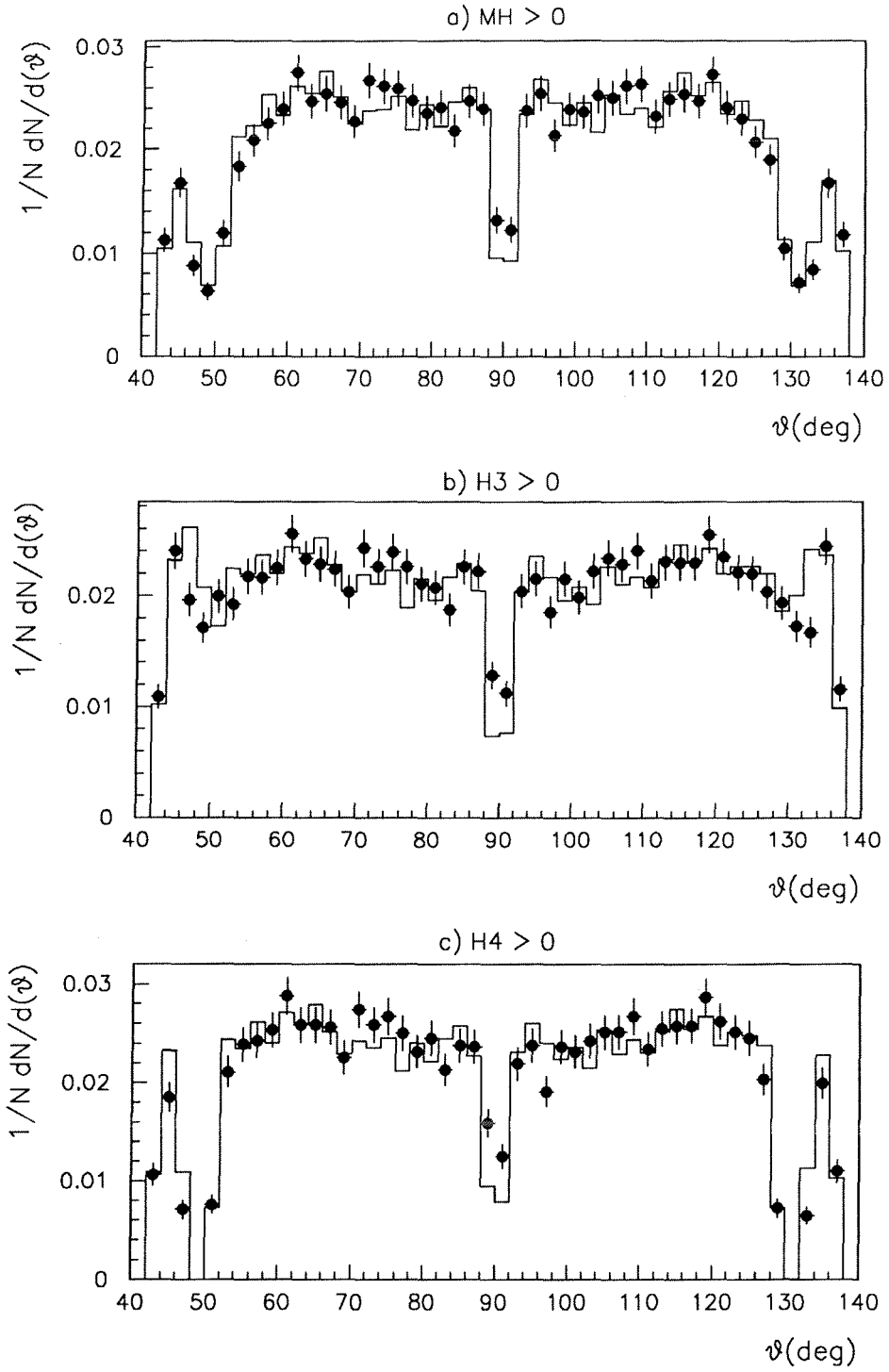

Figure 5.8: *θ of tracks in dimuons selected from data (dots) and simulation for which a) MH > 0, b) H3 > 0 and c) H4 > 0, showing the inefficiencies in the regions 88° < θ < 92° (90° crack) and 46° < θ < 52°, 128° < θ < 134° (gap between barrel and endcap detectors).*

MUON IDENTIFICATION CRITERIA		
$p > 0.066 E_{beam}$		
$47^o < \theta < 133^o$		
$E_{HPC} < 3$ GeV		
$E_\gamma < 1$ GeV		
$54.5^o < \theta < 88^o$ and $92^o < \theta < 125.5^o$	$E_{HCAL} < 10/\sin^2\theta$ GeV	MH or H4 > 0
$51.5^o < \theta < 54.5^o$ and $125.5^o < \theta < 128.5^o$	$E_{HCAL} < 15$ GeV	MH or H4 or H3 > 0
$47^o < \theta < 51.5^o$ and $128.5^o < \theta < 133^o$	$E_{HCAL} < 12.5$ GeV	MH or H4 or H3 > 0

Table 5.1: *Muon identification criteria for selection of* $\tau^- \rightarrow \mu^- \bar{\nu}_\mu \nu_\tau$ *decays.*

The identification criteria are summed up in Table 5.1.

The efficiency of the identification criteria given that $p > 0.066 E_{beam}$ and the track is within the fiducial region defined is around 94 %. The criteria are essentially independent.

The 'bare' background estimated from simulation alone due to other decay modes of the tau is 1.5 %, but as described in Section 5.2.9, this needs to be corrected using data. The proportions of the decay modes making up the background are given in Table 5.2. The distribution in θ of the background is shown in Figure 5.9 and is approximately flat.

Decay mode	e	π	ρ	a_1	K	K^*	$n\pi$
Contribution	–	73 %	13 %	1 %	10 %	3 %	–

Table 5.2: *Percentage contributions of the non-muonic decay modes of the tau to the total internal background (errors are of the order ± 2 %) in simulated* $e^+e^- \rightarrow \tau^+\tau^-$ *events.*

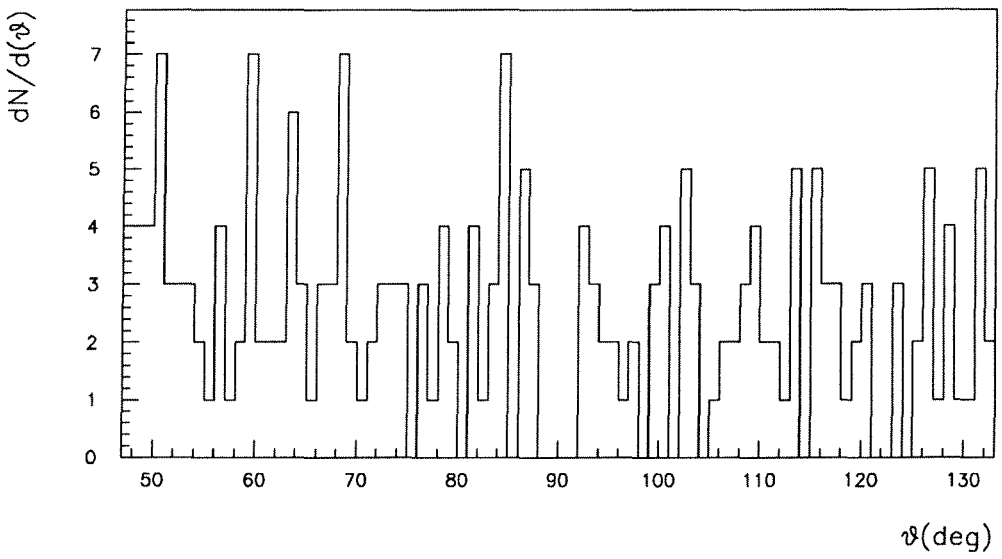

Figure 5.9: *θ distribution of background to the $\tau^- \rightarrow \mu^- \bar{\nu}_\mu \nu_\tau$ decay mode from other decay modes of the tau in simulated $e^+e^- \rightarrow \tau^+\tau^-$ events.*

5.2 Comparison with data

It is important that the distributions of key variables and efficiencies for the cuts implemented show agreement between data and simulation for muons across the full momentum range, in order that the efficiency for muon identification in simulation be realistic. In addition, the background from simulation should show agreement with that estimated from data. The efficiency of each of the three calorimetric cuts and of the *candidate* requirement, together with the efficiency for muon *identification* which is the combination of all four, is shown as a function of momentum for simulated $\tau^- \rightarrow \mu^- \bar{\nu}_\mu \nu_\tau$ decays in Figure 5.10. The dependence of the E_γ cut shows a rise with momentum as muons with lower momenta tend to have radiated photons and thus to have migrated downwards from higher momenta bins. Bremsstrahlung radiation in the HCAL accounts for the fall in efficiency of the E_{HCAL} cut with momentum as muons with higher momenta produce more photons in the HCAL and give a higher energy signal. No dependence can be seen with momentum for the E_{HPC} cut or for the *candidate* requirement (given that the muon has $p > 0.066 E_{beam}$).

To perform these studies, muons and pions must be selected from real data across the full momentum range. For the E_{HPC} cut and the *candidate* requirement, if the efficiencies can be checked for consistency at the low and high momentum ends, then

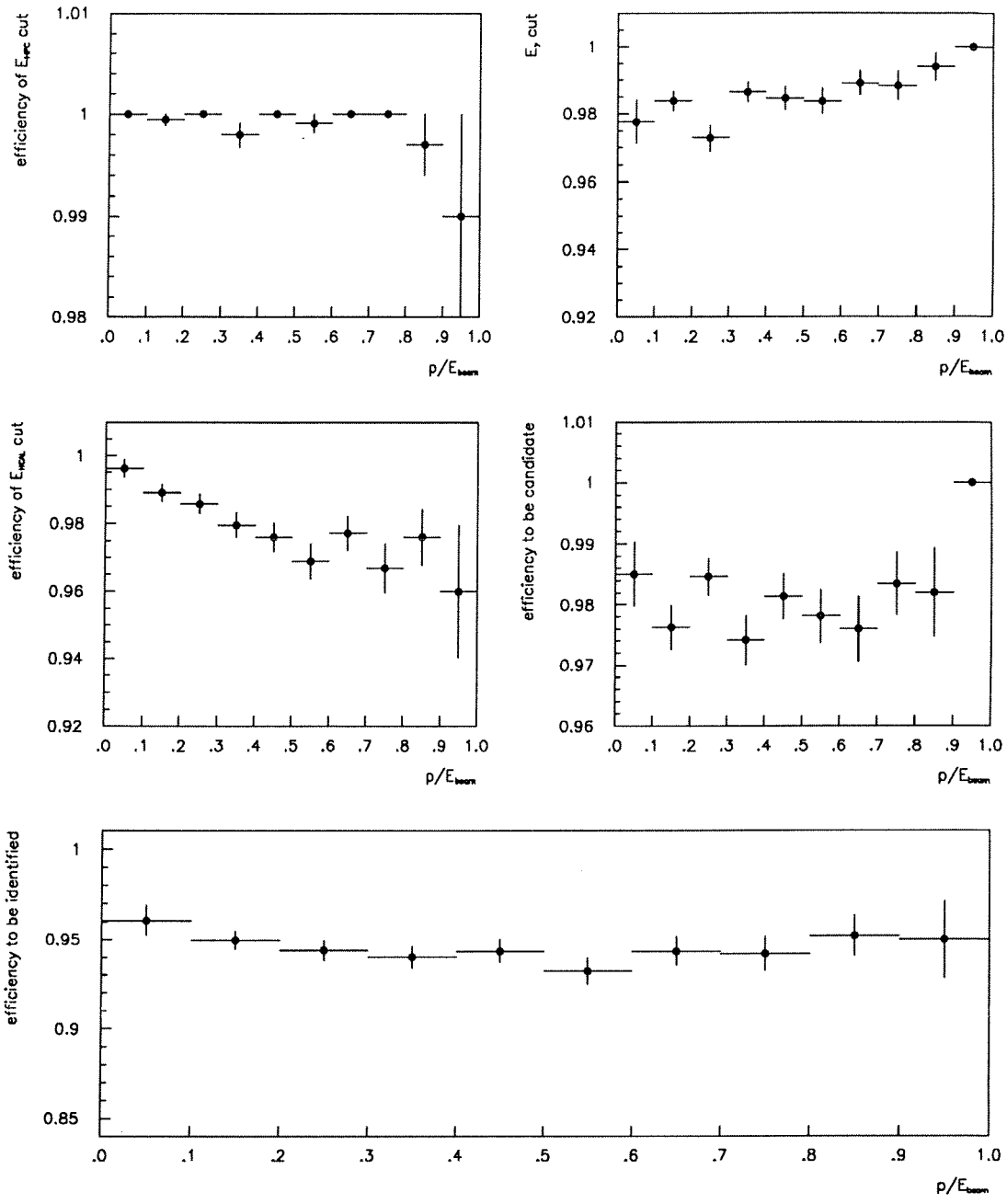

Figure 5.10: *Efficiency of the calorimetric cuts,* candidate *requirement and overall identification for simulated* $\tau^- \to \mu^- \bar{\nu}_\mu \nu_\tau$ *decays as a function of measured momentum. The muon is already required to have momentum* $p > 0.066 E_{beam}$ *and to be within the region* $47° < \theta < 133°$.

it may be assumed that the efficiencies are flat across the momentum range, as they are flat in Monte Carlo. The efficiencies of the E_{HCAL} cut and the E_γ cut should be checked across the full range as they are not flat.

5.2.1 High momentum muon sample

$e^+e^- \rightarrow \mu^+\mu^-$ events provide a relatively large statistics sample of muons on which to study efficiencies and distributions. Events are selected using cuts which will eliminate $\tau^+\tau^-$ events. Also, although cosmic events provide a muonic sample, it is best to exclude them as they could be out of time with respect to some detectors and not others, biasing efficiency calculations.

The cuts used to select $e^+e^- \rightarrow \mu^+\mu^-$ events were:

- $ntrack = 2$
- $\theta_{acol} < 0.5^o$
- $| r | < 1$ cm
- $| z | < 3$ cm
- $| z_1 - z_2 | < 0.5$ cm
- $p_{rad} > 1.1 E_{beam}$

Events with any tracks in the region 88^o to 92^o are not considered. The track in one hemisphere is then tagged as a muon and studies made on the opposite track. In the region where there are muon chambers (θ from 51^o to 88^o and from 92^o to 129^o) the tag is:

- MH ≥ 1

In the region θ from 43^o to 51^o and from 129^o to 137^o where the efficiency of the muon chambers is much reduced, the tag is based on calorimeter cuts:

- $E_{HPC} < 1$ GeV
- $E_\gamma < 0.1$ GeV
- $E_{HCAL} < 20$ GeV

When these cuts were run on samples of simulated $e^+e^- \rightarrow e^+e^-$ and $e^+e^- \rightarrow \tau^+\tau^-$ events, a negligible fraction survived; 9694 'muons' were tagged from data.

5.2.2 Low momentum muon sample

The two-photon process $e^+e^- \rightarrow e^+e^-\mu^+\mu^-$ provides a sample of low momentum muons with which to study efficiencies. However, the statistics of the sample are much lower than the $e^+e^- \rightarrow \mu^+\mu^-$ sample. The cuts used to select the events were:

- $ntrack = 2$
- $\theta_{iso} < 160^o$
- $E_{vis} < 15$ GeV

A track was tagged as a 'muon' if it had momentum greater than $0.066E_{beam}$ and if the opposite side satisfied:

- MH ≥ 1

for the region 51^o to 88^o and 92^o to 129^o, and

- $E_{HCAL} > 0$

outside it. In this way, the number of muons found was 177. The number of simulated $\tau^+\tau^-$ events surviving these cuts was found to be negligible. The momentum spectra for the dimuon and two photon events are shown in Figure 5.11.

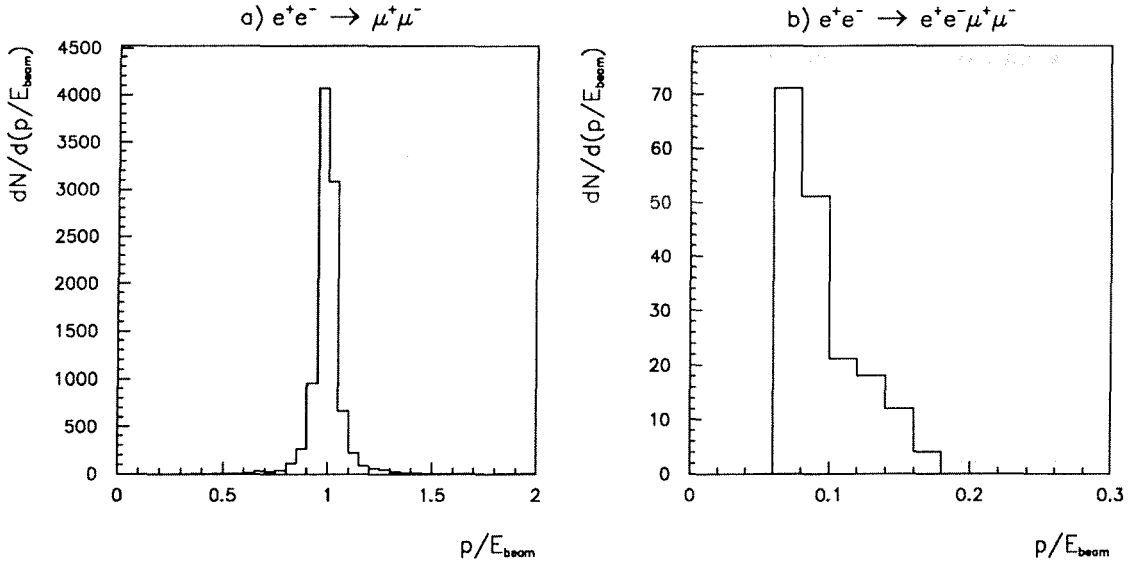

Figure 5.11: *Momentum as function of beam energy for muons selected in data from a) $e^+e^- \rightarrow \mu^+\mu^-$ events and b) $e^+e^- \rightarrow e^+e^-\mu^+\mu^-$ events.*

5.2.3 Intermediate momentum muon sample

For a sample of muons with a momentum range between that of dimuon and two photon events, a subsample of the $\tau^- \rightarrow \mu^- \bar{\nu}_\mu \nu_\tau$ decays is selected by requiring that a track have 3 or more muon hits associated. This ensures that any pions punching through are much reduced than if one simply asked for one or more muon hits, as they have to leave hits in the inner muon chambers, and traverse the whole of the fourth layer in the HCAL, before leaving a third hit in the outer layers. To eliminate background from the external sources of dimuons, cosmics and two photon events, it is also required that the track in the opposite hemisphere not be a *candidate.*

5.2.4 Pion sample

Pions can be selected from real data by identifying rho decays or other multi-pion decays which have a single charged pion and neutral π^0s. The routine used to make this selection is a modified version of [71]. Typically, such decays have neutral energy clusters in the HPC due to photons resulting from the decay of the π^0. It is important to suppress strongly the possibility of identifying muons using the pion selection criteria, as these will significantly distort any conclusions about the levels of pion punch-throughs and background.

The initial selection asks for:

- an isolated charged track in the hemisphere
- at least one neutral HPC cluster in the hemisphere
- $\theta_{acol} > 0.5^o$
- $p_{rad} < 1.3$
- $E_{rad} < 1.2$
- Momentum of track in opposite hemisphere $< 0.85 E_{beam}$

where the last four cuts reduce $e^+e^- \rightarrow e^+e^-$ and $e^+e^- \rightarrow \mu^+\mu^-$ events in the sample to a negligible fraction.

The most energetic neutral in a cone of $> 2^o$ and $< 16^o$ around the track is then selected as the 'primary' neutral. The invariant mass of this neutral assuming it is a π^0 and the

charged track assuming it is a pion is then calculated using the formula

$$M_{INV} = \sqrt{M_{\pi^0}^2 + M_{\pi^+}^2 + 2pE_{neutral}(1 - \cos\theta)} \tag{5.2}$$

where $M_{\pi^0} = 0.1350$ GeV/c^2 is the mass of the π^0, $M_{\pi^+} = 0.1396$ GeV/c^2 is the mass of the charged pion, $E_{neutral}$ is the measured energy of the primary neutral and θ is the angle found between the track and the neutral. The distribution for M_{INV} is shown in Figure 5.12. In order to identify the track as a pion, the following cuts are then applied:

- $E_{neutral} > 5$ GeV
- 0.4 GeV/c^2 $< M_{INV} <$ 1.1 GeV/c^2

The momentum spectrum of particles selected as pions using these cuts from data compares well with that expected from simulated $e^+e^- \rightarrow \tau^+\tau^-$ events (see Figure 5.13), but is softer than that for $\tau^- \rightarrow \pi^-\nu_\tau$ decays.

When the pion selection routine was run on simulated $e^+e^- \rightarrow \tau^+\tau^-$ events, a negligible fraction of leptons were tagged as pions (see Table 5.3); 1690 pions were tagged from data.

The selected pions can be used to study pion response in the HPC, HCAL and muon chambers.

Decay mode	e	μ	π	ρ	a_1	K	K^*	$n\pi$
% tagged	0.30	0.05	0.94	36.38	24.26	1.13	13.17	19.56

Table 5.3: *Percentage of the decay modes of the tau tagged by the pion selection cuts in simulated $e^+e^- \rightarrow \tau^+\tau^-$ events.*

5.2.5 HCAL endcap regions

In 1991, the calibration constants for the endcap/barrel overlap regions in the HCAL from $43^o < \theta < 47^o$ and $133^o < \theta < 137^o$ were found using pions selected in hadronic events. The minimum ionising signal was about a factor 2 higher in data than in simulation (see Figure 5.14).

It was decided to exclude these endcap regions as to correct the signals would lead to a poorer understanding of efficiencies and backgrounds.

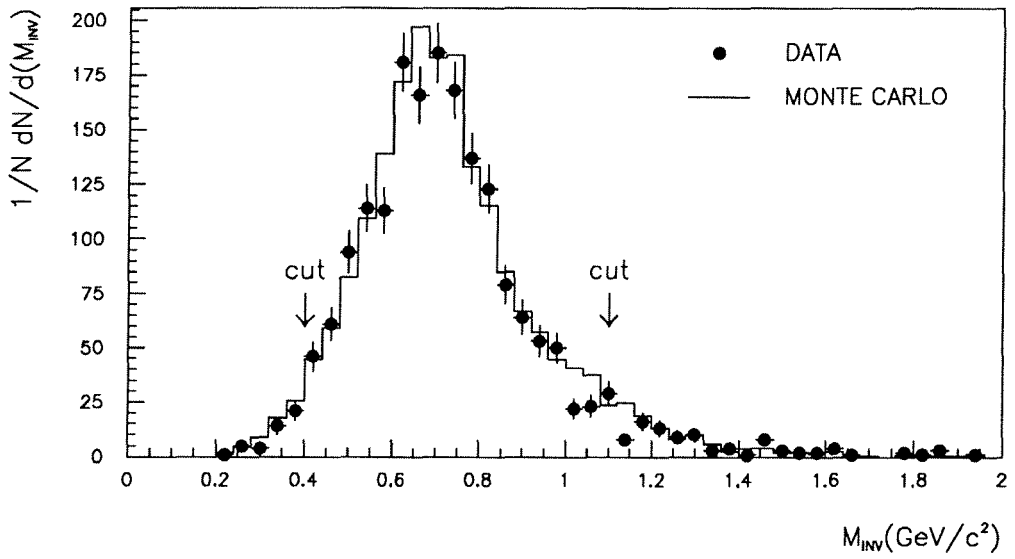

Figure 5.12: *Invariant mass of most energetic HPC neutral and single charged particle for events selected in data compared with simulated $e^+e^- \rightarrow \tau^+\tau^-$ events after all other pion selection cuts have been applied.*

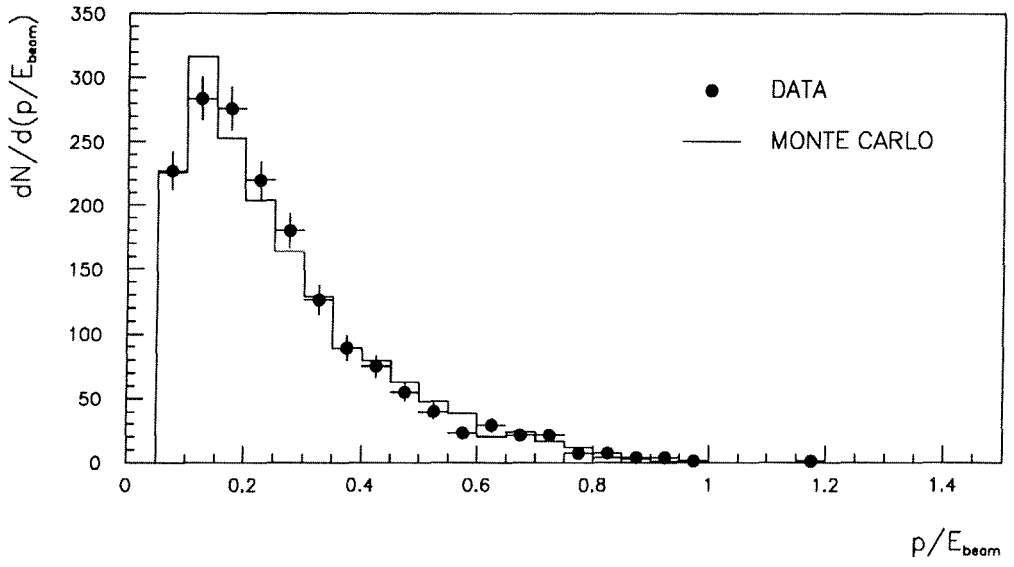

Figure 5.13: *Momentum as function of beam energy for pions selected in data and simulated $e^+e^- \rightarrow \tau^+\tau^-$ events.*

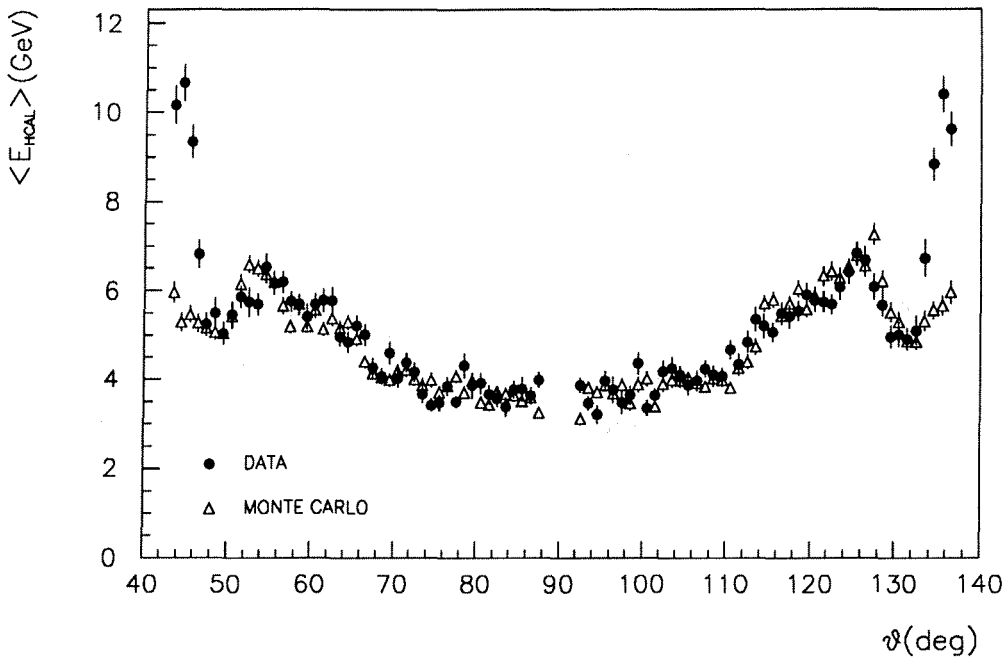

Figure 5.14: *Average HCAL energy deposited (for $E_{HCAL} > 0$) as function of θ for dimuons selected from data and simulation.*

5.2.6 θ variation of total HCAL energy

The total energy deposited by dimuons selected from data and simulation is shown as a function of hypertower divisions in the HCAL in Figure 5.15. These divisions occur in 11.8° segments from $\theta = 90°$ out towards either endcap (refer to Figure 3.11). Minor corrections were applied to obtain good agreement between data and simulation in some of the hypertowers. These consisted of simple scaling of the layer energies in simulation for muons and resumming to obtain the total energy after resetting the threshold per layer at 0.15 GeV.

The overall total energy deposited for dimuons after these corrections shows good agreement between data and simulation (see Figure 5.16). The efficiency of the cut in total HCAL energy was found to be 97.55 ± 0.16 % for dimuons selected in data, and 97.39 ± 0.12 % for dimuons selected in simulation after corrections.

The energy distribution for pions selected as described in Section 5.2.4 in both data and simulated $e^+e^- \rightarrow \tau^+\tau^-$ events also agrees well. The corrections have a negligible effect on the pion distributions and background, and thus are not applied to hadrons.

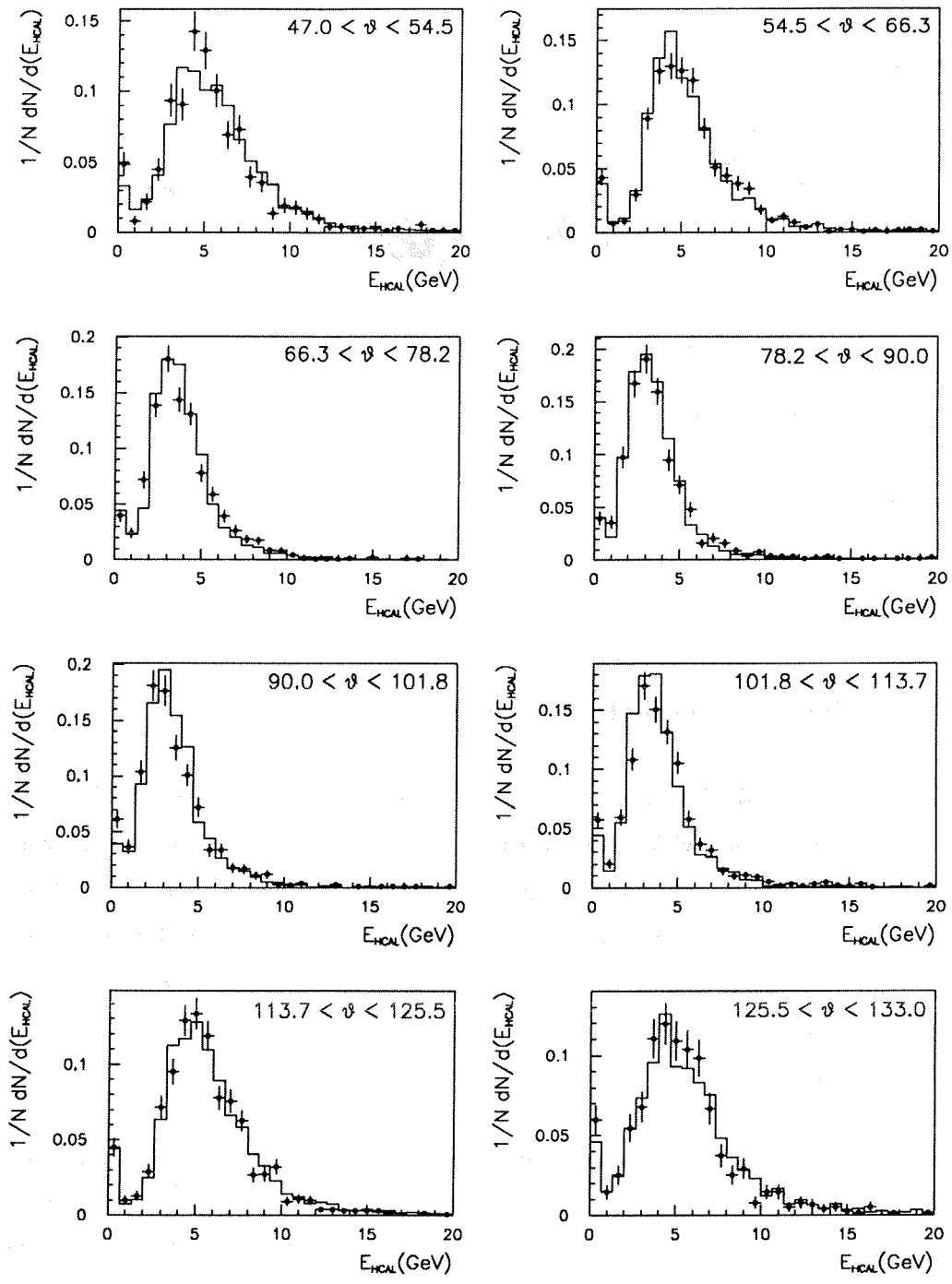

Figure 5.15: *Total HCAL energy deposited for dimuons selected from data and simulation as a function of θ corresponding to HCAL hyerptowers.*

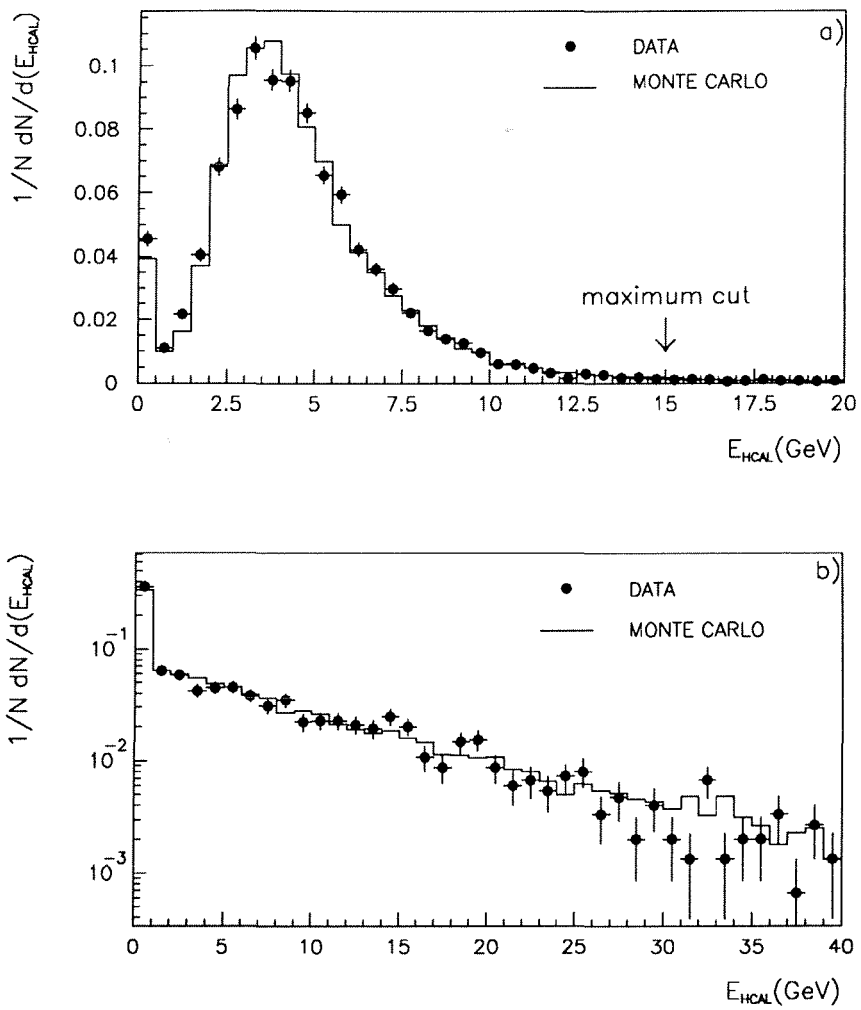

Figure 5.16: *Total HCAL energy deposited by a) dimuons selected from data and simulated* $e^+e^- \rightarrow \mu^+\mu^-$ *events and by b) pions selected from data and simulated* $e^+e^- \rightarrow \tau^+\tau^-$ *events.*

5.2.7 θ variation of *candidate* requirement

The efficiencies of the cut in the total HCAL energy and the *candidate* requirement are shown in Figure 5.17 for dimuon events selected in data compared with dimuons selected from simulation as a function of the θ divisions used when correcting the HCAL energy distributions for simulated muons. There is a loss in efficiency of around 2 % in data compared with simulation for the *candidate* requirement in the regions $47^o < \theta < 54.5^o$ and $125.5^o < \theta < 133^o$ which include the dead zones of the muon chambers and the fourth layer of the HCAL. This loss is corrected for in simulation to obtain better agreement with data.

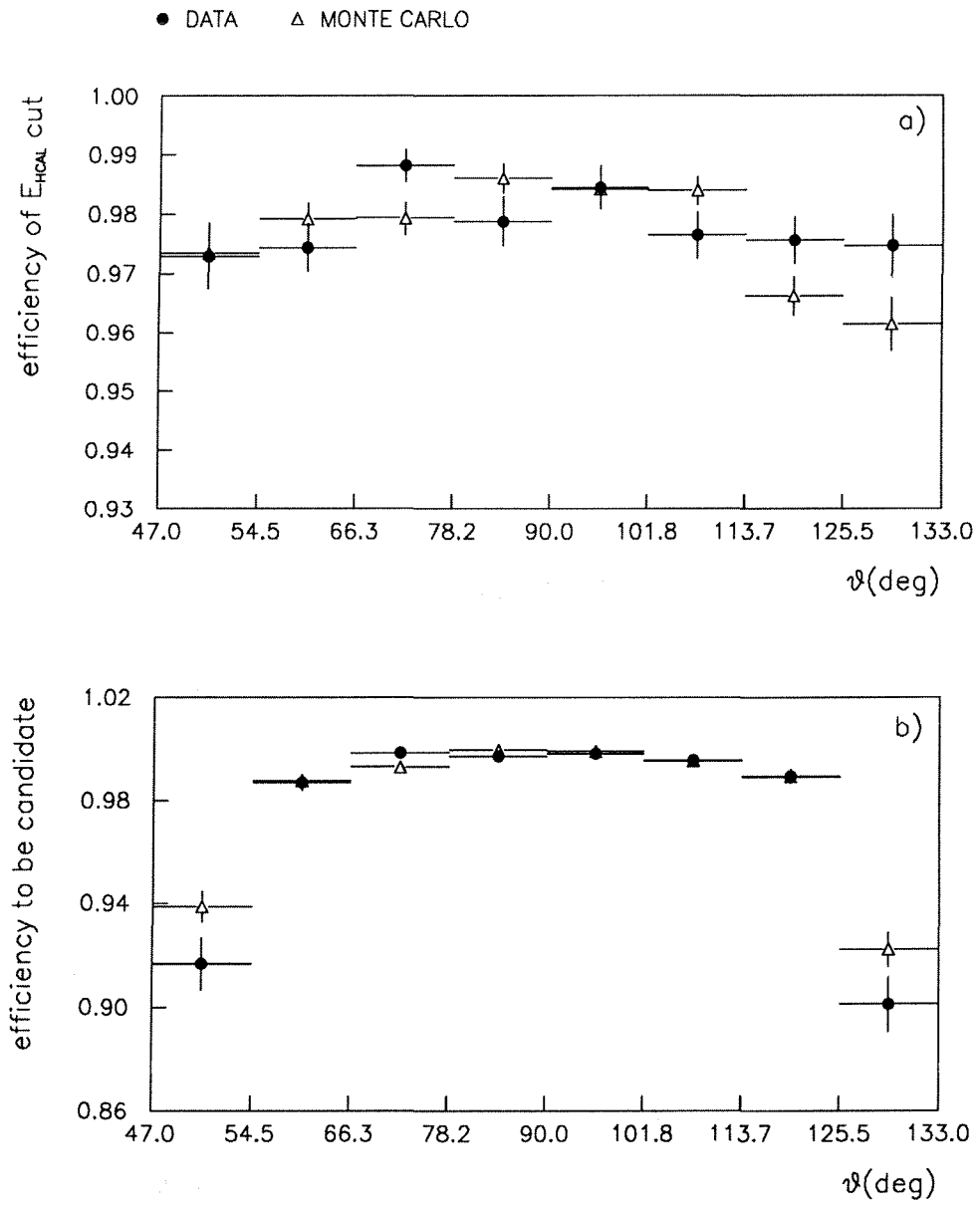

Figure 5.17: *Efficiency of a) cut in E_{HCAL} for dimuons selected in data and in simulation, and of b) the* candidate *selection criteria as a function of θ. The θ divisions correspond to hypertower divisions in the HCAL, according to which HCAL energy distributions were corrected in simulation.*

5.2.8 Momentum dependence of muon identification criteria

candidate requirement

The high momentum end of the spectrum is checked by comparing the dimuons selected from data with simulated dimuons selected in the same way. The efficiency of the *candidate* requirement after correction in simulation for the outermost θ bins was found to be 97.95 $\pm$ 0.15 % for dimuons selected in data, and 97.80 $\pm$ 0.11 % for dimuons selected in simulation. The efficiency obtained for simulated $\tau^- \rightarrow \mu^- \bar{\nu}_\mu \nu_\tau$ decays over the full momentum range was 98.03 $\pm$ 0.14 %.

The low momentum end cannot be checked as definitively, as the two photon events selected from data have a different θ dependence to $\tau^- \rightarrow \mu^- \bar{\nu}_\mu \nu_\tau$ decays, and are of much lower statistics. The momenta of tracks selected as *candidates* (requiring that the other track not be a *candidate* to eliminate external background sources) around the threshold is shown in Figure 5.18 for data and all decays in simulated $e^+e^- \rightarrow \tau^+\tau^-$ events. From this, it can be seen that there is agreement in the region of the cut and that it is well away from the threshold value of about 1.8 GeV. Therefore, the efficiency of the *candidate* requirement is assumed to agree at low momentum. A correction factor of 1.0015 $\pm$ 0.0019 for simulation is assumed from the dimuon differences.

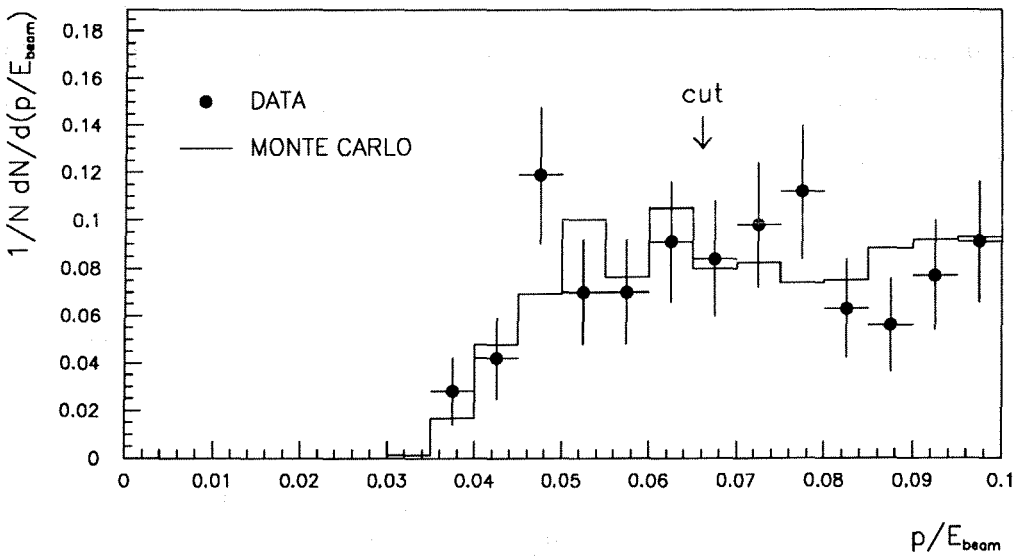

Figure 5.18: *Momentum as a function of beam energy for candidate tracks (with opposite track required not to be a candidate) for data and simulated* $e^+e^- \rightarrow \tau^+\tau^-$ *events.*

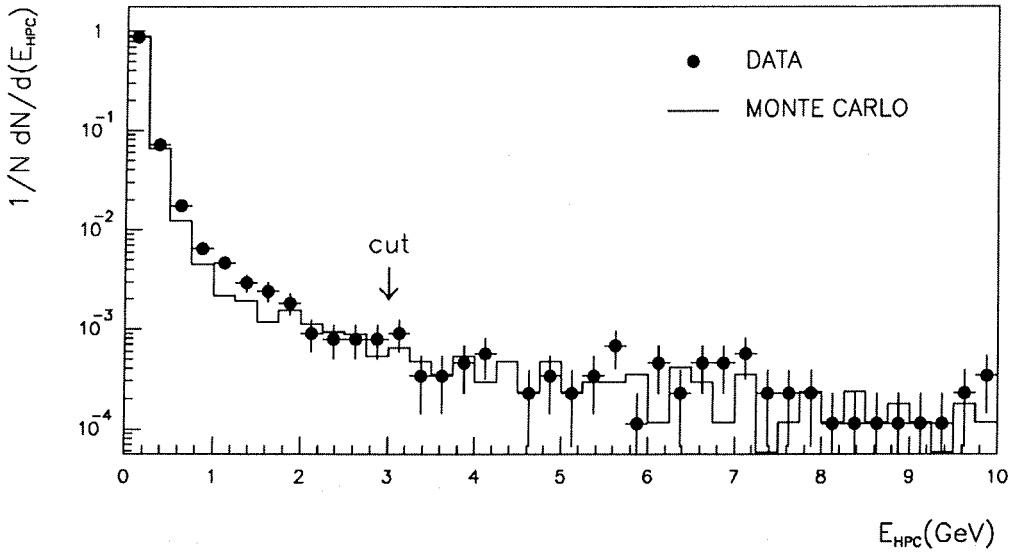

Figure 5.19: *HPC energy associated to track in dimuon events selected in data and simulation.*

Momentum dependence of E_{HPC} cut

The effect of the HPC total energy cut at 3 GeV on the sample of dimuons obtained from data is compared with the effect on a sample of simulated dimuons (see Figure 5.19). The sample of two photon events gives a low momentum efficiency of 100 %, consistent with that expected from Monte Carlo, although the sample is of low statistics. Thus, a flat efficiency can be assumed for data as well as Monte Carlo. A correction of 0.998 $\pm$ 0.002 is applied to the identification efficiency in simulation for the difference seen between data and simulated dimuons.

Momentum dependence of E_{HCAL} and E_γ cuts

The total gamma energy in a 30° cone around the track is shown in Figure 5.20 for tracks which have been identified as *candidates*, and requiring the track in the opposite hemisphere not to be a *candidate* (again, this condition eliminates external backgrounds). The region of low photon energy up to around 0.2 GeV is not well described by simulation which is optimistic concerning photon detection at these energies. However, the cut is situated well away from this region.

The subsample of $\tau^- \to \mu^- \bar{\nu}_\mu \nu_\tau$ decays selected as described in Section 5.2.3 is studied as a function of momentum. The data is corrected for the background due to hadronic

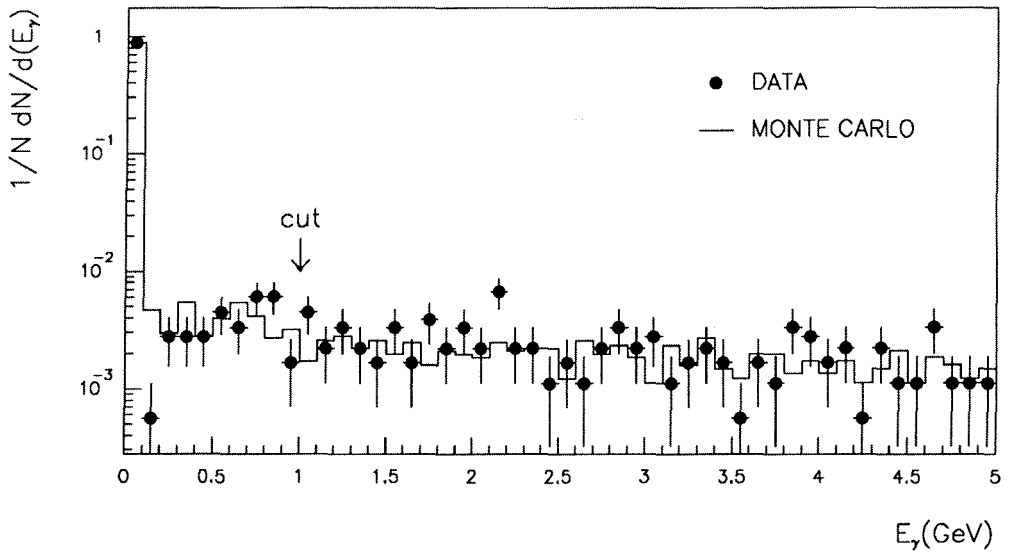

Figure 5.20: *Gamma energy in 30° cone around track satisfying the candidate requirement for data and simulated $e^+e^- \rightarrow \tau^+\tau^-$ events. Background from other sources is suppressed by asking that the leading track in the opposite hemisphere not be a candidate.*

decays of the tau as given by simulation,[1] and the efficiencies of the cuts in E_{HCAL} and E_γ compared with that given for simulated $\tau^- \rightarrow \mu^-\bar{\nu}_\mu\nu_\tau$ decays. The results of this comparison are shown in Table 5.4. The sample of two photon events selected from data gives a further cross check on the efficiency of the E_{HCAL} cut in the momentum bin up to $0.1E_{beam}$, giving an efficiency of 100 %. Although the statistics are somewhat low, there being an average of around 100 events per bin in data, it is possible to deduce an overall correction factor to the efficiencies. No obvious trends in the differences between data and simulation are observed at the present level of statistical uncertainty, and it is assumed that each bin gives a correction independent of the others. The overall correction factor for the cut in E_{HCAL} is found to be 1.0075 ± 0.0051, and 0.9988 ± 0.0058 for the cut in E_γ.

5.2.9 Internal background

The internal background to the $\tau^- \rightarrow \mu^-\bar{\nu}_\mu\nu_\tau$ decay channel is that coming from the other decay modes of the tau, mainly the $\tau^- \rightarrow \pi^-\nu_\tau$ mode. The amount of pion

[1]The excess punchthrough found in data compared to simulation as described in Section 5.2.9 is not seen to hold for the requirement of 3 or more muon hits [72].

Momentum (x E_{beam})	Efficiency of E_{HCAL} cut		Efficiency of E_γ cut	
	Data	Monte Carlo	Data	Monte Carlo
0.0 – 0.1	$100.0\ ^{+0.0}_{-2.7}$	$100.0\ ^{+0.0}_{-0.4}$	94.6 ± 3.7	97.1 ± 0.8
0.1 – 0.2	99.3 ± 0.7	99.1 ± 0.3	97.2 ± 1.4	98.0 ± 0.4
0.2 – 0.3	$100.0\ ^{+0.0}_{-0.7}$	98.7 ± 0.3	97.1 ± 1.4	97.8 ± 0.4
0.3 – 0.4	99.3 ± 0.7	98.2 ± 0.4	98.5 ± 1.0	97.8 ± 0.4
0.4 – 0.5	96.2 ± 1.9	97.2 ± 0.5	98.0 ± 1.3	97.9 ± 0.4
0.5 – 0.6	$100.0\ ^{+0.0}_{-1.1}$	96.8 ± 0.6	$100.0\ ^{+0.0}_{-1.1}$	98.4 ± 0.4
0.6 – 0.8	97.4 ± 1.5	97.0 ± 0.5	97.4 ± 1.5	98.8 ± 0.3

Table 5.4: *Percentage of* $\tau^- \rightarrow \mu^- \bar{\nu}_\mu \nu_\tau$ *decays selected in the intermediate momentum range passing the cuts in* E_{HCAL} *and* E_γ *compared with simulated* $\tau^- \rightarrow \mu^- \bar{\nu}_\mu \nu_\tau$ *decays selected identically.*

punchthrough in simulation is compared to that for data using the pion sample which has been selected to obtain the correction factors required. Table 5.5 shows the fraction of pions passing relevant identification criteria.

There is a very strong correlation between the total energy deposited by the pion in the HCAL and whether it is selected as a muon *candidate* – those depositing large amounts of energy are also more likely to reach the muon chambers and the outer layers of the HCAL. So for pions, the efficiency of the *candidate* requirement is to a large extent negated by the cut in E_{HCAL}. The total HCAL energy deposited by pions is relatively well described (see Figure 5.16). However, the overall punchthrough is found to be too low in simulation by around 40 %. This factor is found to be dependent on momentum with a factor 1.8 more pions satisfying the *candidate* requirement in data than in simulation for momenta above $0.1E_{beam}$ and up to around $0.4E_{beam}$, and a factor of around 1.1 disagreement above $0.4E_{beam}$. The overall correction factor to the internal tau background is found to be 1.5 ± 0.2 where the overall uncertainty is due to the bin-by-bin statistical uncertainties on the pion *candidate* efficiency. The total internal background from non-muonic tau decays to the $\tau^- \rightarrow \mu^- \bar{\nu}_\mu \nu_\tau$ channel is estimated to be 2.3 ± 0.3 % for both the linescan and polarisation selections. The contributions to the error are: 0.27 from the uncertainty in the correction factor required, 0.15 from Monte Carlo statistics and 0.13 to cover any possible differences in photon detection efficiency.

Cut	Data	Monte Carlo
E_{HCAL}	77.7 ± 1.1%	76.5 ± 0.4%
E_{HPC}	84.9 ± 0.9%	80.7 ± 0.3%
H3 > 0	19.9 ± 1.0%	15.1 ± 0.3%
H4 > 0	8.0 ± 0.7%	5.4 ± 0.2%
MH > 0	3.1 ± 0.4%	2.4 ± 0.1%
candidate	10.2 ± 0.8%	7.2 ± 0.2%
E_{HPC}, E_{HCAL} and *candidate*	3.6 ± 0.5%	2.4 ± 0.2%

Table 5.5: *Percentage of pions selected in data and in simulated* $e^+e^- \rightarrow \tau^+\tau^-$ *events passing muon identification criteria in the region* $47^o < \theta < 133^o$. *Note that since pion selection involves the presence of a neutral HPC cluster, the cut on gamma energy cannot be studied.*

5.3 External backgrounds

5.3.1 Cosmic background

The cut in $\mid z_1 - z_2 \mid$ described in Section 4.3.3 (corresponding to an event time of ± 220 ns relative to BCO) is tightened to

- $\mid z_1 - z_2 \mid < 2$ cm

(equivalently, an event time of ± 150 ns relative to BCO). The background was estimated in the same way as described for the linescan selection (see Section 4.9.5) and was found to be 0.5 ± 0.3 %.

5.3.2 $e^+e^- \rightarrow e^+e^-\mu^+\mu^-$ background

The background to the $\tau^- \rightarrow \mu^-\bar{\nu}_\mu\nu_\tau$ decay from the two photon process is cut by a further factor of ≈ 0.75 by asking that for events with two tracks,

- $\theta < 15^o$

An estimate to the background is obtained at generator level only by running the two photon Monte Carlo program [70] described in Section 4.4.1 to obtain a cross section for events passing those linescan selection cuts which could affect the background and additionally, the momentum and θ angle requirements for a track to be considered for muon identification (see Table 5.1). The momentum spectrum for the tracks passing

these cuts is assumed to be not very different from reality, as the momenta involved are low and would be measured relatively accurately. Because of the E_{vis} requirement already implemented (see Section 4.4.2) and the low total transverse momentum of two photon events, nearly all the background is found to consist of events where both tracks have $p > 0.066E_{beam}$. The cross section evaluated by the generator is 0.4 ± 0.1 pb for events with both tracks greater than $0.066E_{beam}$ and 0.08 ± 0.04 pb for events with only one track. A factor of 0.94 is included for the efficiency of the identification criteria involving the HPC, HCAL and muon chambers. From the measured luminosity of 9915 nb^{-1} for the 1991 data-taking period, the background obtained is thus 0.5 ± 0.3 %, concentrated at low momenta. A conservative error is assumed due to the uncertainty of detector effects.

5.3.3 $e^+e^- \rightarrow \mu^+\mu^-$ background

The background due to $e^+e^- \rightarrow \mu^+\mu^-$ events should, as far as possible, be eliminated without using very hard momentum cuts, in order to minimise any biases of the measurement of the tau polarisation from the momentum spectrum of $\tau^- \rightarrow \mu^-\bar{\nu}_\mu\nu_\tau$ decays. The background to the linescan selection consists of events that have passed the $p_{rad} < 1.0$ cut, and the background to the polarisation selection is higher due to the looser $p_{rad} < 1.2$ cut. Effective suppression of this background involves several stages, which are described below.

TPC ϕ crack cut

A considerable fraction of $e^+e^- \rightarrow \mu^+\mu^-$ background is due to poor momentum reconstruction for tracks which pass through a crack between neighbouring TPC modules. The ϕ cracks occur every 60^o at $\phi = 30^o, 90^o, \ldots, 330^o$. For any two track event with a muon *identified*, it is asked that

$$\text{IF} \quad p_1 \text{ or } p_2 > 0.6\ E_{beam}$$

$$\text{THEN} \quad \phi_1 \text{ and } \phi_2 > 1^o \text{ from TPC } \phi \text{ crack}$$

(see Figure 5.21).

Cuts on $\mu_{IDED} - \mu_{CAND}$ events

Further cuts in momentum and p_{rad} are made to reduce the $e^+e^- \rightarrow \mu^+\mu^-$ background, but their effect on the $\tau^- \rightarrow \mu^-\bar{\nu}_\mu\nu_\tau$ sample is minimised by applying them only to

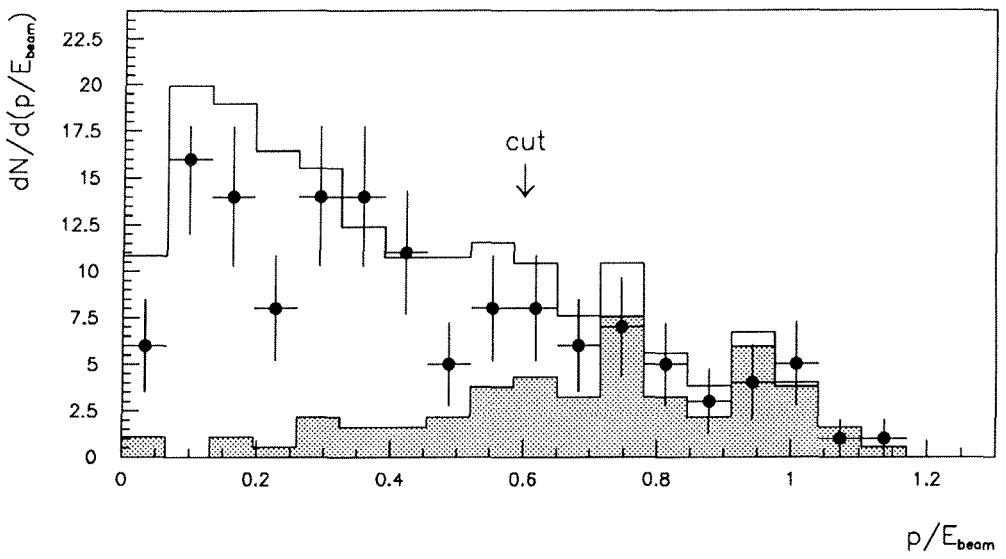

Figure 5.21: *Momentum distribution of 1 v 1 events with at least one identified muon and one track within 1° of a TPC ϕ crack. The dots represent data and the solid line simulated $e^+e^- \rightarrow \tau^+\tau^-$ and $e^+e^- \rightarrow \mu^+\mu^-$ events (with the contribution due to $e^+e^- \rightarrow \mu^+\mu^-$ events hatched).*

events which are likely to be dimuons. These are selected to be events where an isolated track has been *identified* as a muon (is a μ_{IDED}) and the leading track in the opposite hemisphere is a muon *candidate* (a μ_{CAND}). With this requirement, almost 100 % of dimuons are selected, but only a fraction of the $\tau^- \rightarrow \mu^- \bar{\nu}_\mu \nu_\tau$ sample, mainly those in events which have a second muon decay or a punchthrough pion decay in the opposite hemisphere. The first cut which is applied to $\mu_{IDED} - \mu_{CAND}$ type events is a tighter p_{rad} cut:

- $p_{rad} < 0.95$

(see Figure 5.22).

The majority of dimuon events surviving after the cuts so far are found to be events in which a track is of low momentum due to radiation of a relatively hard photon, and therefore, the event is able to pass the p_{rad} cut. However, provided the photon showers in the HPC, its energy can be added to the momentum of the track and this should be once again close to beam energy. The track will not of course be *identified* as a muon because it would fail the cut on E_γ but it would probably satisfy the *candidate* requirement.

A second cut is also applied to $\mu_{IDED} - \mu_{CAND}$ events with only two tracks. It is required that

- $p_{\mu_{IDED}} < 0.7E_{beam}$ $\quad OR$
- $(p + E_{CONE})_{\mu_{CAND}} < 0.7E_{beam}$

(see Figure 5.22).

After these cuts, the remaining dimuon background is mainly attributable to the imperfect *candidate* selection efficiency.

From Figure 5.22, it is seen that there is a slight excess in data around the region of the dimuon peak. The background obtained from simulation is corrected by a factor of 1.3 $\pm$ 0.3 which corresponds to the difference. The background for the linescan selection is 0.3 $\pm$ 0.1 % and 0.8 $\pm$ 0.3 % for the polarisation selection, and is concentrated at high momentum. The momentum corrections which have been applied as described in Section 4.7.1 to the simulation change the distribution of the background, but the effect on the overall amount is negligible.

The internal and external backgrounds to the $\tau^- \rightarrow \mu^- \bar{\nu}_\mu \nu_\tau$ selection are summarised in Table 5.6.

Background type	Amount
Tau internal	2.3 $\pm$ 0.3 %
Cosmic rays	0.5 $\pm$ 0.3 %
$e^+e^- \rightarrow e^+e^-\mu^+\mu^-$	0.5 $\pm$ 0.3 %
$e^+e^- \rightarrow \mu^+\mu^-$ (linescan)	0.3 $\pm$ 0.1 %
$e^+e^- \rightarrow \mu^+\mu^-$ (polarisation)	0.8 $\pm$ 0.3 %
Total (linescan)	3.6 $\pm$ 0.5 %

Table 5.6: *Background contributions to the* $\tau^- \rightarrow \mu^- \bar{\nu}_\mu \nu_\tau$ *decay channel.*

5.4 Systematics on the muon selection efficiency

The uncertainties on the correction factors estimated to be required for simulation regarding the muon identification criteria (Table 5.1) are a source of systematic bias. In addition, other possible sources of systematic uncertainties are investigated by varying

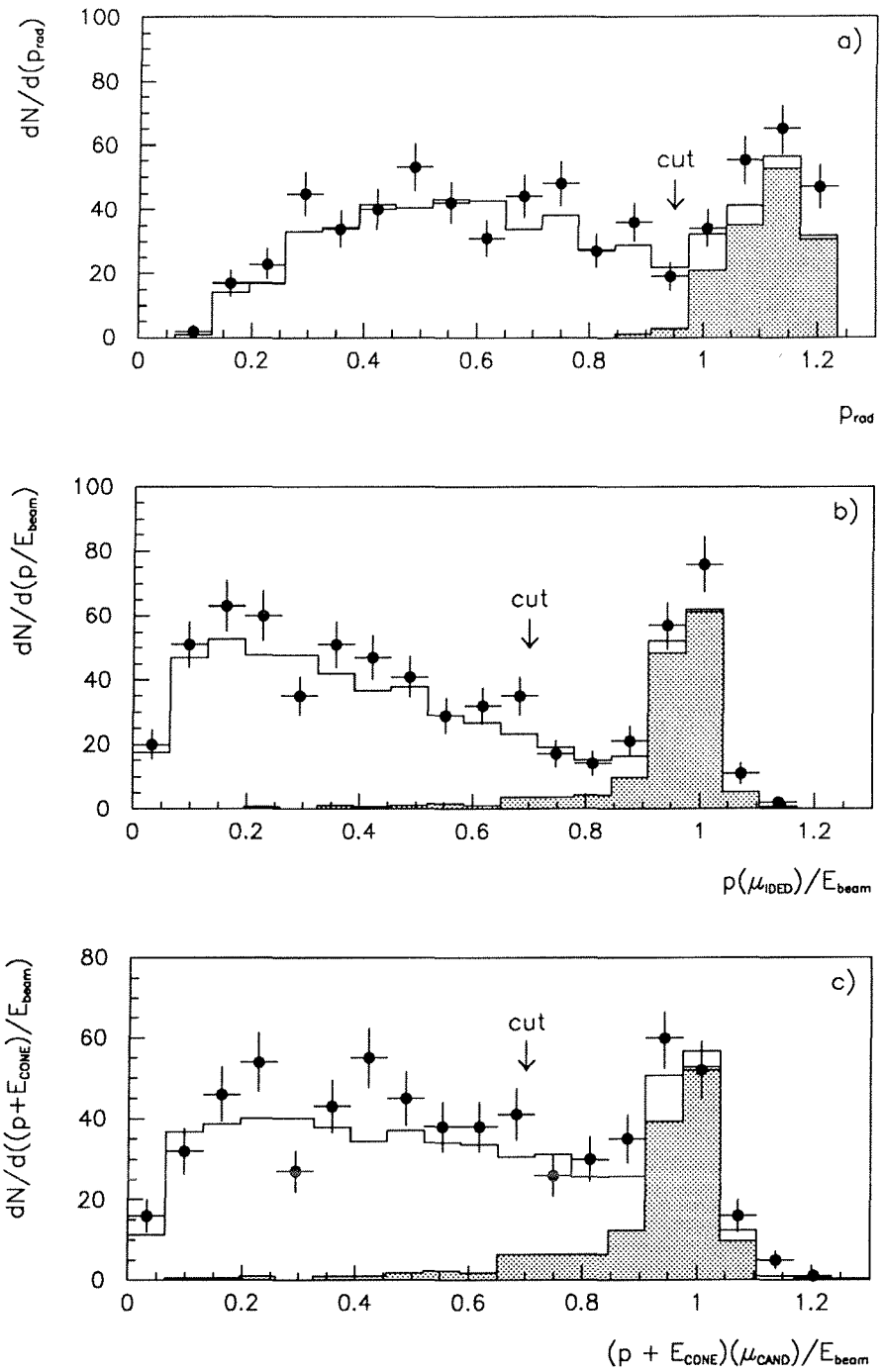

Figure 5.22: *Plots for $\mu_{IDED}-\mu_{CAND}$ events in data (dots) and in Monte Carlo $e^+e^- \rightarrow \tau^+\tau^-$ and $e^+e^- \rightarrow \mu^+\mu^-$ events (line, shaded portion $e^+e^- \rightarrow \mu^+\mu^-$ contribution). a) p_{rad} for the event, with the cut placed at $p_{rad} < 0.95$. b) p as a function of E_{beam} for μ_{IDED}, and c) $p + E_{CONE}$ as function of E_{beam} for μ_{CAND}, before the p_{rad} cut. The cuts in b) and c) are made simultaneously on the event after the p_{rad} cut.*

the other cuts used to select $\tau^- \to \mu^- \bar{\nu}_\mu \nu_\tau$ decays. The variation of the cut values is not necessarily symmetric as the cut may be near the edge of a distribution.

Minimum momentum requirement

The cut at $p > 0.066 E_{beam}$ is brought down to $p > 0.055 E_{beam}$ which is approximately halfway between the original cut value and the threshold for identification as a muon (see Figure 5.18), and raised to $0.088 E_{beam}$. All backgrounds were re-evaluated. Within statistical fluctuations, differences between simulation and data were compatible.

Isolated track requirement

The requirement that an identified $\tau^- \to \mu^- \bar{\nu}_\mu \nu_\tau$ decay have only one track in the hemisphere can lead to differences between simulation and data if for instance the rate of photon conversions or the tracking peculiarities of the TPC in splitting a single track into two are not well described in simulation. The events having a hemisphere flagged in data as a $\tau^- \to \mu^- \bar{\nu}_\mu \nu_\tau$ decay with more than one charged track were scanned visually. If there were microvertex hits for more than one track, it was assumed to be an a_1 decay, as the probability for a photon to convert in the beam pipe is very low. The other decays were found to be consistent with a $\tau^- \to \mu^- \bar{\nu}_\mu \nu_\tau \gamma$ decay where the photon converted, or a $\tau^- \to \mu^- \bar{\nu}_\mu \nu_\tau$ decay with misreconstruction of a single track as two tracks.

A correction factor of 1.0042 ± 0.0042 was assumed from the difference between simulation and data in the number of $\tau^- \to \mu^- \bar{\nu}_\mu \nu_\tau$ decays found with more than one track.

$| z_1 - z_2 |$ cut

The requirement that $| z_1 - z_2 | < 2$ cm was varied by $\pm$ 1 cm, and the corresponding cosmic background re-evaluated using the method described in Section 4.9.5. A systematic uncertainty of $\Delta\varepsilon/\varepsilon = 0.35$ % was estimated from differences observed between data and simulation.

Pion punchthrough

The uncertainty in the momentum dependent factors applied to correct the probability of observing a hadronic *candidate* contributes an uncertainty to the muon selection effi-

ciency via the cuts used to reject dimuons. The uncertainty is small, as little correction was needed for the high momentum end of the hadronic decays, and is conservatively estimated to be $\Delta\varepsilon/\varepsilon = 0.17$ %.

Dimuon rejection cuts

The cut values used in the rejection of dimuon events are strongly correlated since they all involve momentum. The momentum cut used in the TPC ϕ crack cut of $0.6E_{beam}$ is varied by $\pm$ $0.1E_{beam}$. The differences observed between data and simulation were compatible with the statistical uncertainties expected.

The other cuts are specifically applied to $\mu_{IDED} - \mu_{CAND}$ events over the whole ϕ range, and are assumed to be relatively independent of the TPC ϕ crack cut. The cut values used are moved either higher or lower simultaneously as follows:

- p_{rad} at 0.95 by $\pm$ $0.05E_{beam}$
- For μ_{IDED}, p at $0.7E_{beam}$ by $\pm$ $0.1E_{beam}$
- For μ_{CAND}, $(p + E_{CONE})$ at $0.7E_{beam}$ by $\pm$ $0.1E_{beam}$

The dimuon background was re-evaluated with the altered cuts. Within expected statistical variations, no changes were observed between data and simulation.

Acollinearity cut at 15°

This cut, which was introduced to reduce the background from two photon events (Section 5.3.2), is varied by $\pm$ 2°. Within expected variations, no systematic effects were observed.

5.5 Efficiency of $\tau^- \rightarrow \mu^-\bar{\nu}_\mu\nu_\tau$ selection

The efficiency as estimated from simulation of selecting $\tau^- \rightarrow \mu^-\bar{\nu}_\mu\nu_\tau$ decays from the full solid angle is found to be 39.44 $\pm$ 0.26 % (uncertainty due to Monte Carlo statistics). This efficiency must be corrected by the following factors obtained from data:

- Linescan selection correction factors (see Section 4.7). The correction required due to the momentum distribution differences is found to be the same for $\tau^- \rightarrow \mu^-\bar{\nu}_\mu\nu_\tau$ decays. However, no correction is found necessary in the case

of electromagnetic energy differences, as the $\tau^- \rightarrow \mu^- \bar{\nu}_\mu \nu_\tau$ channel does not leave large deposits of charged or neutral energy in the HPC in general.

Losses of events due to a track passing through a ϕ crack in the TPC would be independent of particle type and therefore lead to an approximately equal loss of $\tau^- \rightarrow \mu^- \bar{\nu}_\mu \nu_\tau$ decays[2]. The same argument applies to losses of events due to the leading track failing the r impact parameter cut because of bad tracking. In a 1 v N event where the leading track in the N side fails the r cut because it is from a photon conversion, the event is lost, but here again, there is no bias in the decay type of the 1 prong. A greater proportion of N v N tau events are thrown away with the r cut (i.e. these cuts are somewhat topology dependent) but since these are at the few percent level overall, biases are low. Therefore, one can assume the same correction factors due to differences between data and simulation concerning TPC ϕ crack and r impact parameter distributions. The overall correction factor from the above differences is estimated to be 0.991 $\pm$ 0.006.

- Efficiency of E_{HPC} cut – 0.998 $\pm$ 0.002.
- Efficiency of *candidate* requirement – 1.0015 $\pm$ 0.0019.
- Efficiency of E_{HCAL} cut – 1.0075 $\pm$ 0.0051.
- Efficiency of E_γ cut – 0.9988 $\pm$ 0.0058.
- Requirement of isolated track – 1.0042 $\pm$ 0.0042.

The systematic uncertainties estimated on the $e^+e^- \rightarrow \tau^+\tau^-$ selection efficiency from the placement of the linescan selection cuts are assumed to apply equally to the $\tau^- \rightarrow \mu^- \bar{\nu}_\mu \nu_\tau$ selection efficiency, except for the effect of the cut in E_{rad}. The uncertainties are listed in Table 5.7.

After these corrections, the efficiency for $\tau^- \rightarrow \mu^- \bar{\nu}_\mu \nu_\tau$ selection over 4π is found to be 39.48 $\pm$ 0.54 %.

---

[2]For the overall $\tau^- \rightarrow \mu^- \bar{\nu}_\mu \nu_\tau$ selection one can ignore any effects on the correction factor from dimuon rejection cuts involving TPC ϕ crack cuts (see Section 5.3.3) as negligible since they are applied to around 20 % of the sample only.

Systematic source	$\Delta\varepsilon/\varepsilon$
TPC ϕ cracks correction	0.3 %
p_{rad} correction	0.2 %
r impact parameter correction	0.5 %
acollinearity	0.2 %
isolation angle	0.1 %
isolated track	0.4 %
E_{HPC} cut	0.2 %
candidate	0.2 %
E_{HCAL} cut	0.5 %
E_{γ} cut	0.6 %
pion punchthrough correction	0.2 %
$\mid z_1 - z_2 \mid$ cut	0.4 %
MC statistics	0.7 %
Total	1.4 %

Table 5.7: *Systematic uncertainties on the selection efficiency for* $\tau^- \rightarrow \mu^- \bar{\nu}_\mu \nu_\tau$ *decays.*

The efficiency relative to the linescan selection is 69.5 $\pm$ 1.0 %, where the main losses are due to the exclusion of the regions $43^o < \theta < 47^o$ and $133^o < \theta < 137^o$, the momentum cut at $p > 0.066 E_{beam}$ and the other identification criteria of Table 5.1.

Within the fiducial region of θ acceptance (also excluding the 90^o hole) and requiring that $p > 0.066 E_{beam}$, the efficiency relative to the linescan selection is around 90 %.

The $\tau^- \rightarrow \mu^- \bar{\nu}_\mu \nu_\tau$ proportion in the tau linescan selection is enhanced by a factor 1.056 compared to the original proportion due to biases of the selection criteria.

In the 1991 data set, **1613** muons were selected for the branching ratio study, and **1644** for the polarisation measurement.

Chapter 6

Branching ratio results

6.1 Measurement of $Br(\tau^- \rightarrow \mu^- \bar{\nu}_\mu \nu_\tau)$

The branching ratio for the decay $\tau^- \rightarrow \mu^- \bar{\nu}_\mu \nu_\tau$ can be determined according to the following equation:

$$Br(\tau^- \rightarrow \mu^- \bar{\nu}_\mu \nu_\tau) = \frac{N_\mu(1-b_\mu)/(\varepsilon_\mu c_\mu)}{N_\tau(1-b_\tau)/(\varepsilon_\tau c_\tau)} \tag{6.1}$$

where

- N_μ = number of $\tau^- \rightarrow \mu^- \bar{\nu}_\mu \nu_\tau$ decays selected
- b_μ = fractional background in the $\tau^- \rightarrow \mu^- \bar{\nu}_\mu \nu_\tau$ decay sample
- ε_μ = Monte Carlo efficiency to select $\tau^- \rightarrow \mu^- \bar{\nu}_\mu \nu_\tau$ decays in 4π.
- c_μ = correction factors required for ε_μ as found from data
- N_τ = number of $e^+e^- \rightarrow \tau^+\tau^-$ decays selected x 2
- b_τ = fractional background in the $e^+e^- \rightarrow \tau^+\tau^-$ decay sample
- ε_τ = Monte Carlo efficiency to select $e^+e^- \rightarrow \tau^+\tau^-$ decays in 4π.
- c_τ = correction factors required for ε_τ as found from data.

The correction factors for ε_τ are the linescan selection correction factors due to the differences seen between data and simulation for momentum, electromagnetic energy, TPC ϕ crack and r impact parameter distributions. Their estimation is described in Section 4.7.

The correction factors for ε_μ also include the linescan correction factors, not necessarily of the same magnitude. They are discussed in Section 5.5, and are the same for $\tau^- \to \mu^- \bar{\nu}_\mu \nu_\tau$ decays, except that no electromagnetic energy correction is required. In addition, there are the correction factors arising specifically from the $\tau^- \to \mu^- \bar{\nu}_\mu \nu_\tau$ selection criteria. The main corrections are due to differences between data and simulation for the efficiency of the E_{HCAL} cut, and from requiring an isolated track.

In this calculation, ε_μ and ε_τ as given below are found from simulated $e^+e^- \to \tau^+\tau^-$ events with the corrections required for momentum and HPC cone energy to obtain agreement with data (see Sections 4.7.1 and 4.7.2) already included. The additional correction factors due to the inefficiencies of the TPC ϕ cracks and the losses from the cut in r impact parameter are the same for the $\tau^- \to \mu^- \bar{\nu}_\mu \nu_\tau$ and $e^+e^- \to \tau^+\tau^-$ selections and will cancel out in the calculation of the branching ratio. Hence, they do not need to be considered further. Therefore, the only correction factors to take into account in the calculation are those specific to the $\tau^- \to \mu^- \bar{\nu}_\mu \nu_\tau$ channel, as given in Section 5.5. The overall correction factor to be applied to ε_μ is found to be

$$c_\mu = 1.0100 \pm 0.0092 \tag{6.2}$$

where the overall uncertainty is obtained by adding the individual uncertainties in quadrature.

If one considers an uncertainty on an efficiency due to a systematic effect given by $\alpha = \Delta\varepsilon/\varepsilon$, then if it has the same magnitude for efficiencies ε_1 and ε_2, we find that

$$\frac{\varepsilon_1 + \Delta\varepsilon_1}{\varepsilon_2 + \Delta\varepsilon_2} = \frac{\varepsilon_1 + \alpha\varepsilon_1}{\varepsilon_2 + \alpha\varepsilon_2} = \frac{\varepsilon_1}{\varepsilon_2} \tag{6.3}$$

i.e., any systematic effects common to ε_τ and ε_μ will cancel out in the calculation of the branching ratio, and thus the uncertainties due to these systematics do not need to be considered. Thus, in addition to the Monte Carlo statistical uncertainty of 0.16 % (absolute) ε_τ has an additional systematic uncertainty of $\Delta\varepsilon/\varepsilon = 0.35$ % from the cut in E_{rad}, which would not affect the $\tau^- \to \mu^- \bar{\nu}_\mu \nu_\tau$ selection in the same way. For ε_μ, the Monte Carlo statistical uncertainty of 0.26 % is to be combined with additional systematic uncertainties in the $\tau^- \to \mu^- \bar{\nu}_\mu \nu_\tau$ selection which are not accounted for in c_μ, i.e.,with $\Delta\varepsilon/\varepsilon = 0.17$ % from the pion punchthrough correction and $\Delta\varepsilon/\varepsilon = 0.35$ % from the $\mid z_1 - z_2 \mid$ cut at 2 cm.

The numbers used for the branching ratio calculation are given in Table 6.1.

N_μ	b_μ	c_μ	ε_μ
1613	3.6 ± 0.5 %	1.0100 ± 0.0092	0.3952 ± 0.0030
N_τ	b_τ	c_τ	ε_τ
2 x 6129	2.8 ± 0.6 %	–	0.5378 ± 0.0025

Table 6.1: *Numbers used in calculation of* $Br(\tau^- \to \mu^- \bar{\nu}_\mu \nu_\tau)$.

The branching ratio is measured to be

$$\boxed{Br(\tau^- \to \mu^- \bar{\nu}_\mu \nu_\tau) = 17.58 \pm 0.41 \text{ (stat)} \pm 0.27 \text{ (syst)} \%} \tag{6.4}$$

The main contributions to the systematic uncertainty are given in Table 6.2.

6.2 Tests of universality

The branching ratio measured above can be used to test the hypothesis of universal lepton couplings to the W boson. Two relations have been given in Section 2.1:

$$\frac{Br(\tau^- \to \mu^- \bar{\nu}_\mu \nu_\tau)}{Br(\tau^- \to e^- \bar{\nu}_e \nu_\tau)} = 0.9726 \left(\frac{g_\mu}{g_e}\right)^2 \tag{2.8}$$

which predicts the ratio of the electron and muon branching fractions of the tau in terms of the effective coupling constants g_e and g_μ, and

$$Br(\tau^- \to \mu^- \bar{\nu}_\mu \nu_\tau) = 0.9730 \frac{\tau_\tau}{\tau_\mu} \left(\frac{m_\tau}{m_\mu}\right)^5 \left(\frac{g_\tau}{g_e}\right)^2 \tag{2.14}$$

which provides a connection between tau and muon decay in terms of g_e and g_τ.

Using the following value for the electron branching ratio [77]:

$$Br(\tau^- \to e^- \bar{\nu}_e \nu_\tau) = 17.76 \pm 0.16 \ \% \tag{6.5}$$

the ratio of the effective weak coupling constants at the μ–W–$\bar{\nu}_\mu$ and e–W–$\bar{\nu}_e$ vertices is deduced to be:

$$\left(\frac{g_\mu}{g_e}\right)^2 = 1.018 \pm 0.028 \tag{6.6}$$

Using the following values for the muon mass [9], tau mass [24], muon lifetime [9] and tau lifetime [76]:

$$m_\mu = 105.658 \text{ MeV/c}^2 \tag{2.5}$$

$$m_\tau = 1776.9^{+0.4}_{-0.5} \text{ MeV/c}^2 \tag{2.6}$$

$$\tau_\mu = 2.19703 \pm 0.00004 \ \mu s \tag{6.7}$$

$$\tau_\tau = 295.7 \pm 3.2 \text{ fs} \tag{6.8}$$

the ratio of the effective weak coupling constants at the τ–W–$\bar{\nu}_\tau$ and e–W–$\bar{\nu}_e$ vertices is deduced to be:

$$\left(\frac{g_\tau}{g_e}\right)^2 = 0.998 \pm 0.030 \tag{6.9}$$

These values are consistent with universal effective weak couplings in the lepton generations, as expected in the Standard Model. In both cases, the errors are dominated by the uncertainty on $Br(\tau^- \to \mu^- \bar{\nu}_\mu \nu_\tau)$.

SOURCE	$\Delta[Br(\tau^- \to \mu^- \bar{\nu}_\mu \nu_\tau)]$
Isolated track requirement	0.07
E_γ cut uncertainty	0.10
E_{HCAL} cut uncertainty	0.09
$\mid z_1 - z_2 \mid$ cut	0.06
MC statistical uncertainty on ε_μ	0.12
Tau internal background	0.05
External backgrounds in $\tau^- \to \mu^- \bar{\nu}_\mu \nu_\tau$ selection	0.07
E_{rad} cut uncertainty	0.06
MC statistical uncertainty on ε_τ	0.05
$e^+e^- \to e^+e^-$ background in $e^+e^- \to \tau^+\tau^-$ sample	0.07
TOTAL	0.27

Table 6.2: *Main systematic uncertainties on* $Br(\tau^- \to \mu^- \bar{\nu}_\mu \nu_\tau)$.

Chapter 7

Polarisation results

7.1 Measurement of A_{pol}

7.1.1 Fit procedure

The measured momentum spectrum of the $\tau^- \to \mu^- \bar{\nu}_\mu \nu_\tau$[1] decays selected is used to find the average tau polarisation. The bin width used is $0.1E_{beam}$. The backgrounds from $e^+e^- \to \mu^+\mu^-$ events, $e^+e^- \to e^+e^-\mu^+\mu^-$ events, cosmics and non-muonic tau decays are subtracted according to the proportions expected per bin. This gives the number of events in the data to be fitted per bin i as

$$n_i = N_i - b_i \tag{7.1}$$

where N_i is the original number observed in bin i and b_i is the total background expected in bin i. The uncertainty on n_i is given by

$$\sigma_{n_i}^2 = N_i + \sigma_{b_i}^2 \tag{7.2}$$

with σ_{b_i} the uncertainty on b_i. Only the first nine bins are used in the fit, as the dimuon background in the last bin is of the same magnitude as the signal, and is a source of systematic uncertainty. On the other hand, there is no significant loss in sensitivity if the bin is excluded. The overall number of $\tau^- \to \mu^- \bar{\nu}_\mu \nu_\tau$ decays used in the fit after correction for background is 1570.

The helicity of the tau is known in the simulation, and two momentum distributions, m_i^+ and m_i^- (corresponding to P = +1 and P = −1 tau helicities respectively), are

[1]Including the charge conjugate decay mode.

obtained for $\tau^- \rightarrow \mu^- \bar{\nu}_\mu \nu_\tau$ decays which have passed through the same analysis chain as the data. These distributions are each normalised to the total number of (background subtracted) data entries. The simulation distribution used to fit the data is given by

$$f_i = a m_i^+ + (1 - a) m_i^- \tag{7.3}$$

with one free parameter a which is related to the average tau polarisation A'_{pol}[2] by

$$a = \frac{1 + A'_{pol}}{2} \tag{7.4}$$

The best fit to the data is obtained by a least-squares method, which consists of minimising

$$\chi^2 = \sum_i \frac{(n_i - f_i)^2}{\sigma_i^2} \tag{7.5}$$

where σ_i includes the statistical uncertainty on the data as given by Equation 7.2 and the statistical uncertainty on the f_i arising from using a finite Monte Carlo sample in the fit. Some considerations have to be taken into account when fitting for the polarisation:

1. The simulated spectra have to be corrected for the momentum dependent efficiency differences found between data and simulation for the E_{HCAL} and E_γ cuts (see Section 5.2.8). The same correction factors were used for the last three bins due to a lack of statistics in determining individual factors. The effect of the uncertainties on these factors on the polarisation measurement is therefore evaluated separately.

2. The cuts used to select the $\tau^- \rightarrow \mu^- \bar{\nu}_\mu \nu_\tau$ sample, especially cuts involving momentum, can bias the fit in that P = +1 and P = −1 spectra are selected with different efficiencies. This point is explained further below.

Bias of selection cuts

The polarisation to be measured is

$$A_{pol} = \frac{N^+ - N^-}{N^+ + N^-} \tag{7.6}$$

where N^+ is the number of $\tau^- \rightarrow \mu^- \bar{\nu}_\mu \nu_\tau$ decays with P = +1 for the tau and N^- is the number of $\tau^- \rightarrow \mu^- \bar{\nu}_\mu \nu_\tau$ decays with P = −1 for the tau. However, the selection cuts involving for instance rejection of dimuon background cause there to be different

[2]The reason for using the notation A'_{pol} instead of A_{pol} to represent the mean polarisation is explained further on.

efficiencies ε_+ and ε_- for N^+ and N^-. The polarisation that is in fact measured is

$$A'_{pol} = \frac{\varepsilon_+ N^+ - \varepsilon_- N^-}{\varepsilon_+ N^+ + \varepsilon_- N^-} = \frac{N^+ - \frac{\varepsilon_-}{\varepsilon_+} N^-}{N^+ + \frac{\varepsilon_-}{\varepsilon_+} N^-} \tag{7.7}$$

and unless $\varepsilon_+ = \varepsilon_-$, $A_{pol} \neq A'_{pol}$.

From a comparison of simulated $P = +1$ and $P = -1$ muon momentum spectra before and after all cuts, it is found that for this selection of $\tau^- \to \mu^- \bar{\nu}_\mu \nu_\tau$ decays,

$$\frac{\varepsilon_-}{\varepsilon_+} = 1.0487 \pm 0.0108 \tag{7.8}$$

The corrected value for a measured polarisation A'_{pol} is given by

$$A_{pol} = \frac{\left(\frac{\varepsilon_-}{\varepsilon_+} - 1\right) + \left(\frac{\varepsilon_-}{\varepsilon_+} + 1\right) A'_{pol}}{\left(\frac{\varepsilon_-}{\varepsilon_+} + 1\right) + \left(\frac{\varepsilon_-}{\varepsilon_+} - 1\right) A'_{pol}} \tag{7.9}$$

7.1.2 Fit results for A'_{pol}

The χ^2 constructed in Equation 7.5 is minimised using the MINUIT package [73]. The value obtained from the fit for A'_{pol} is

$$A'_{pol} = -0.138 \pm 0.137 \tag{7.10}$$

with a χ^2 per degree of freedom of 1.0, indicating a reasonable fit. The fit result is shown in Figure 7.1, together with the contributions from the P = +1 and P = −1 simulation spectra. The Monte Carlo sample is approximately 9 times the size of the data sample. The momentum spectrum of the background that was subtracted is shown in the shaded histogram.

The uncertainty quoted includes uncertainties from the rates of backgrounds and from finite Monte Carlo statistics. These are separately quantified below.

Background uncertainties

To evaluate the uncertainty from the backgrounds, each source is varied simultaneously by 1 σ in each bin, and the fit reperformed. The change in A'_{pol} that is observed is taken as an estimate of the systematic uncertainty. The total uncertainty arising from backgrounds is estimated to be 0.017, with 0.010 due to the dimuon background, and 0.010 due to the two photon background. These numbers are consistent with the decrease (in quadrature) of the error obtained from performing the fit without including the background uncertainties in the χ^2.

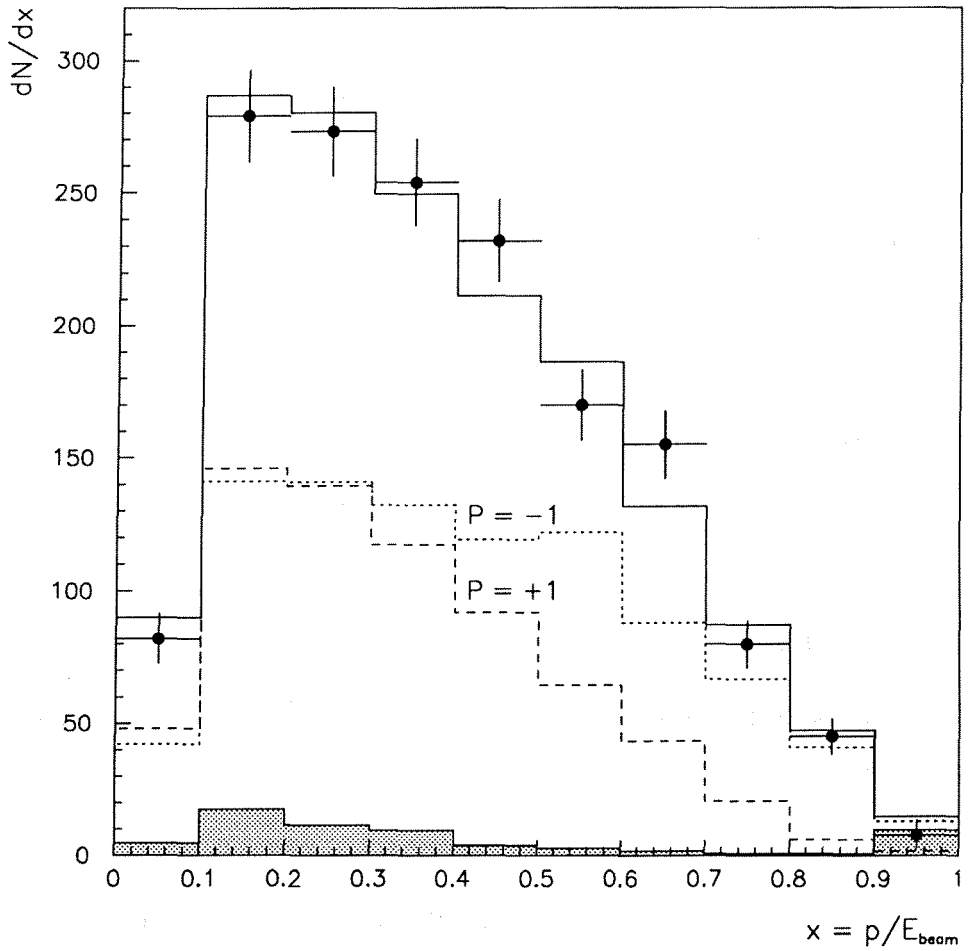

Figure 7.1: *Background subtracted momentum spectrum of* $\tau^- \rightarrow \mu^- \bar{\nu}_\mu \nu_\tau$ *decays used in the average tau polaristion measurement, and contributions of simulation* $P = +1$ *and* $P = -1$ *spectra to the fit. The shaded histogram represents the background spectrum.*

Monte Carlo statistics

The finite sample of simulated helicity P = ±1 decays with which the data is fitted is a source of uncertainty due to the statistical fluctuations in the sample. These are quantified by generating in a random way new Monte Carlo spectra based on the original spectra [74]. The data is then refitted with the new spectra, and the spread in polarisation values obtained is taken as an estimate of the contribution to the uncertainty from Monte Carlo statistics. The root mean square of the spread in values is found to be 0.046. This number is entirely consistent with the decrease observed in the error obtained from performing the fit using the original spectra with the contribution from the Monte Carlo uncertainties excluded in the χ^2.

The uncertainties due to the backgrounds and Monte Carlo statistics are subtracted in quadrature from 0.137 to give an estimate of the statistical uncertainty from the data alone as 0.128.

7.1.3 Systematics on A'_{pol}

Two approaches are used to estimate the size of any systematic effects on the measurement of A'_{pol}. If the effect being investigated is due to a known difference between data and simulation, the shift in A'_{pol} that is observed is taken as a systematic uncertainty. However, to quantify effects due to cuts that may bias the momentum spectrum, the cuts are varied or removed and new distributions m_i^+, m_i^-, n_i and σ_i are found. If the shift in A'_{pol} that is observed is not compatible with the shift expected through the change in $\varepsilon_-/\varepsilon_+$ within statistical fluctuations, then the shift is again taken as a systematic uncertainty.

Momentum distribution differences

The simulation data used in the fit have been corrected for differences in momentum resolution and scale as described in Section 4.7.1 in order to obtain agreement with data. The correction especially affects the high momentum end of the muon spectrum. New distributions m_i^+ and m_i^-, and a new spectrum for the expected dimuon background are generated without applying the corrections and the shift in A'_{pol} is observed. The systematic uncertainty is 0.053.

Pion punchthrough corrections

These refer to the momentum dependent corrections estimated from data for the probability of observing a hadronic *candidate*. They affect the data spectrum through a change in the momentum spectrum of the tau internal background, and also alter the simulation muon spectra because of the dimuon background rejection cuts involving the identification of *candidates*. The scaling factors required were each simultaneously increased by 1 σ. The systematic uncertainty is taken from the shift in A'_{pol} to be 0.016.

Effect of E_γ and E_{HCAL} cuts

Since the correction factors found in Section 5.2.8 for these cuts have only statistical uncertainties arising from the data and simulation, and no obvious correlation across bins is observed, the uncertainties on the different bins can be considered as independent.

The correction factors are varied by 1 σ separately in each bin of the simulation, with the last three bins varied simultaneously as they share the same factors. The changes observed in A'_{pol} were added in quadrature to give an overall systematic uncertainty of 0.040 (0.026 for E_{HCAL} and 0.030 for E_γ).

TPC ϕ crack inefficiencies

The TPC ϕ cracks are less efficient in data than in simulation, as observed in Section 4.7.3. This could introduce a bias through the dimuon rejection cuts which involve cutting out tracks that pass through cracks if they are above $0.6E_{beam}$ (see Section 5.3.3 for exact cuts). An extra 20 % inefficiency is conservatively assumed (see Figure 4.19). on the tracks lost in simulation. The systematic uncertainty is estimated from the shift in A'_{pol} to be 0.009.

Dimuon rejection cuts

The cut values used were varied by the same amounts as for the study of the $\tau^- \rightarrow \mu^-\bar{\nu}_\mu\nu_\tau$ selection efficiency (see Section 5.4), and the shift in A'_{pol} compared with the shift expected. The systematic effect was estimated to be 0.013.

$\mid z_1 - z_2 \mid$ cut

The requirement that $\mid z_1 - z_2 \mid < 2$ cm was varied by $\pm$ 1 cm, and the spectra re-evaluated for data and simulation, including the cosmic background spectrum. Within statistical fluctuations, no systematic effects were observed.

Isolated track requirement

The requirement that there be no other tracks in the hemisphere in which the muon is identified is relaxed, and new spectra evaluated, including a new tau internal background spectrum. The shift observed was statistically compatible with that expected.

Minimum momentum requirement

The minimum momentum required for a track to be identified as a muon is varied to $0.055E_{beam}$ and $0.088E_{beam}$ to investigate any biases due to muon selection efficiency in the low momentum region. The systematic uncertainty is estimated to be 0.029.

Acollinearity cut at 15°

The cut on acollinearity at 15° was varied by ± 2°, and no systematic effects observed within the expected statistical fluctuations.

Other linescan selection cuts

The main remaining selection cuts which could have a biasing effect on the muon momentum spectrum are the acollinearity cut at 0.5°, and the total transverse momentum cut at 0.4 GeV/c. These are applied to obtain the initial $e^+e^- \rightarrow \tau^+\tau^-$ sample from which the muons are selected, and are described in Sections 4.3.1 and 4.4.2. The cuts are removed altogether, and the backgrounds re-evaluated. The shifts observed were statistically compatible with those expected.

Uncertainty on $\varepsilon_-/\varepsilon_+$

The uncertainty on the ratio $\varepsilon_-/\varepsilon_+$ (Equation 7.8) translates into an uncertainty on the corrected value of A_{pol} of 0.005.

Helicity correlations

In instances where the decays of both the taus in an event have been used in measuring the tau polarisation (i.e. in double-tagged muon decays), there is a reduction in sensitivity to the tau polarisation due to the 100 % correlation of the τ^- and τ^+ helicities. This results in an underestimation of the statistical uncertainty of the measurement. Since the muon decay mode has low sensitivity anyway (see Table 2.2), the reduction is not significant [75], and, taking into account the $\tau^- \rightarrow \mu^-\bar{\nu}_\mu\nu_\tau$ selection efficiency, has been estimated and found to be negligible.

7.1.4 Final A_{pol} result

The value of A'_{pol} measured is corrected according to Equation 7.9 to obtain the average tau polarisation A_{pol} :

$$\boxed{A_{pol} = -0.114 \pm 0.129\ (\text{stat}) \pm 0.091\ (\text{syst})} \qquad (7.11)$$

where the statistical uncertainty refers to that on the data only. The sources of systematic uncertainty are listed in Table 7.1.

Source	$\Delta(A_{pol})$
Momentum distribution differences	0.053
Monte Carlo statistics	0.046
E_γ cut	0.030
Minimum momentum requirement	0.029
E_{HCAL} cut	0.026
Pion punchthrough corrections	0.016
Background uncertainties	0.017
Dimuon rejection cuts	0.013
TPC ϕ crack inefficiencies	0.009
Uncertainty on $\varepsilon_-/\varepsilon_+$	0.005
TOTAL	0.091

Table 7.1: *Systematic uncertainties on* A_{pol}.

7.2 Measurement of tau couplings and $\sin^2\theta^l_{W_{eff}}(M_Z^2)$

The value of A_{pol} that has been measured is related to the quantity

$$\mathcal{A}_\tau = -2\frac{c_V^\tau c_A^\tau}{c_V^{\tau 2} + c_A^{\tau 2}} \approx -2\frac{c_V^\tau}{c_A^\tau} \tag{7.12}$$

by the expression

$$A_{pol} = \mathcal{A}_\tau + 0.003 \tag{7.13}$$

where the 0.003 accounts for initial state radiative effects and photon exchange as discussed in Section 1.5.5. The result for A_{pol} that has been obtained in this analysis gives the ratio of the vector and axial-vector coupling constants of the tau to the Z^o as

$$\frac{c_V^\tau}{c_A^\tau} = 0.058 \pm 0.079 \tag{7.14}$$

Using Equation 1.45, the value for the effective mixing angle at the Z^o mass scale is obtained to be:

$$\sin^2\theta^l_{W_{eff}}(M_Z^2) = 0.2354 \pm 0.0198 \tag{7.15}$$

Conclusions

The branching ratio for the decay mode $\tau^- \rightarrow \mu^- \bar{\nu}_\mu \nu_\tau$ (and its charge conjugate) has been measured with a sample of 1613 muons collected during 1991 with the DELPHI detector. The value obtained is

$$\boxed{\mathrm{Br}(\tau^- \rightarrow \mu^- \bar{\nu}_\mu \nu_\tau) = 17.58 \pm 0.41\ (\mathrm{stat}) \pm 0.27\ (\mathrm{syst})\ \%}$$

This is in good agreement with the world average measurement as given by the Particle Data Group (1992) [9] which is

$$Br(\tau^- \rightarrow \mu^- \bar{\nu}_\mu \nu_\tau)_{WA} = 17.58 \pm 0.27\ \%$$

This measurement has been used to find the ratios

$$\left(\frac{g_\mu}{g_e}\right)^2 = 1.018 \pm 0.028, \quad \left(\frac{g_\tau}{g_e}\right)^2 = 0.998 \pm 0.030$$

where g_l is the effective coupling constant at the $l-W-\bar{\nu}_l$ vertex. These ratios are consistent with 1, and thus support the hypothesis of lepton universality.

The average polarisation of the tau has been measured with the muon momentum spectrum to be

$$\boxed{A_{pol} = -0.114 \pm 0.129\ (\mathrm{stat}) \pm 0.091\ (\mathrm{syst})}$$

This result is in agreement with measurements of the tau polarisation made at energies near the Z^o peak using all the major decay modes by other LEP experiments and by DELPHI using the 1990 data set [78]:

$$A_{pol_{LEP}} = -0.142 \pm 0.017$$

The polarisation value obtained in this analysis gives the ratio of the vector and axial-vector coupling constants of the tau to the Z^o as

$$\frac{c_V^\tau}{c_A^\tau} = 0.058 \pm 0.079$$

In the Standard Model, this ratio depends on the value of the effective weak mixing angle at the Z^o mass scale which is derived to be

$$sin^2\theta^l_{W_{eff}}(M_Z^2) = 0.2354 \pm 0.0198$$

and is in agreement with recent measurements at LEP involving several different processes from which this parameter can be deduced [16]:

$$sin^2\theta^l_{W_{eff}}(M_Z^2)_{LEP} = 0.2324 \pm 0.0011$$

Prospects for the future

The above measurements have been based on a total Z^o sample of around 250 K events. From 1991 to 1994, approximately 3 million Z^o events will have been collected at DELPHI. The corresponding statistical precision on $Br(\tau^- \rightarrow \mu^- \bar{\nu}_\mu \nu_\tau)$ and A_{pol} will be 0.12 and 0.04 respectively.

The main features of this analysis are the high selection efficiency for muons within the fiducial region, and low levels of background, both of which are checked using the data itself. Since the bulk of the systematic uncertainties arise from correction factors or amounts of background, their magnitude is therefore limited by the data. Thus, the systematic uncertainties are expected to decrease in proportion to the statistical uncertainty. The largest single contribution to the systematic uncertainty on the polarisation measurement comes from the momentum scale uncertainty at high momentum. This should be better understood in the future. Thus, the overall precision which can be expected to be achieved at LEP100 will be statistics dominated.

The consequent precision on $(g_\mu/g_e)^2$ and $(g_\tau/g_e)^2$ will be around 1 %, and 0.006 on $\sin^2\theta^l_{W_{eff}}(M_Z^2)$. The existence of parity violation in the production of taus may also be established with the muon decay mode at DELPHI. Other feasible measurements [15] include a determination of the parameter $\mathcal{A}_e$ through a measurement of the polarisation forward-backward asymmetry, or together with $\mathcal{A}_\tau$ through a measurement of A_{pol} as a function of θ, which would provide a test of universality in the neutral current interaction. Also, the $V-A$ nature of the tau decay which has been assumed in this analysis could be investigated using the decay correlations between the muon decay mode and other tau channels. With large improvements in statistics close by, the muon decay mode of the tau certainly merits continued study.

References

[1] S.L. Glashow, *Nucl. Phys* **B22** (1961) p579.
S. Weinberg, *Phys. Rev. Lett* **19** (1967) p1264.
A. Salam, *Proc. 8th Nobel Symposium*, Aspenäsgarden 1968, ed. N. Svartholm (Almqvist and Wiksell, 1968) p367.

[2] F.J. Hasert et al, *Phys Lett* **46B** (1973) p138, *Nucl. Phys* **B73** (1974) p1.

[3] LEP Design Report, CERN-LEP/84-01 (1984).

[4] P. Aarnio et al, DELPHI Collab., *Nucl. Inst. Meth.* **A303** (1991) p233.

[5] F. Matorras, DELPHI 92-124 PHYS 124 (1992).

[6] N. Cabbibo, *Phys. Rev. Lett* **10** (1963) p531.
M. Kobayashi and K. Maskawa, *Prog. Theor. Phys* **49** (1972) p282.

[7] M. Gell-Mann, *Phys. Rev.* **92** (1953) p833.
K. Nishijima, *Prog. Theor. Phys.* **13** (1955) p285.

[8] P.W. Higgs, *Phys. Lett.* **12** (1964) p132, *Phys. Rev.* **13** (1964) p508, *Phys. Rev. Lett* **145** (1966) p1156.
F. Englert and R. Brout, *Phys. Rev. Lett.* **13** p321.
G.S. Guralnik, C.R. Hagen and T.W.B. Kibble, *Phys. Rev. Lett.* **13** (1964) p585.

[9] K. Hikasa et al, Particle Data Group, *Phys. Rev.* **D45** (1992).

[10] See for example, F. Halzen and A. Martin, *Quarks and Leptons* (John Wiley and Sons, 1984).

[11] D. Bardin et al, DELPHI Collab., DELPHI 92-114 PHYS 220 (1992).

[12] W. Bonivento, DELPHI 93-91 PHYS 318 (1993).